Aus dem Lehrstuhl für Computerunterstützte Klinische Medizin

der Medizinischen Fakultät Mannheim

(Komm. Direktor: Prof. Dr. Ing. Frank G. Zöllner)

Advancing Sodium Multi-Quantum Coherences MRI on Clinical Scanners

Inauguraldissertation
zur Erlangung des Doctor scientiarum humanarum (Dr. sc. hum.)
der
Medizinischen Fakultät Mannheim
der Ruprecht-Karls-Universität zu Heidelberg

vorgelegt von

Christian Licht, M.Sc.

aus

Bergisch Gladbach

2023

Dekan: Prof. Dr. med. Sergij Goerdt
Referent: Prof. Dr. rer. nat. Lothar R. Schad

Advancing Sodium Multi-Quantum Coherences MRI on Clinical Scanners

In recent years, sodium (^{23}Na) Magnetic Resonance Imaging (MRI) has gained increased attention, particularly with the development of ultra-high field >= 7 T MRI. It provides non-invasive physiological information related to the cell's vitality, making it an exciting tool for medical research. ^{23}Na MRI provides a non-invasive quantitative estimation of the tissue sodium concentration. However, ^{23}Na MRI could provide rich additional contrast information, which can be exploited by leveraging ^{23}Na Multi-Quantum Coherences (MQC) MRI. Unfortunately, ^{23}Na MQC MRI is inherently slow and challenging to use in clinical protocols. As a result, the full potential of ^{23}Na MQC MRI has yet to be explored. This work focused on developing acceleration techniques to obtain ^{23}Na MQC MRI in clinically acceptable scan time. The proposed frameworks were extensively studied on numerical simulations, phantom, and in vivo human brain data acquired at 3 and 7 T.

In the first part of this thesis, a custom-built multi-dimensional (5D) reconstruction framework based on Compressed Sensing (CS) theory is presented. This framework constitutes an advanced sampling strategy to accelerate the acquisition of ^{23}Na MQC MRI up to 3-fold, coupled with an iterative reconstruction algorithm that optimally leverages ^{23}Na MQC MRI's signal structure to reconstruct highly undersampled data reliably. A comprehensive study showed the advantages of the 5D CS over the conventional 3D CS reconstruction. Reliable acceleration factors up to 3-fold were possible, reducing acquisition times or increasing the spatial resolution to unprecedented 6x6x10mm^3.

Secondly, the gained experience of MR signal sampling and reconstruction of undersampled ^{23}Na MQC MRI from the first part was leveraged to improve the sequence and the reconstruction framework. The sequence was adapted to simultaneously acquire ^{23}Na and ^{23}Na MQC MRI, with ^{23}Na MQC MRI being highly undersampled. The reconstruction was performed by two advanced low-rank reconstruction frameworks that optimally exploit the coherent information in the acquired data. 6x6x6mm^3 in vivo ^{23}Na MRI leveraging the Double Half-Echo technique was demonstrated for the first time. The low-rank reconstruction performance for ^{23}Na MQC MRI was compared to the 5D CS model and outperformed 5D CS regarding SSIM, RMSE, and SNR. Eventually, the novel accelerated acquisition was leveraged to obtain whole-brain ^{23}Na MQC MRI images with an unprecedented spatial resolution of 8mm isotropic in 2x23 minutes, uniquely showcasing the sodium tissue characteristics of white and grey matter. The simultaneously acquired sodium images at 6mm isotropic lay ground for a complete quantitative evaluation of brain sodium MRI for future studies.

This thesis aimed to overcome ^{23}Na MQC MRI's obstacles, mainly targeting the slow acquisition speed leading to lengthy acquisitions and limited spatial resolution. Two advanced reconstruction frameworks have been proposed that efficiently leverage the highly multi-dimensional structure of ^{23}Na MQC MRI and, therefore, outperform conventional reconstruction techniques. Additionally, an efficient sequence was proposed that allows for simultaneous acquisition of ^{23}Na and prospectively undersampled ^{23}Na MQC MRI within clinically acceptable time that allows for a direct

comparison of ^{23}Na and ^{23}Na MQC MRI fostering the possibility to be used for clinical studies. Extensive experiments demonstrated applicability on 3 and 7 T clinical MRI, which makes the frameworks highly versatile and robust. In conclusion, the presented sequence and reconstruction algorithms represent a promising framework for future studies exploiting ^{23}Na and ^{23}Na MQC MRI with a clinical research focus.

Weiterentwicklung der Natrium Multiquantenkohärenz Magnetresonanztomographie auf klinischen Scannern

In den letzten Jahren erhielt die Natrium (^{23}Na) Magnetresonanztomographie (MRT) immer mehr Aufmerksamkeit, da sie nicht-invasiv wichtige Gewebeinformationen bereitstellt, die direkt mit der Zellvitalität verknüpft sind. Ebenso hat die Entwicklung von Ultrahochfeld Scannern (>= 7 Tesla) dazu beigetragen, dass die Natrium MRT immer häufiger verwendet wird. Das Besondere an der ^{23}Na MRT ist, dass sie die quantitative Bestimmung der Gewebe-Natriumkonzentration in vivo ermöglicht. Neben der Gewebe-Natriumkonzentration, liefert die ^{23}Na MRT weitere Informationen, die man mit Hilfe der ^{23}Na Multiquantenkohärenz (MQC) Bildgebungstechnik auflösen kann. Leider ist die Akquisitionszeit von ^{23}Na MQC MRT für die klinische Anwendung zu lang und macht es daher schwierig, das Potenzial der ^{23}Na MQC MRT vollständig zu untersuchen. Diese Arbeit beschäftigte sich mit der Entwicklung von robusten Methoden zur Beschleunigung der Akquisition, welche die klinische Anwendung von ^{23}Na MQC MRT ermöglichen. Hierzu wurden verschiedene Methoden entwickelt und in nummerischen Simulationen, Phantom und in vivo Kopf-Messungen auf 3 und 7 Tesla miteinander verglichen.

Der erste Teil dieser Arbeit beschäftigte sich mit der Entwicklung eines mehrdimensionalen (5D) Rekonstruktionsmodels basierend auf der Compressed Sensing (CS) Theorie. Hierzu wurde eine fortschrittliche Unter-Abtastmethode verwendet, die die Beschleunigung der ^{23}Na MQC MRT ermöglichte. Die unterabgetasteten Daten wurden mit Hilfe des Rekonstruktionsalgorithmus, unter Berücksichtigung der Mehrdimensionalität des ^{23}Na MQC Signals, optimal rekonstruiert. Ausführliche Experimente demonstrierten den Vorteil der neuen gegenüber der herkömmlichen Rekonstruktionsmethode und ermöglichte somit eine robuste Beschleunigung der Akquisition um den Faktor drei. Aufgrund der beschleunigten Aufnahme konnte erstmals eine höhere räumliche Auflösung von 6x6x10mm^3 in vivo erzielt werden.

Für den zweiten Teil der Arbeit wurden die Kenntnisse bezüglich der Unterabtastung aus dem ersten Teil verwendet, um die Rekonstruktion und die MRT-Sequenz zu verbessern. Die Sequenz wurde erweitert um gleichzeitig ^{23}Na MRT und unterabgetastete ^{23}Na MQC MRT zu ermöglichen. Zum ersten Mal in der ^{23}Na MRT wurden nieder-Rang Rekonstruktionsalgorithmen verwendet, um simultane ^{23}Na MRT und ^{23}Na MQC MRT zu rekonstruieren. Der Vorteil dieser Rekonstruktionsalgorithmen basiert darauf, dass kohärente Informationen stark komprimiert werden können. Zum ersten Mal wurde die Doppel-Echo Technik angewandt, um 6x6x6mm^3 ^{23}Na in vivo MR Bilder aufzunehmen. Die Rekonstruktion der ^{23}Na MQC Daten wurde mit dem 5D CS Model aus dem ersten Teil der Arbeit quantitativ verglichen. Letztlich wurde ^{23}Na MQC MRT prospektiv unterabgetastet, um eine höhere räumliche Auflösung von 8x8x8mm^3 zu erzielen. Die neue Sequenz bietet die Möglichkeit simultan ^{23}Na und ^{23}Na MQC MRT mit höherer räumlicher Auflösung in 2x23 Minuten aufzunehmen, welches eine optimale Grundlage für weitere Studien bietet, in denen das vollständige ^{23}Na Signal untersucht werden kann.

Diese Arbeit zeigte Lösungen auf, wie die lange Akquisitionszeit der ^{23}Na MQC MRT effektiv reduziert und die limitierte räumliche Auflösung erhöht werden kann. Hierfür wurden zwei Rekonstruktionsalgorithmen vorgestellt, die unterschiedlichen

mathematischen Konzepten unterliegen. Beide Algorithmen wurden dahingehend optimiert, dass diese die mehrdimensionale Struktur des ^{23}Na MQC MRT Signals optimal für die Rekonstruktion nutzen und demonstrierten verbesserte Rekonstruktionsresultate als herkömmliche Algorithmen. Beide Methoden wurden ausgiebig in silico, in vitro und in vivo getestet, um fundierte Aussagen über die Qualität der Rekonstruktion treffen zu können. Des Weiteren wurde eine effiziente Sequenz entwickelt, die die simultane Akquisition von ^{23}Na und ^{23}Na MQC MRT ermöglicht. Die neue Sequenz überzeugte durch die vereinfachte Rekonstruktion und die Robustheit der Akquisition aufgrund der kartesischen Aufnahmestrategie und stellt somit eine wichtige Grundlage für weitere ^{23}Na MRT Studien da.

Contents

List of Figures

List of Tables

List of Acronyms

1D	one-dimensional
2D	two-dimensional
3D	three-dimensional
4D	four-dimensional
5D	five-dimensional
ADC	Analog-to-Digital Converter
CRISTINA	Cartesian simultaneous Single and Triple Quantum ^{23}Na
CS	Compressed Sensing
DHE	Double Half-Echo
DQ	Double Quantum
DQC	Double Quantum Coherence
EFGs	Electric Field Gradients
FID	Free Induction Decay
FoV	Field of View
FT	Fourier transform
GM	Gray matter
GRE	Gradient Recalled Echo
iFT	inverse Fourier transform
MQC	Multi-Quantum Coherence
MR	Magnetic Resonance
MRI	Magnetic Resonance Imaging
NMR	Nuclear Magnetic Resonance
PSF	Point Spread Function
RF	Radiofrequency
RMSE	Root Mean Squared Error

ROI	Region of Interest
SAKE	Simultaneous Auto-calibrating and k-space Estimation
SAR	Specific Absorption Rate
SBM	Split Bregman Method
SNR	Signal-to-Noise Ratio
sodium	^{23}Na
SQ	Single Quantum
SQC	Single Quantum Coherence
SSIM	Structural Similarity Index
SVD	Singular Value Decomposition
SVT	Singular Value Thresholding
TE	Echo Time
TQ	Triple Quantum
TQC	Triple Quantum Coherence
TSC	Tissue Sodium Concentration
TV	Total Variation
UTE	Ultrashort Echo Time
VD	Variable Density
WM	White matter
ZQC	Zero Quantum Coherence

1. Introduction and Outline

1.1 Motivation

Sodium ^{23}Na Magnetic Resonance Imaging (MRI) can provide valuable quantitative information regarding cell vitality. In addition, the physical properties of the sodium nucleus lead to multi-quantum coherence (MQC), which could uniquely reveal insights into cell viability. However, sampling these MQCs is challenging because it is inherently slow and thus, limited in its spatial resolution. Following, robust acceleration is warranted. Emphasizing ^{23}Na MQC MRI exhibits highly multi-dimensional and structured information; this prior knowledge can be leveraged to design a dedicated reconstruction allowing undersampled acquisition. Hence, the leading research hypothesis for this work was defined as:

Can knowledge-driven image reconstruction improve ^{23}Na MQC MRI towards faster and better resolved whole-brain sodium quantitative imaging?

1.2 Outline

This thesis provides a brief introduction to NMR, MRI, and sodium MRI, with the basic concepts of sparse and low-rank reconstructions given. Focused on image reconstruction, the thesis resulted in two main research articles, with the first one focusing on sparse image reconstruction and the second paper addressing low-rank reconstruction frameworks to advance ^{23}Na MQC MRI.

In the first project of this thesis, a sparse image reconstruction framework was developed that optimally leverages the multi-dimensional signal structure of ^{23}Na MQC MRI. The framework is based on Compressed Sensing (CS) theory and was compared to a standard three-dimensional CS framework. An extensive investigation of numerical simulations, phantoms, and retro- and prospective in vivo brain data acquired at 3 and 7 T was performed. This model enabled prospective undersampling to obtain unprecedented ^{23}Na MQC MRI spatial resolution while not exceeding imaging time.

The second project involved advancing ^{23}Na MQC MRI by leveraging two dedicated low-rank matrix completion frameworks. Obtaining ^{23}Na MQC MRI requires accurate pulse sequences, and the used sequence in this study was improved to also acquire conventional ^{23}Na MRI. ^{23}Na MRI was developed with the Double Half-Echo technique, which samples two individual k-space halves. Both k-space halves are reconstructed by leveraging an iterative framework with a low-rank coupling constraint. Additionally, the multi-dimensional structure of ^{23}Na MQC MRI was leveraged in another low-rank matrix completion framework that exploits coherent information to reconstruct highly undersampled ^{23}Na MQC MRI. Comprehensive experiments on numerical simulations, phantom, and retro- as well as prospective in vivo data acquired at 7 T validated the new sequence and the low-rank reconstruction frameworks.

1.3 Related Publications

Several chapters of this thesis have already been published in the international journal *Magnetic Resonance in Medicine*.

Licht C, Reichert S, Guye M, Schad LR, Rapacchi S. Multidimensional compressed sensing to advance 23Na multi-quantum coherences MRI. Magn Reson Med. 2024; 91: 926-941. doi: 10.1002/mrm.29902

Licht C, Reichert S, Bydder M, et al. Low-rank reconstruction for simultaneous double half-echo 23Na and undersampled 23Na multi-quantum coherences MRI. Magn Reson Med. 2024; 1-16. doi: 10.1002/mrm.30132

2. Theoretical Background

2.1 Nuclear Magnetic Resonance

Nuclear Magnetic Resonance (*NMR*) describes an event in which a nucleus, placed in an external static magnetic field, B_0, interacts with a superimposed oscillating magnetic field, B_1^+, and emits an electromagnetic wave in return. This signal exhibits a frequency characteristic of the relationship between the nucleus and the magnetic field. However, not every nucleus undergoes NMR. Only nuclei that have an intrinsic nuclear magnetic moment, $\vec{\mu}$, and angular momentum, $\vec{J}$, which in return are nuclei with a spin quantum number, $I > 0$. Following, nuclei with $I = 0$ do not undergo NMR. A nucleus that is NMR sensitive is the hydrogen nucleus, ^{1}H, which exhibits a spin quantum number, $I = 1/2$, and, therefore, possesses a magnetic moment. Owed to the magnetic moment, a nucleus with spin 1/2 is regarded as a dipole magnet,[1, 2] which can be manipulated by an externally applied magnetic field.

Once the 1/2 nuclei are placed inside a magnetic field, the spins precess around its main axis statistically aligned parallel or anti-parallel to the field lines.[2] Due to parallel and anti-parallel alignment of the spins, manipulation of the magnetization requires a defined amount of energy, ΔE.

$$\Delta E = \hbar \gamma B \tag{2.1}$$

The manipulation of nuclear spins requires matching energy differences, ΔE, specific to certain nuclei (Figure 2.1). Owed to the parallel and anti-parallel orientations,

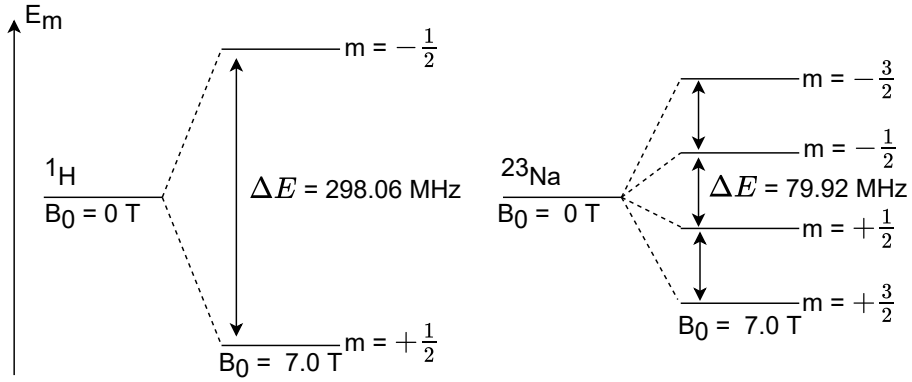

Figure 2.1: Energy levels of two spin systems, 1/2 and 3/2, when placed inside a homogeneous magnetic field, $B_0 = 7$ T. The energy levels split up equidistantly, with parallel orientation being energetically favorable rather than anti-parallel.

only in spin 1/2 systems, two proton spin populations exist with the ratio defined as[3]

$$\frac{n_-}{n_+} = e^{-\Delta E/kT} \tag{2.2}$$

with k being the Boltzmann's constant and T the absolute temperature.

Since $\frac{n_-}{n_+} <^{\epsilon} 1$ for ^{1}H (at room temperature), a slightly larger portion of parallel than anti-parallel spins exist. The difference between the resulting macroscopic spin-up and spin-down vectors yields the final macroscopic magnetization vector. The equilibrium Magnetization, M_0, is then defined as

$$M_0 = \frac{N\gamma^2\hbar^2 I(I+1)B_0}{3kT} \tag{2.3}$$

The resulting magnetization depends on the number of nuclear spins, N, the gyromagnetic ratio, γ, and the static magnetic field, B_0.[3]

Suppose a spin ensemble is placed inside a static magnetic field. In that case, each magnetic moment from every spin in the magnetic field gets polarized along the direction of the applied magnetic field. Hence, the sum of each magnetic moment, μ_i, yields a net magnetization vector, $\vec{M}$.[1]

$$\vec{M} = \sum_{i=1}^{n} \vec{\mu_i} \tag{2.4}$$

If no main magnetic field is applied, all the magnetic moments will cancel each other $\vec{M} = 0$.[1] However, suppose the spins are exposed to a static and homogeneous magnetic field. In that case, the magnetic moment statistically aligns with the direction of the magnetic field and precesses in that specific direction.

The Larmor frequency, $\vec{\omega}_0$, describes the precession frequency of the spins about B_0 [4].

$$\text{Larmor frequency: } \vec{\omega}_0 = \gamma B \tag{2.5a}$$

$$\text{Gyromagnetic ratio: } \gamma = \frac{\vec{\mu}}{\vec{J}} \tag{2.5b}$$

The Larmor frequency is the frequency to which the spins are resonant. This linear relationship is a fundamental concept in NMR as it relates the precession frequency with the magnetic field strength the nuclei are exposed to. The gyromagnetic ratio, γ, is defined as the ratio of the magnetic moment, $\vec{\mu}$, to the angular momentum, $\vec{J}$ and is specific to every nuclei, for example: $\gamma_{^1H} = 42.58$ MHz/T or $\gamma_{^{23}Na} = 11.26$ MHz/T for the ^{23}Na (*sodium*) nucleus. If the magnetic moment and the spin are in the same direction, $\gamma > 0$. However, if $\gamma < 0$, the magnetic moment and the spin are in opposite directions.

Since the magnetization, $\vec{M}$, can be manipulated and is thus a function of time, $M(t)$ at time t, the magnetization behavior is expressed as a differential equation.

$$\frac{d\vec{M}}{dt} = \vec{M} \times \gamma B(\vec{r}) \tag{2.6}$$

Equation 2.6 is the vectorized form of the Bloch equations,[5] without accounting for relaxation. It is important to note that $B(\vec{r})$ includes all magnetic fields applied.[3] The Bloch equation thus describes nuclear magnetization with respect to time[1] and

[1]The magnetization vector, $\vec{M}$, is not necessarily static as it can change directions. The Bloch equations are sometimes referred to as the equations of motion of nuclear magnetization and were introduced by Felix Bloch in 1946.[5]

are the fundamental concepts to understand the formation of an NMR signal. Nevertheless, it is important to note that this equation only holds for macroscopic nuclear magnetization when all individual magnetic moments are summed up, contributing to a final macroscopic magnetization vector, $\vec{M}$.

The human body consists of various molecules which are constantly vibrating. Therefore, the center of mass of the molecules averaged over its multiple positions, can be approximated by a single position. Indeed, small molecules' precession is faster than larger molecules such as proteins.[6] Following from Equation 2.5a, this precession frequency is characteristic of specific molecules; hence, NMR can probe molecular motion and the environment.

Radiofrequency pulse

Derived from Equation 2.6, the macroscopic magnetization can be manipulated by superimposing an additional time-varying magnetic field Radiofrequency (*RF*), B_1^+, which interacts with the nuclear spin, leading the spins to change their precession direction.[2]

$$B_{\text{eff}} = B_0 + B_1^+ \tag{2.7}$$

The new precession direction is statistically given by the RF's flip angle, θ.

$$\theta = \gamma \int_{t=0}^{\tau} B_1^+(t)dt \tag{2.8}$$

With τ being the time the RF pulse is applied. The new precession frequency that the tipped spins possess is then given by

$$\omega_1 = \gamma B_1^+ \tag{2.9}$$

The RF pulse is most effective at matching (Larmor) frequency and is sent perpendicular to the static magnetic field. However, the energy of the RF pulse is absorbed by the body. This, in return, imposes restrictions on the in vivo application of RF pulses, foremost to avoid tissue heating. The absorbed energy is termed Specific Absorption Rate (*SAR*) and is defined as

$$SAR \propto \int_0^t |B_1^+(t)^2|dt \tag{2.10}$$

In sodium NMR experiments, short, hard RF pulses are favored to minimize relaxation processes during the excitation. Nevertheless, following from Equation 2.8 and Equation 2.10, SAR imposes restrictions on in vivo NMR experiments, which usually lead to elongation of the RF pulse not to exceed the SAR limit.

[2] For simplicity, a laboratory frame of reference is used. This frame of reference rotates clockwise at the Larmor frequency, which enables the neglect of the precession of the net magnetization vector, $\vec{M}$, around the static magnetic field.[6] Hence, manipulating the magnetization vector can be described as the tipping of a stationary vector.

Thanks to the applied RF pulse, the macroscopic magnetization vector is tipped towards the transverse plane (xy-plane). According to Faraday's law, this induces an electromotive force, ε, into the receiver coils.

$$\varepsilon = -\frac{d\Phi_B}{dt} \tag{2.11}$$

Equation 2.11 states that the rate of change of the magnetic flux, Φ_B, induces an electromotive force, ε, in the receiver coil. After the RF pulse is applied, the net magnetization vector is tipped, which changes the magnetic flux, $d\Phi_B$, and therefore, an electromotive force is induced. It follows that the induced electromotive force over a given volume, V, is expressed as[4]

$$\varepsilon = -\frac{d}{dt}\int_V dr\vec{M}_{xy}(\vec{r},t)\vec{B}_1^-(\vec{r},t) \tag{2.12}$$

and is proportional to

$$\varepsilon \propto S_{\mathrm{NMR}} \propto \gamma^3 I(I+1)c_{\mathrm{phys}}c_{\mathrm{bio}} \tag{2.13}$$

with S_{NMR} being the detected signal, c_{phys} being the relative abundance ($c_{\mathrm{phys}} = 1$ for ^{23}Na) and c_{bio} representing the biological abundance. It follows from Equation 2.13 that the induced NMR signal highly depends on the gyromagnetic ratio of the investigated nucleus and the natural abundance. ^{1}H NMR is the most clinically used nucleus to obtain the NMR signal. Table 2.1 lists commonly used nuclei in NMR. The second best choice regarding signal intensity is ^{23}Na. Although other nuclei than ^{1}H are challenging to investigate, these nuclei have the potential to provide additional information, which is not accessible via ^{1}H NMR alone.

Table 2.1: NMR properties of several nuclei that are typically used, see [7].

Isotope	Spin I	$\frac{\gamma}{2\pi}$ [MHz/T]	Abundance c [%]	Rel. sensitivity
^{1}H	1/2	42.58	99.99	1.0
^{2}H	1	6.54	0.01	4.8×10^{-3}
^{19}F	1/2	40.08	100	8.3×10^{-1}
^{23}Na	3/2	11.27	100	9.3×10^{-2}
^{39}K	3/2	1.99	93.26	4.8×10^{-4}
^{17}O	5/2	5.77	0.04	2.9×10^{-2}

Relaxation

Maintaining the spins' changed direction after the RF pulse was applied requires a constant supply of energy in the form of an electromagnetic wave. If the RF pulse is turned off, the spins return to their initial orientation.[2] Once all excessive energy is dissipated, the spins are aligned with the main magnetic field's direction, and the magnetic flux is constant. Conclusively, no voltage is induced anymore. The return of the net magnetization vector to its initial direction (z-axis), inducing an electromotive force, is called Free Induction Decay (*FID*).[4] It refers to the signal probed in NMR when only a single RF pulse is applied.

The excessive energy that is dissipated is referred to as 'relaxation', which is governed by two significant effects:

1. Spin-lattice interaction (longitudinal relaxation, T_1)
2. Spin-spin interaction (transversal relaxation, T_2)

T_1 - longitudinal relaxation
Spin-lattice interaction characterizes the return of the magnetization vector to its equilibrium state along the direction of the static magnetic field. Thermal equilibrium is reached when $M_z = M_0$. T_1 is greatly influenced by the magnetic dipoles in the surrounding environment. The magnetic fields generated by the additional dipoles induce transitions between the spin populations n_+ and n_-. The energy required for these transitions depends on the magnetic field strength, and following, T_1 increases with increasing field strength.[3]

T_2 - transverse relaxation
The spin-spin interaction describes the decay rate of the transverse magnetization, M_{xy}. The field components along z, generated by the same magnetic dipoles as described in the previous paragraph about T_1, also influence the transverse relaxation. These additional fields lead to a broadening of the Larmor frequency spectrum, forcing the spins to precess at slightly different frequencies. As a result, the spins lose coherence towards each other[3] in the transverse plane, with $T_2 < T_1$. These additional fields are small and, therefore, only contribute to T_2 and not to T_1 relaxation. Following, T_2 is independent of the magnetic field strength.[3]

With the relaxation time constants introduced, Equation 2.6 is extended to describe the change of magnetization along the x-, y- and z-axis while taking T_1 and T_2 relaxation into account.

$$\frac{dM_x}{dt} = \gamma(M(t) \times B)_x - \frac{M_x}{T_2} \tag{2.14}$$

$$\frac{M_y}{dt} = \gamma(M(t) \times B)_y - \frac{M_y}{T_2} \tag{2.15}$$

$$\frac{dM_z}{dt} = \gamma(M(t) \times B)_z - \frac{M_0 - M_z}{T_1} \tag{2.16}$$

Since the transverse magnetization is described in the complex plane as $M_{xy}(t) = M_x(t) + iM_y(t)$,[4] with $i = \sqrt{-1}$, the solutions to Equation 2.16 in the rotating frame of reference are given by

$$M_{xy}(t) = M_{xy}(0)e^{i\omega_0 t}e^{-\frac{t}{T_2}} \tag{2.17}$$

$$M_z(t) = M_0 - (M_0 - M_z(0))e^{-\frac{t}{T_1}} \tag{2.18}$$

After applying a perfect 90° RF pulse, the net magnetization is solely given by the transverse magnetization, M_{xy}. In this state, the spins exchange energy between themselves, e.g., dipole-dipole interaction. This leads to the spins losing their phase coherence and, following, reduces M_{xy}, as previously discussed. The dephasing process is further influenced by field inhomogeneities, resulting in deviations from the

[3] The process of coherence loss is also called 'dephasing'

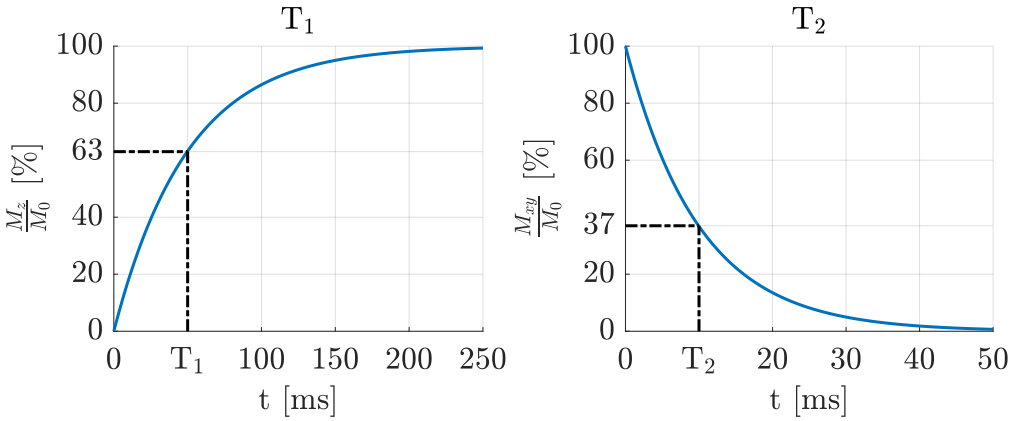

Figure 2.2: Longitudinal (T_1) and transverse (T_2) magnetization after a 90° RF pulse was applied with $T_2 < T_1$. Full relaxation is observed when $t = 5T_1$.

Larmor frequency, and therefore, relaxation occurs faster. Another constant describes this enhanced relaxation process, T_2^*.

$$\frac{1}{T_2^*} = \frac{1}{T_2} + \gamma \Delta B \tag{2.19}$$

with ΔB being the magnetic field inhomogeneities. Whereas T_2 is unaffected by the magnetic field strength, T_2^* is highly affected, and thus, T_2^* reduces with increasing field strength. T_2^* is always measured after excitation unless a refocusing RF pulse of 180° is applied to counter the field inhomogeneities related to dephasing processes. Leveraging a 90° followed by a 180° RF pulse is termed a 'Spin-Echo-Experiment'. However, without further energy deposition, the net magnetization returns to equilibrium by dissipating the RF pulse-induced energy to the surroundings (lattice). T_1 is optimally probed by leveraging an 'Inversion-Recovery-Experiment', a spin echo experiment with a 180° RF pulse applied before the 90° RF pulse.

Fourier transform

In general, periodic functions, $f(x)$, are described as a combination of $sin(x)$ and $cos(x)$. Replacing $t \leftarrow x$, the time-dependent periodic signal is described by the Fourier series as

$$S(t) = \sum_{j=0}^{+\infty} (A_j sin(\omega_j t) + B_j cos(\omega_j t)) \tag{2.20}$$

with A_j and B_j being the amplitudes and ω_j the oscillation frequency of frequency j. If the amplitudes are known, any given signal, $S(t)$, can be fully expressed in terms of *sin* and *cos* functions. In this case, $j \in \mathbb{N}$, with $j > 0$. To also account for negative frequencies, Equation 2.20 is extended to

$$S(t) = \sum_{j=-\infty}^{+\infty} \left(\frac{A_j}{2} sin(\omega_j t) \pm \frac{B_j}{2} cos(\omega_j t) \right) \tag{2.21}$$

leading to an equivalent distribution of frequencies across the positive and negative spectrum, giving rise to a complex signal. From Euler's formula, it follows that

$$e^{-i\omega t} = cos(\omega t) - isin(\omega t) \tag{2.22}$$

with $i = \sqrt{-1}$. Finally, substituting Equation 2.22 into Equation 2.21 expresses any given signal in the frequency domain and, finally, yields the continuous Fourier transform

$$S(\omega) = \int_{-\infty}^{+\infty} S(t)e^{-i2\pi\omega t}dt \tag{2.23}$$

The continuous Fourier transform (FT), F, is a simple forward signal model, which maps the periodic time-dependent signal, $S(t)$, into a signal that solely depends on the frequencies, ω and hence, the transform is given by $S(t) \xrightarrow{F} S(\omega)$. Following, the inverse Fourier transform is defined as

$$S(t) = \int_{-\infty}^{+\infty} S(\omega)e^{i2\pi\omega t}d\omega \tag{2.24}$$

Therefore, the Fourier transform gives rise to the frequencies embedded in the original signal, and the inverse Fourier transform recovers the time-dependent signal that was represented in the frequency domain. The following paragraph demonstrates the FT regarding the NMR spectrum and its application in MRI.

NMR spectrum

In theory, all nuclei of the same isotope share the same resonance frequency. However, the electron cloud surrounding a nucleus shields it from the main magnetic field, with the shielding effect depending on the electron cloud's density. The electron shielding effect leads to a slightly different local field $B_{loc} = B_0 + \Delta B$ experienced by the nucleus. Following, the same nuclei in different molecular environments experience varying degrees of electron shielding and, thus, exhibit slightly different local fields, B_{loc}. In conclusion, an alteration of the local field results in a change of the Larmor frequency by $\Delta\omega = B_0 + \Delta B$, also called a chemical shift.[8]

Given the FID in time, the FT computes dominant frequency components, giving rise to the FID's spectrum[4]. Referring to the first FID, FID_1 in Figure 2.3, only a single damped frequency makes up the FID and, thus, yields a single Lorentzian peak in the frequency spectrum. Superimposing another FID, with $\omega_{\text{FID}_2} > \omega_{\text{FID}_1}$, the Fourier transform reveals two Lorentzian peaks indicating two dominant frequencies the time-dependent input signal is composed of. The Fourier transform is a powerful tool for analyzing time-dependent signals by decomposing the input signal into a combination of trigonometric functions. These functions are scaled by an amplitude, which gives rise to the extent of each single function contributing to the final input signal. The FT enables the determination of these amplitudes, providing valuable information about the input signal[5].

[4] An FID spectrum is a distribution of frequencies that the FID consists of. The FT reveals the underlying frequency components and provides the FID's frequency spectrum.

[5] In other words, the FT enables the expression of any time-dependent signal as a combination of weighted trigonometric functions. Once each amplitude of the dominant functions is known, the complete signal is mathematically described as a combination of these weighted functions.

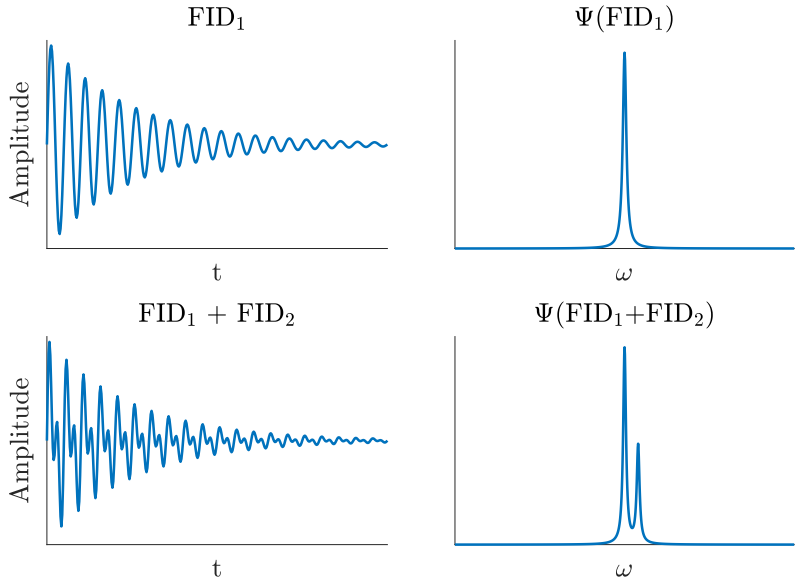

Figure 2.3: Two time-dependent free induction decays, FID_1 and FID_2, with their respective Fourier transform, Ψ, giving rise to the FIDs' spectrums.

Applying a Fourier transform, Ψ, to a time-dependent signal exhibits the frequency components, $\Psi(S(t)) \rightarrow S(\omega)$, and vice-versa; computing the inverse FT, Ψ^{-1}, of the frequency spectrum yields the time-dependent FID signal, $\Psi(S(\omega))^{-1} \rightarrow S(t)$. Figure 2.3 shows a spectrum of a non-local FID. However, additional information is needed in imaging to spatially encode the signal, which will be discussed in the next section.

2.2 Magnetic Resonance Imaging

Magnetic Resonance Imaging (*MRI*) is based on NMR. It is a constantly evolving tool for the non-invasive study of anatomical structures and functions of the human body, with MRI offering the ability to provide information for diagnosis of diseases, anatomical information, and detection of early stages in pathologies.[9] MRI has two major advantages over other imaging modalities. First, MRI does not rely on ionizing radiation and second, MRI provides outstanding soft tissue contrast and is therefore exceptionally well suited for in vivo head imaging. Despite MRI primarily being used for anatomical imaging, it is also capable of functional imaging.[10] Functional imaging gives rise to physiological parameters that provide additional information besides anatomical structures. Foremost, information about tissue viability is of interest.[11]

Generally speaking, MRI uses radiowaves coupled with strong magnetic fields to excite the spins of a patient placed inside the scanner. The patient then re-emits radiowaves that are processed into an image. The image represents a spin-density weighted map of the region of interest, with the amplitude of the voxel being scaled according to the underlying spin density.[1]

MRI involves three magnetic fields:

1. The static magnetic field, B_0
2. The RF pulse to excite the spins, B_1^+
3. The gradients, $G(t)$

With the gradients representing the most important component of MRI.[3] Instead of measuring a single NMR signal across a volume, the gradients can discretize the volume into a 2D or 3D grid. Hence, the gradients enable precise spatial encoding of the NMR signal. These gradients are additional magnetic fields spanning the x, y, and z-directions. Conclusively, the gradients enable the spatial encoding of the signal to probe the effective spin density at the given location. Following, spatially varying frequencies are probed in MRI, and Equation 2.5a is therefore extended to

$$\omega(\vec{r}) = \gamma B(\vec{r}) \tag{2.25}$$

with $\vec{r}$ describing the spatial coordinate along the direction of the applied gradient. Following, in terms of MRI, the Larmor frequency is a function dependent on the spatial location. It thus represents a spatial frequency, which offers the opportunity to obtain an image.[4]

Slice selection gradient

Conventional MRI acquires Two-dimensional (*2D*) slice snapshots; therefore, the RF pulse needs to be applied to a specific region along the z-dimension of the body. By applying a gradient along the z-direction of the patient, at the same time when the RF pulse is applied, the precession frequencies along z are linearly changed, which results in an offset that enables selection of a particular slice. The frequencies along z are thus given by

$$\omega(z) = \gamma(B_0 + G_z z) \tag{2.26}$$

with G_z representing the gradient amplitude along the spatial coordinate, z. Only the spins in the targeted slice precess with the Larmor frequency. Spins outside the slice of interest experience a linear frequency offset, which makes them unresponsive to the applied RF pulse. Hence, the RF pulse's frequency matches only the frequency of the selected slice and, thus, excites a pre-determined slice only. This imposes restrictions on the slice thickness, either determined by the bandwidth of the applied RF pulse and by the gradient's slope across the patient.

Three-dimensional (*3D*) sequences provide initially higher SNR due to volumetric excitation and do not leverage a slice selection gradient. These sequences excite the whole volume, and the re-emitted signal is gridded into partitions along z. Hence, the slice thickness, Δz, is given by

$$\Delta z = \frac{BW_{RF}}{\frac{\gamma}{2\pi} G_z} \tag{2.27}$$

with BW_{RF} being the bandwidth of the RF pulse. Notably, most sequences used for ^{23}Na MRI are 3D, thus leveraging volumetric excitation to counter the initially low SNR.

Frequency encoding gradient

In analogy to the slice selection gradient, spatial encoding along x is performed by applying an additional gradient with a constant amplitude after the slice selection gradient is turned off.

$$\omega(x) = \gamma(B_0 + G_x x) \tag{2.28}$$

The changed precession frequency along x is thus directly linked to the gradient's strength experienced by the spins. However, the frequency encoding gradient exhibits a continuous gradient amplitude, and the gradient's strength is defined by the gradient moment it accumulates over time. This gradient is applied continuously while the signal is detected and converted.

Phase encoding gradient

Finally, spatial encoding along the y-direction is performed by applying a third gradient, which also changes the precession frequencies concerning the spatial location of the spins. However, this gradient is only applied briefly before detecting the Magnetic Resonance (*MR*) signal. Due to the changed frequencies along the y-direction, the precession frequencies change, and after turning the gradient off, the selected fraction of the spins precessed faster than others, which results in a relative change of phase, ϕ. Hence, the phase difference is well known along the y-direction because the amplitude and the time of application of the phase-encoding gradient are known. The phase of the spins is related to the gradient according to

$$\phi(y) = -\gamma G_y y t \tag{2.29}$$

Applying the phase-encoding gradient results in a phase change, ϕ. This phase change extent is given by the gradient's amplitude, G_y, at the position, y, and by the time, t, which defines how long the gradient was superimposed over B_0.

k-Space

k-Space is the matrix structure in which the NMR signal is stored. By applying the gradients, the position in the k-space can be determined, and thus, the strength and or the duration of the gradient applied is directly linked to the position in the k-space matrix. Hence, a direct link between the k-space and the image domain exists. The gradients' relation to the position in the k-space is given by

$$\begin{aligned} x &= \frac{\omega}{\gamma G_x} \leftrightarrow k_x = \gamma G_x t \\ y &= \frac{\omega}{\gamma G_y} \leftrightarrow k_y = \gamma G_y t \end{aligned} \tag{2.30}$$

with k_x and k_y representing the x- and y-position in k-space, respectively. It is important to note that the position in k-space is directly linked to the applied gradient. In contrast, the information of a single point in the k-space matrix is related to all voxels in the image domain.

The k-space matrix can be arbitrarily filled, which leads to enhanced sampling strategies compared to standard Cartesian. Furthermore, k_{max} in the k-space represents the highest frequency sampled, determining the image domain's resolution. The entire width of the k-space matrix is given by $k_{FoV} = 2k_{max}$. Additionally, the spacing in k-space is defined by Δk_x and Δk_y for the spacings along x and y, respectively. The relations of k-space and image domain for these parameters are defined as

$$\Delta k = \frac{1}{FoV} \leftrightarrow \Delta x = \frac{1}{k_{FoV}} \tag{2.31}$$

with FoV representing the Field of View (FoV) and Δx, the pixel size in image domain with $\Delta x = \Delta y$. From Equation 2.31, it follows that the k-space and the image domain are inversely proportional, posing gradient and sampling restrictions for MRI. The Nyquist limits[6] for the gradients are given by

$$\begin{aligned} \Delta t &\leq \frac{2\pi}{\gamma G_x N_x \Delta x} \\ \Delta G_y &\leq \frac{2\pi}{\gamma t N_y \Delta y} \end{aligned} \tag{2.32}$$

Equation 2.32 shows that the frequency encoding gradient has to sample the signal rapidly. Since the frequency encoding gradient is usually played continuously, this criterion is always full-filled. However, the phase encoding gradient in y requires small steps to match the desired pixel size, Δy. As the phase encoding steps need to be repeated N-times, this is, with the repetition time, one of the most crucial parameters that determine the acquisition speed of MRI. Violating these sampling limits results in aliasing artifacts.

[6] See section Image reconstruction for the definition of Nyquist limit

Fourier transform in MRI

Referring to Equation 2.24 and Equation 2.30, by replacing $\rho(x) \leftarrow S(t)$ and $k_x x \leftarrow \omega t$, the time-dependency is substituted by spatial dependencies on x. Following, $\rho(x)$ represents a density function, which in MRI is the spin-density, and $k_x x$ represents the position in k-space, which is directly linked to the gradient. With $k_x = \frac{\gamma}{2\pi} G_x t$, this gives rise to the inverse Fourier transform (*iFT*) used in MRI as

$$\rho(x) = \int_{-\infty}^{+\infty} S(k_x) e^{i2\pi k_x x} dk_x \tag{2.33}$$

From Equation 2.33, it follows that the inverse Fourier transform of k-space yields the spin-density function, $\rho(x)$, representing the investigated nuclei's MR image[7].

Gradient Recalled Echo Sequence

One of the most commonly used sequence[8] is the Gradient Recalled Echo (*GRE*), Figure 2.4. Generally, a basic GRE sequence constitutes a single RF pulse, with flip angles from $\theta = 5...90°$, coupled with gradients used for spatial encoding of the MR signal. GRE sequences are implemented as 2D snapshots or 3D volumetric sequences. The frequency encoding gradient generates the echo in this sequence. First, the slice-selective gradient along z is applied, followed by the phase encoding gradient. Finally, the frequency encoding gradient is used to dephase the signal first and then rephrase it to produce a gradient-stimulated echo in the center of the Analog-to-Digital Converter (*ADC*)[9] at the Echo Time (*TE*), TE_i with i being the i-th echo. Following, the MR signal sampled with this sequence is governed by ${T_2}^*$ decay, and hence, the longer the echo time is, the more the signal is weighted towards ${T_2}^*$. Extending the GRE to a multi-echo GRE sequence, more efficient sampling of the ${T_2}^*$ signal curve can be realized. In this modification, the sequence consists of multiple echoes that sample the signal at different time points. In this case, the frequency encoding gradient creates multiple echoes by inverting the gradient moment. The MRI sequence used in this thesis is based on a basic 3D GRE sequence.

The idea of gradients is more intuitive when described in the meaning of building the k-space matrix. k-Space is defined as the matrix in which the MR scanner places the FID with the help of an ADC. In the case of Cartesian sampling, the slice selective gradient determines the height of the matrix, and the phase encoding gradient defines the row. Once this is set, the frequency encoding gradient determines the position from left to right to fill the selected line of the k-space matrix. In other words, the gradients determine the position in the k-space matrix where the FIDs are stored. For each repetition time, a single k-space line is acquired (only for Cartesian sampling), which is repeated until the whole k-space matrix is filled.

[7] Only the 1D Fourier Transform is described for simplicity since 2D or 3D reconstructions are cascaded one-dimensional (*1D*) Fourier transforms computed along the respective dimensions.

[8] Sequences are scripts that coordinate the timing of RF pulses, gradients, and signal acquisition parameters leading to a specific type of MR image.

[9] Analog to Digital Converter (ADC) is used to translate the analog signal (induced electromotive force) into a digital signal that can be processed further.

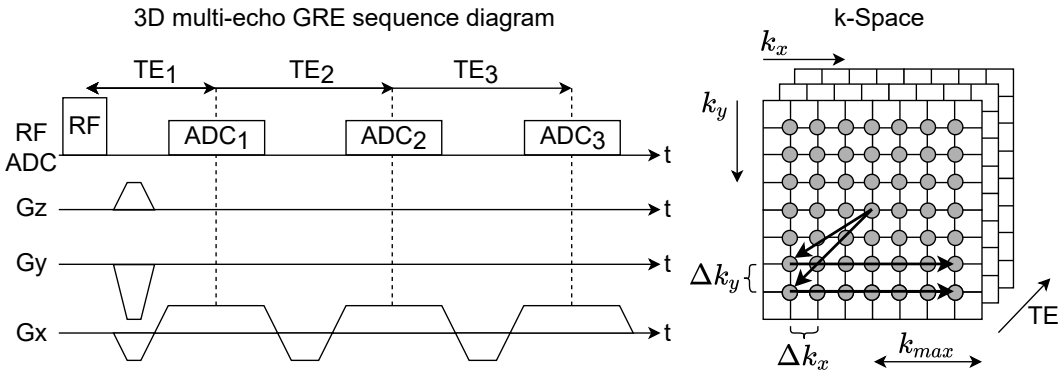

Figure 2.4: Sequence diagram of a 3D multi-echo GRE Sequence with the corresponding timing of each gradient and ADC. The corresponding k-space matrix construction is shown on the right.

2.3 Physics of the sodium nucleus

Other than ^{1}H, ^{23}Na is a 3/2 spin nucleus, which splits into four Zeeman levels when exposed to an external applied magnetic field, B_0, (Figure 2.1). Under certain conditions, Multi-Quantum Coherence (*MQC*) are observable, being superpositions between multiple quantum states. The quantum coherences for ^{23}Na are Single Quantum Coherence (*SQC*), Double Quantum Coherence (*DQC*), and Triple Quantum Coherence (*TQC*).[12] These MQCs are observed once the sodium nucleus is placed inside a heterogeneous environment where it interacts with the surrounding Electric Field Gradients (*EFGs*) of larger molecules. Therefore, probing MQCs could encode information about the molecular environment of the ^{23}Na nucleus.[12, 13]

Quadrupole interaction

Whereas the nuclear charge distribution for spin 1/2 nuclei is spherical, quadrupole nuclei exhibit an asymmetric charge distribution (Figure 2.5).[8] Consequently, rotations alter the electrostatic energy of the ^{23}Na nucleus.

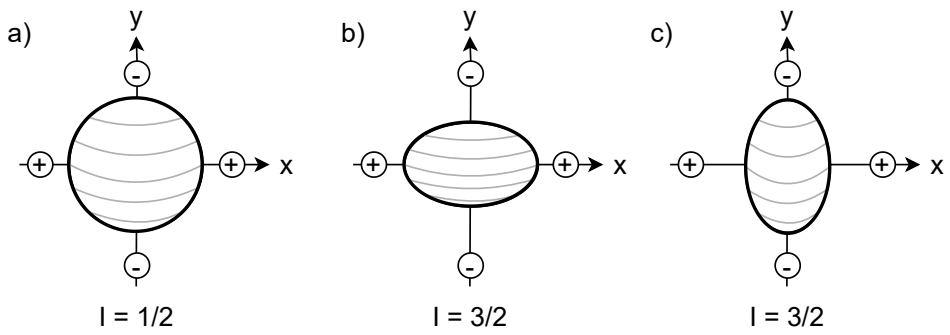

Figure 2.5: Nuclear charge distribution for nuclei with spin I=1/2 and I=3/2. For ^{1}H, the charge distribution is spherical (a), whereas ^{23}Na nuclei exhibit an asymmetric nuclear charge distribution. For spin I=3/2, the orientations can differ oblate (b) and prolate (c), with (c) being energetically favored.

Owed to the asymmetric charge distribution, the ^{23}Na nuclei also possess an electric quadrupole moment. Spins with I>0 experience dipole-dipole interactions, whereas spins with I>1/2 also exhibit electric quadrupole interactions. These lead to strong coupling to local EFGs, and indeed, relaxation for quadrupole nuclei is predominantly governed by the quadrupole interaction.[14] Consequently, quadrupole nuclei strongly interact with their molecular environment.

In isotropic environments, e.g. in fluids such as pure NaCl solutions, and when exposed to an external magnetic field, $B_0 > 0$, the ^{23}Na nucleus exhibits four equidistant energy levels (Figure 2.6, type d), which result in directly MR detectable SQC. This is observable in saline solutions, with the fluctuating quadrupolar interaction arising from short-term energy level splitting. As a result, the NMR spectrum is made of a single Lorentzian peak for type d. In biological tissue, e.g. in White matter (*WM*) or Gray matter (*GM*), the fluctuating interactions lead to two superimposed peaks, leading to a broadened spectrum for type c environments (e.g. biological tissue). In that case, the EFGs of surrounding molecules affect the ^{23}Na nuclei, enhanced due to the increased interaction time, and ultimately, giving rise to MQCs (Figure 2.1, Type c). Suppose the ^{23}Na nucleus is placed inside an anisotropic environment, e.g. crystal-like structure. In that case, the EFGs of surrounding molecules also affect the ^{23}Na nuclei, finally leading to residual quadrupole interaction (Figure 2.1, Type a). This split into static energy levels leads to distinct resonances, giving rise to multiple peaks at different frequencies in the NMR spectrum.

The extent of the EFGs affecting the ^{23}Na nuclei highly depends on the molecular environment and, thus, affects the ^{23}Na nuclei differently.[13] Depending on the correlation time, τ_c, the EFGs vary rapidly (extreme-narrowing regime, type d), e.g., in CSF, or slower in biological tissues, e.g., in WM or GM. For the first case, the T_2 relaxation behavior of ^{23}Na is solely described mono-exponentially. This corresponds to a single damped frequency, which gives rise to a single peak in the NMR spectrum. Outside the extreme-narrowing regime, the residual quadruple interaction gives rise to bi-exponential relaxation behavior described as

$$S_{23_{Na}} = 0.6e^{-\frac{TE}{T_{2f}^*}} + 0.4e^{\frac{-TE}{T_{2s}^*}} \tag{2.34}$$

with TE being the echo time, and T_{2f}^* and T_{2s}^* being the fast and slow components, respectively. In regards to brain ^{23}Na MRI, T_{2f}^* is in the order of 0.8 to 3 ms, and T_{2s}^* is in the range of 15 to 65 ms.[11] Again, Equation 2.34 demonstrates the importance of leveraging sequences with short echo times because most of the signal is governed by T_{2f}^*. With biological tissue being mostly heterogeneous, bi-exponential relaxation is predominantly observed.

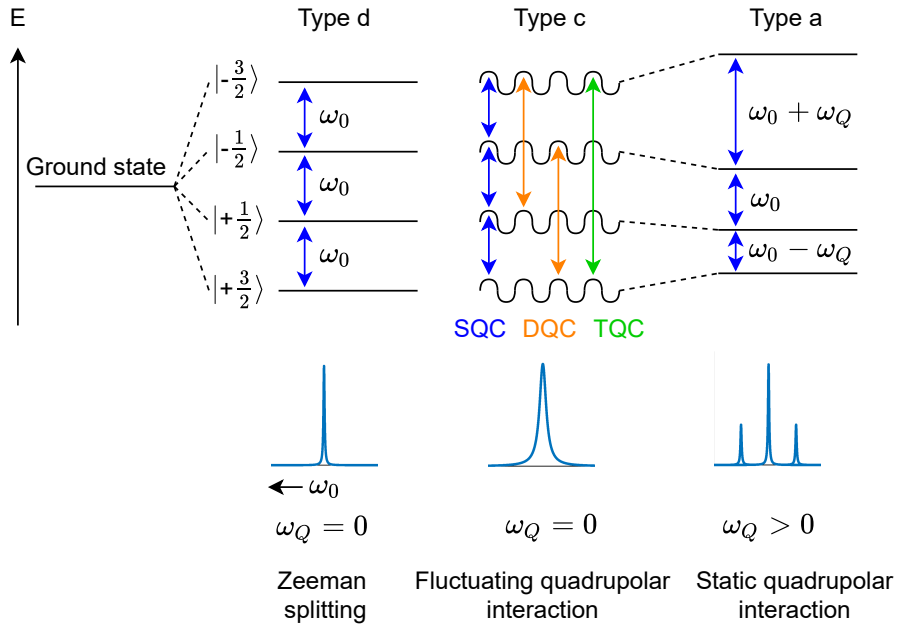

Figure 2.6: Splitting of energy levels of sodium (top) and the resulting NMR spectra (bottom) when exposed to different environments. Types d and c correspond to isotropic environments and type a corresponds to anisotropic environments. Adapted from [15] and [13].

Density operator and the Irreducible Tensor Formalism

The density operator contains information about the state of the quantum system. For spin systems I=3/2, the matrix consists of 16 elements, with the off-diagonals representing the coherences.

$$\hat{\sigma}_{I=3/2} = \begin{pmatrix} \sigma_{11} & \sigma_{12} & \sigma_{13} & \sigma_{14} \\ \sigma_{21} & \sigma_{22} & \sigma_{23} & \sigma_{24} \\ \sigma_{31} & \sigma_{32} & \sigma_{33} & \sigma_{34} \\ \sigma_{41} & \sigma_{42} & \sigma_{43} & \sigma_{44} \end{pmatrix}$$

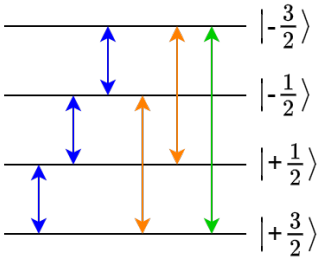

Figure 2.7: The density operator, $\hat{\sigma}_{I=3/2}$, for a spin ensemble of I=3/2 and the color-coded Zeeman energy levels with the MQCs, e.g., SQC, DQC and TQC.

The colors represent Zero Quantum Coherence (*ZQC*), SQC, DQC and TQC. At thermal equilibrium, the coherences between the states are zero[8] e.g., when the probe is placed inside B_0. If no additional magnetic fields are applied, the populations' sum is $\sum_i \sigma_{ii} = 1$, giving rise to ZQC only. Following, manipulating the magnetization enables probing coherences between energy levels and allows for MQC MRI.

To explain the complex NMR dynamics of quadrupole nuclei, in particular of ^{23}Na, the density operator, $\hat{\sigma}$, is expressed in terms of irreducible spherical tensor operators, $\hat{T}_{lm}$.[16, 17] The tensor formalism suffices to explain the dynamics of the spin systems' Hamiltonian[10] and the coherence evolution in MQC NMR sequences.

Similarly to the density operator, the irreducible spherical tensor operator basis, $\hat{T}_{lm}$ consists of 16 different operators (for ^{23}Na) with rank, $l = 0...3$, and coherence order $m = -l, -l+1...l-1, l$. The advantage of this tensor formalism is the rotation properties, which are very convenient when strong RF pulses are applied. It is important to note that hard RF pulses change the coherence order m, whereas the relaxation process changes the rank l of the spherical tensor operator.[8] The tensor formalism helps track the evolution of coherence when designing MQC sequences and enables a precise representation of the MQCs when RF pulses and relaxation alter the spin dynamics.[8]

Table 2.2: Irreducible spherical tensor operator for spin I=3/2 and the corresponding definition for each rank and coherence combination.

$\hat{T}_{lm}$	Description
$\hat{T}_{00}$	Identity
$\hat{T}_{10}$	Longitudinal magnetization
$\hat{T}_{20}$	Quadrupole magnetization
$\hat{T}_{30}$	Octupole magnetization
$\hat{T}_{1\pm1}$	Rank 1 SQC
$\hat{T}_{2\pm2}$	Rank 2 SQC
$\hat{T}_{3\pm3}$	Rank 3 SQC
$\hat{T}_{2\pm2}$	Rank 2 DQC
$\hat{T}_{2\pm3}$	Rank 3 DQC
$\hat{T}_{3\pm3}$	Rank 3 TQC

For further readings regarding the density operator and the irreducible tensor formalism, see [6, 8, 17, 18].

[10] The Hamiltonian operator, $\hat{H}$, represents the total energy operator of a given system, with the operator's eigenvalues corresponding to the allowed energy levels, and its eigenvectors representing the quantum states associated with the discrete energy levels.

2.4 Sodium Magnetic Resonance Imaging

Physiology of Sodium and Clinical Motivation

Sodium (^{23}Na) is an essential electrolyte involved in many physiological processes in the human body.[19] Foremost, it helps to maintain ionic homeostasis and regulates pH and transmission of nerve signals. Sodium is highly concentrated in the extracellular space ($\approx$ 140 mM) but less in the intracellular space ($\approx$ 15 mM). However, the intracellular volume fraction is around 80% of the tissues, with 20% being the extracellular volume fraction.[11] Hence, the concentration of the electrochemical gradient is pointing towards the intracellular space, which needs to be actively regulated by the Na^+/K^+ pump. Healthy cells can maintain this ion gradient, whereas an alteration of the energy supply leads to an imbalance of homeostasis and changes the intracellular sodium concentration.[11, 20] Conclusively, the sodium concentration is very sensitive to metabolic changes and could be used to distinguish healthy from malignant tissue.

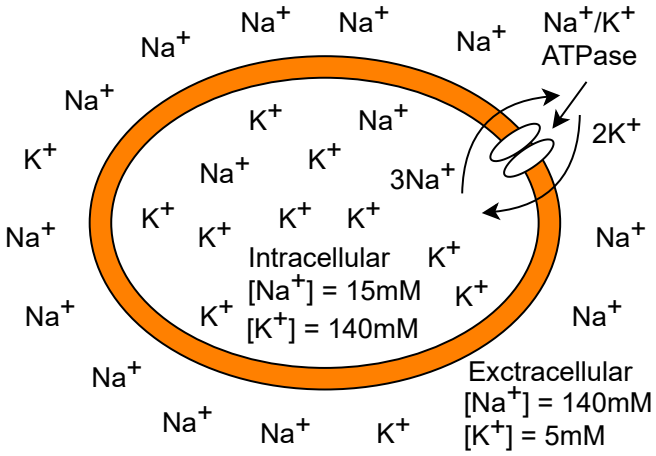

Figure 2.8: Simplified schematics of the sodium/ potassium pump (Na^+/K^+ ATPase) balancing homeostasis to maintain the ion concentration gradients.

Sodium MRI

Whereas ^{1}H MRI provides anatomical information, ^{23}Na MRI provides sensitive physiological information about the state of the tissue. Hence, sodium (^{23}Na) MRI is a promising tool to probe tissue ionic homeostasis, which in return could provide valuable information on tissue viability.[21–23] Sodium MRI is attractive for its unique specificity to directly characterize tissue ionic homeostasis from the linear correlation between the MR signal and the sodium concentration in vivo. Indeed, with proper calibration and Ultrashort Echo Time (*UTE*), ^{23}Na MRI can map apparent quantitative Tissue Sodium Concentration (*TSC*)[24–27].[28]

The cell's vitality is closely related to the sodium concentration and, thus, offers great potential to be a clinical marker for disease states.[11] Sodium MRI has been used to assess various types of cancer,[29] brain tumors,[30, 31] in neurodegenerative diseases such as Alzheimer's disease[32] or multiple sclerosis.[33, 34] Thanks to the advent

of ultra-high field (>=7 T) MRI and associated coil designs for dual-tuned $^{1}H/^{23}Na$ complementary imaging, ^{23}Na has received increased interest in recent years[11].[28]

However, ^{23}Na MRI is challenging since sodium exhibits very short relaxation times with T_2^* mainly being in the range of 0.8-5 ms. Special sequences that capture the rapidly decaying sodium signal efficiently have been developed. Typical sodium sequences constitute non-Cartesian sampling, e.g., non-linear k-space sampling that enables the start of sampling directly at the k-space center. This has the advantage that UTEs below 1 ms are achievable. Despite the advantage of short echo times, non-Cartesian sampling exhibits drawbacks, which lead to more complicated image reconstruction, worsened Point Spread Function (*PSF*), and susceptibility to gradient imperfections. Proper calibration of the image reconstruction framework and the gradient performance are essential, making non-Cartesian ^{23}Na MRI complicated. However, derived from Equation 2.5a, ^{23}Na MRI greatly benefits from increased field strength, which makes sodium MRI an exciting and essential research tool at ultra-high field scanners (>3 T).

2.5 Multi-Quantum Coherences Magnetic Resonance Imging

Besides the TSC estimation, ^{23}Na MRI enables MR contrasts that could further provide information about the tissue's health status. Due to sodium's 3/2 spin, Triple Quantum (*TQ*) coherences arise from the biexponential relaxation observable in slow-motion regimes such as WM and GM and are susceptible to the nucleus' molecular environment.[13] The TQ signal of ^{23}Na holds promises for novel or complementary information to conventional ^{23}Na MRI. LaVerde et al.[35] showed that the TQ signal is sensitive to changes in the sodium surroundings earlier than standard ^{23}Na MRI. The TQ signal's amplitude scales linearly with the intracellular sodium concentration shown by Schepkin et al.[36] in rat hearts. ^{23}Na TQ imaging has been demonstrated in the brain,[15, 37–39] with a direct correlation to PET,[40, 41] the knee[42] and in spinal disc tissue.[43] TQ imaging of primary brain tumors has been demonstrated by Boada et al.[44]. It was proposed as a valuable tool to monitor intracellular sodium content changes related to neoplastic changes. Conclusively, studying the full ^{23}Na MR signal by leveraging MQC imaging techniques[15] to acquire Single Quantum (*SQ*) and TQ signal components jointly could provide more and novel information about the tissue, the macroscopic sodium environment and the cell's vitality overall.[28]

Unfortunately, probing sodium's MQCs is challenging and requires specialized sequences. A typical MQC sequence with the coherence pathways, utilizing the tensor formalism, is depicted in Figure 2.9. A ^{23}Na MQC MRI pulse sequence combines the effects of relaxation and RF pulses to excite and disentangle MQCs, converting them into an NMR-detectable signal. RF pulses change the coherence order of the tensor operators, whereas relaxation periods alter the rank. Hence, these sequences leverage three strong 90° RF pulses that are phase-cycled[11] and combined with evolution periods to select the coherence of interest.[8]

[11] RF phase-cycling is used to suppress unwanted signals. Alteration of the RF pulse's phase, in combination with adequate post-processing of the measured signal, enables cancellation or enhancement of a specific FID.[45]

The first pulse, α_1, excites the spins. Directly after the pulse, only T_{11} and $T_{1\text{-}1}$ coherences are observable, which correspond to the transverse magnetization in the xy-plane. In conventional ^{23}Na MRI, $T_{1\text{-}1}$ coherence is solely probed. However, to probe multi-quantum coherences, e.g., TQ coherences, an evolution period, τ_{evo}, is crucial for the MQCs to build up. Thanks to the evolution period, T_{11} and $T_{1\text{-}1}$ coherences evolve into T_{31} and T_{21}, and $T_{3\text{-}1}$ and $T_{2\text{-}1}$, respectively. The extent of MQC coherence build-up is determined by the length of the evolution period, τ_{evo}, and differs for biological tissues. After the evolution period, a second 90° RF pulse is applied to disentangle the MQCs from the SQ pathway, rapidly followed by a third 90° RF pulse that converts the MQCs back into an MR detectable signal, $T_{1\text{-}1}$. MQC sequences applied in pre-clinical settings also deploy a 180° pulse during evolution to counter B_0 inhomogeneities. However, this is not applicable for in vivo acquisitions due to the SAR restrictions.

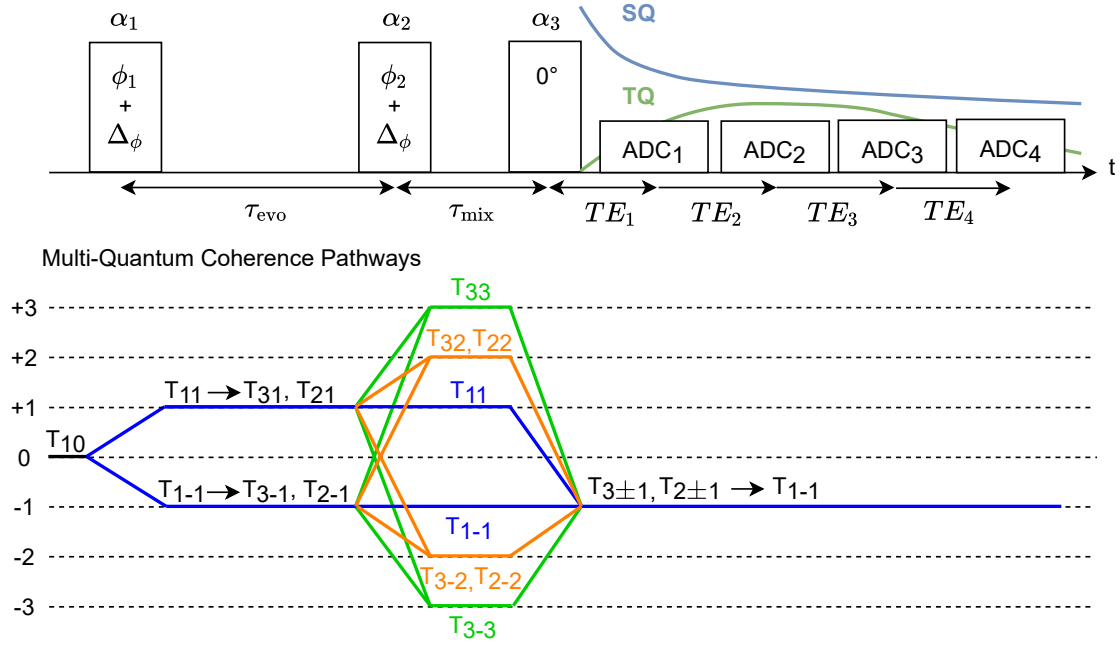

Figure 2.9: Pulse sequence with a multi-echo readout for probing multi-quantum coherences. Three strong RF pulses, α, coupled with appropriate phase-cycling, $\phi + \Delta\phi$, and adequate evolution periods, τ_{evo}, are needed to probe all the coherence paths of interest. The tensor formalism suffices to keep track of the quantum coherence pathway. Coherence pathways are color-coded representing: ZQC, SQC, DQC and TQC. Spatial encoding gradients are missing since they are equivalent, as shown in Figure 2.4.

The correct distinction of the MQCs from the SQ pathway is challenging, and there are two ways to do this effectively. The first one is termed Multi-Quantum Filtering (MQF). These sequences use the superposition principle by cycling the RF phases to annihilate unwanted signals. Hence, the MQCs are the desired signal, and these components constructively interfere. The final signal is the summation of the carefully selected components of interest. A drawback of this method is that only one signal of interest can be probed per phase-cycle, e.g., only TQ.

A different approach is based on SQ, Double Quantum (*DQ*), and TQ signal components oscillating at different frequencies. The ^{23}Na MQC signal (signal after the evolution time, before the second RF pulse is applied) is a superposition of SQ, DQ, and TQ signal components, each oscillating at different frequencies. These components can be separated by computing the 1D FT along the phase-cycle dimension. One advantage of this method is the ability to simultaneously detect both the SQ and TQ signals. Another advantage is that this sequence allows for TQ signal quantification by normalizing the TQ signal with respect to the SQ signal. The TQ/SQ ratio is another contrast that could provide additional information and holds the potential to quantify the TQ signal, potentially extending TSC information. This type of sequence was used in this thesis. The RF phase-cycling concept followed by the Fourier transform is depicted in Figure 2.10.

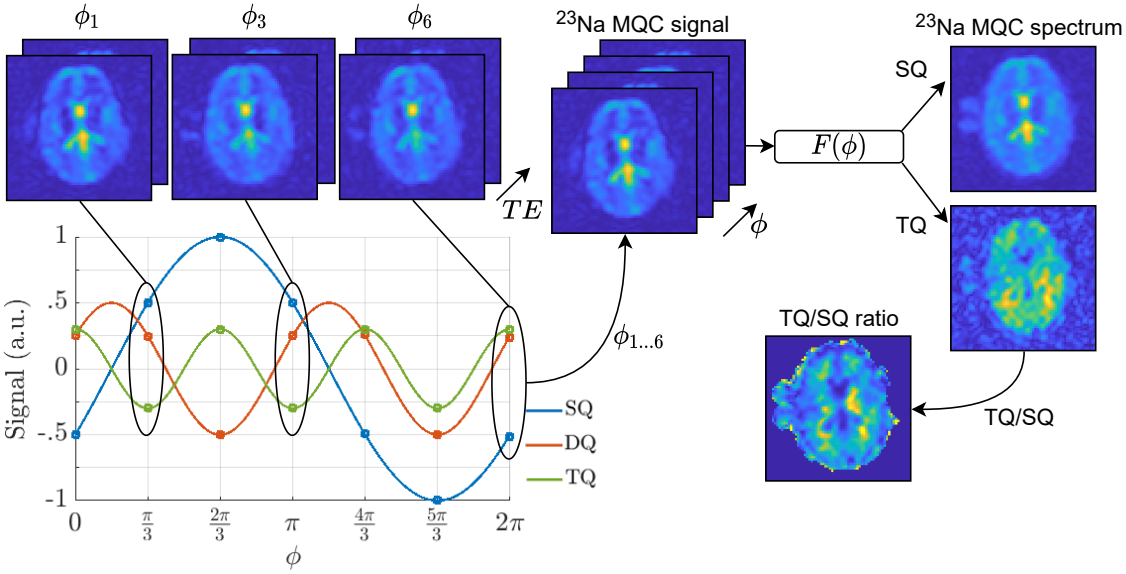

Figure 2.10: Superimposed phase-cycled ^{23}Na MQC signal. Leveraging RF phase-cycling samples the signal at different positions, e.g., ϕ_1. This results in volumetric acquisitions along the echo time, TE, with the same phase. The oscillating signal consists of multiple underlying signal components, with the TQ signal component oscillating at a frequency three times higher than the SQ signal. When a full phase-cycle was acquired, $\phi_{1...6}$, computing the Fourier transform along the phase-cycling dimension, $F(\phi)$, reveals the ^{23}Na MQC spectrum (SQ and TQ). Computing the ratio of both images, the TQ/SQ ratio provides an additional quantitative parameter and could reveal additional tissue information and, thus, potentially extend conventional TSC estimation.

Since 180° RF refocusing pulses are unsuited for in vivo ^{23}Na MQC MRI, different methods have been developed to counter B_0 inhomogeneities. Fleysher et al.[46] proposed to acquire two data sets, χ_0 and χ_{90}, with 90° phase offsets between each data set. Both data sets are combined to regain otherwise lost signal by leveraging the quadrature combination.

^{23}Na MQC MRI is a challenging imaging procedure with the hurdles foremost given by:

1. Suffers from low NMR sensitivity and, hence, low SNR
2. Inherently slow due to RF phase-cycling
3. Limited in spatial resolution due to slow acquisition speed
4. In vivo application restricted by SAR
5. TQ signal being susceptible to field inhomogeneities

However, there are strong motivations to evaluate sodium characterization in vivo. Still, all the hurdles mentioned above have made this feat scarce, albeit the promising results in the few published studies. Therefore, ^{23}Na MQC MRI could significantly benefit from advanced sequences and reconstruction frameworks, leading to faster and better resolved whole-brain sodium quantitative imaging.

2.6 Image reconstruction

MRI is generally known for lengthy acquisitions, so robust acceleration techniques are warranted. However, MR acceleration is limited by several factors, including hardware and signal sampling restrictions, which will be discussed in the following sections.

Acceleration

Sampling the MR signal is restricted by fundamental signal processing theorems, foremost limited by the Nyquist-Shannon sampling theorem.[47] This theorem states that a given signal, $x(t)$, which contains frequencies no higher than Ω_{max}, is sufficiently defined by sampling points taken with a spacing of $1/(2\Omega_{max})$. This theorem imposes sampling restrictions onto the MR signal, guaranteeing perfect signal reconstruction only if the sampling frequency, f_s, is at least $f_s > 2\omega_{max}$. If the theorem is violated, meaning an insufficient sampling density was used, the FT reconstructed signal exhibits aliasing artifacts, which lead to erroneous reconstructions. The sampling density and the highest frequency of the signal of interest highly limit MRI acceleration potential. Since the MR signal is sampled in the frequency domain, the sampling density, Δk, must be chosen adequately to enable accurate FT reconstruction. However, acceleration is only achieved by skipping phase-encoding lines, which changes the sampling density, Δk.

The captured MR signal is related to the image by computing the inverse Fourier transform. As described, the FIDs are stored in the k-space matrix, representing the frequency domain signal. k-Space exhibits a crucial structure with the contrast information stored at the k-space matrix's center. These are low-frequency components and contain most of the signal's information but lack the information about finer structures such as edges. The detailed information is encoded in the high-frequency components located at the periphery of the k-space matrix. However, both components must be adequately sampled to guarantee accurate image reconstruction (Figure 2.11) when only a simple forward model, such as the FT, is used. The inverse Fourier-transformed signal is considered the MR image.

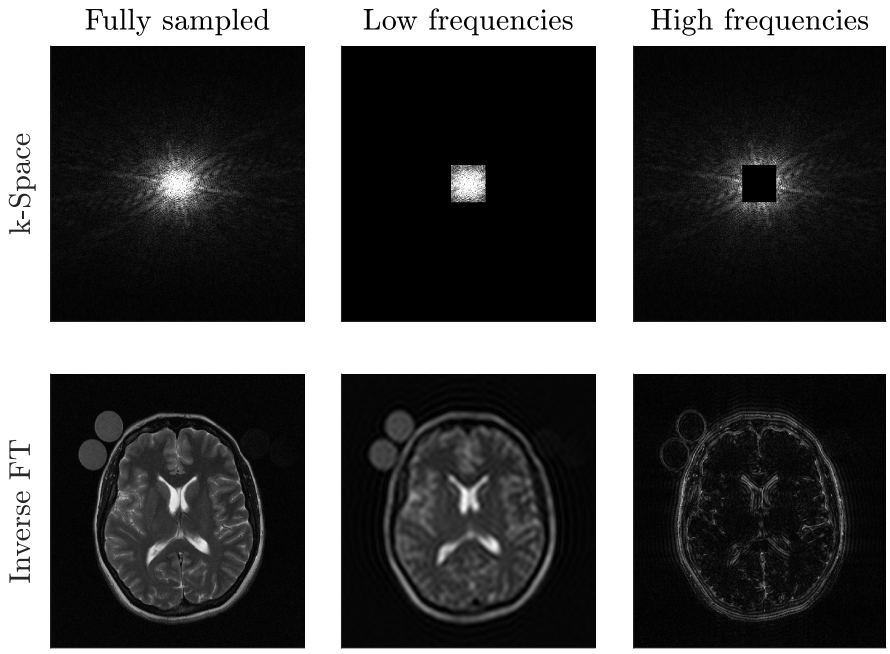

Figure 2.11: In MRI, the acquired k-space is related to the image domain via an inverse Fourier transform of the k-space matrix (shown in the top row). Low frequencies are concentrated in the center, whereas high frequencies are stored at the edges of the k-space matrix. Both frequency components are needed to guarantee accurate image reconstruction when using a simple iFT.

However, leveraging prior knowledge enables the reconstruction of the undersampled MR signal aliasing-free. Partial Fourier samples only a fraction (typically 70%) of the phase-encoding steps and reconstructs the missing lines by exploiting k-space symmetry.[48] More advanced techniques utilize dedicated hardware multi-receive coils to exploit redundancy in the data. Predominantly used are Generalized Autocalibrating Partially Parallel Acquisitions (GRAPPA[49]) and Sensitivity Encoding (SENSE[50]). These reconstruction techniques compute a kernel that generalizes the linear relationship between multiple images to synthesize missing lines. Unfortunately, these techniques are limited to multi-receive coils, which are rare for sodium MRI. Therefore, this thesis investigated algorithms to accelerate ^{23}Na MQC MRI based on sparsity assumptions or low-rank projections that do not rely on specific hardware.

2.6.1 Sparse image reconstruction

An efficient way to reconstruct undersampled signals is based on sparse representations. In mathematical terms, a matrix, A, with $m \times n$ elements and each element denoted as a_{mn}, is considered sparse when most elements are 0. Hence, only a few coefficients are needed to express most of the data variance.[51] In this thesis, sparsity is defined as most of the matrix's entries have to be close to 0 to be considered sparse.

Compressed Sensing (*CS*)[52–54] is a reconstruction technique that allows for accelerated MRI while maintaining decent image quality and has been successfully used for many years. The paradigm states that under the assumptions of incoherent

subsampling and a transform domain in which the signal is sparse, the signal can be almost perfectly recovered from a fraction of the sampled points,[53] even if one is far below the maximum frequency bandwidth determined by the Nyquist-Shannon-Theorem. The assumption of sparsity affects the k-space sampling, too. If the data is sparse in a transform domain and thus only a few coefficients are needed to express most of the data variance, this prior knowledge can be leveraged to obtain a fraction of the data in the first place. Following, the assumption of sparsity during MR signal sampling reduces the redundancy of the acquired data and, therefore, enables acceleration of the acquisition.

Most signals are not intrinsically sparse and must be made sparse using an adequate transform, e.g., Wavelet transform[55, 56] (WT). These transforms decompose the input signal into basis functions that can be recombined to approximate the original signal. In general, the transform enables chronological sorting of the contributions of each basis function from most important (expressing most of the variance) to least important (only representing a small portion of the overall data variance). Low-frequency components express most of the signal's variance, whereas slight variance is expressed by high-frequency components, e.g., noise or detailed information like edges. Cutting out on the small basis functions results in a reduced amount of retained information. However, these small values mostly contain noise and do not contribute substantially to the final signal. Nevertheless, thresholding too many values will result in blurry images since detailed information is missing.

In terms of undersampling, leveraging sparsity reduces the complexity of the reconstruction problem and, in return, helps to find a better solution to the optimization problem. It is important to note that the SNR in this transform domain determines the quality of the reconstruction. The easier it is to distinguish between the signal of interest and unwanted noise or interference, the easier it is to set appropriate reconstruction parameters and thus improve the reconstruction results.

The idea of sparsity has been introduced in MRI by Lustig et al.[57] to reconstruct undersampled MR images. CS leverages sparsity with the three major components involved in the reconstruction being:

1. Incoherent undersampling
2. Sparsity and thresholding
3. Non-linear reconstruction that includes the sparsity regularization and fidelity to the sampled data

The first prerequisite of CS is incoherent undersampling. Regarding MRI sampling, k-space sampling is a crucial part and determines the quality of the reconstruction. Coherent subsampling of k-space leads to folding artifacts, given by the relation of $\Delta k = 1/FoV$. An acceleration factor of R=2 leads to $\Delta k_{R=2} = 2\Delta k$, which reduces the field of view by a factor of 2 — conversely, incoherent subsampling leads to noise-like artifacts (Figure 2.12). Subsequently, undersampling the high-frequency information more drastically while sampling the low-frequency components more densely is termed Variable Density (*VD*) undersampling. VD undersampling represents an efficient sampling strategy to accelerate MRI.[57]

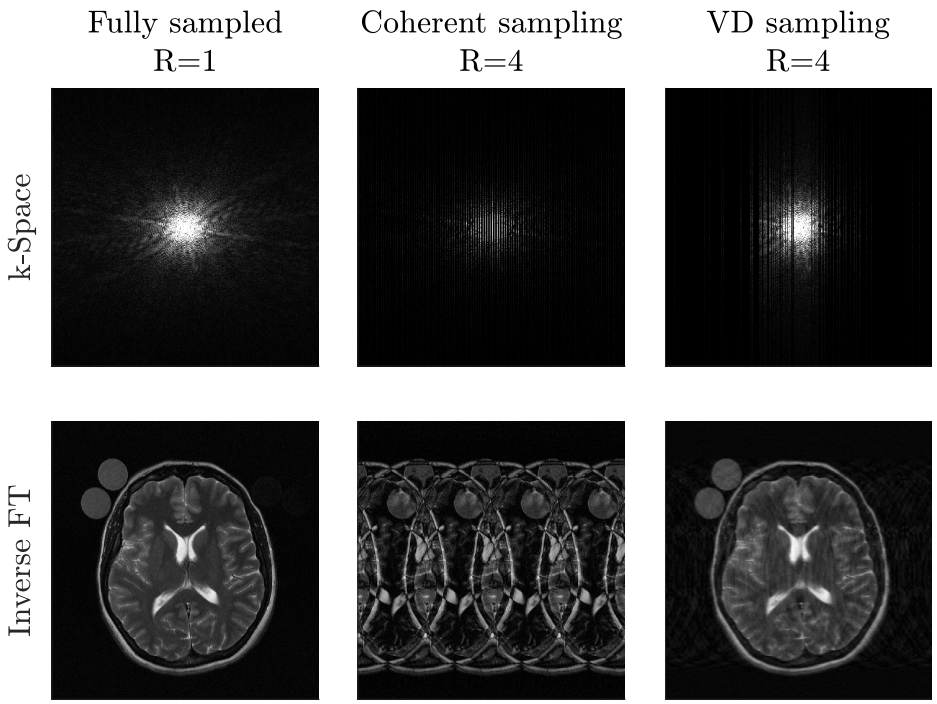

Figure 2.12: Acceleration factor of R=4 with Cartesian sampling was used. Coherent k-space sampling leads to folding artifacts. Leveraging prior knowledge of the k-space structure, variable density enables sampling of low-frequency components with higher density than high-frequency ones, yielding noise-like (incoherent) artifacts.

Sparsity and thresholding

Sparsity in MRI is a concept to compress the data to remove unnecessary image information, e.g., noise, and only to retain important imaging features. Computing an inverse FT of the undersampled k-space results in aliased images, which appear to be noise-like. Hence, an assumption can be made that the noise-like artifacts are treated as noise; therefore, denoising techniques can be leveraged to remove those. A conventional denoising technique is based on thresholding operations, which retain signal components above a certain threshold and penalize everything below the threshold.

The probed signal can be regarded as a superposition of the actual signal, $S(t)$, and the noise, η, following: $S_\eta(t) = S(t) + \eta$. If η is known, shrinkage operations can obtain the optimal values representing the signal by applying a threshold, λ, with $\lambda = \eta$. The hard thresholding function sets values below λ to zero and, thus, does not affect values $> \lambda$.

$$\text{Shrinkage}(x) = \begin{cases} x & \text{if } |x| > \lambda, \\ 0 & \text{otherwise.} \end{cases} \tag{2.35}$$

λ must be determined with caution not to remove signal components of interest but to adequately remove noise-like artifacts. The concept of signal, noise, and thresholding is shown in (Figure 2.13).

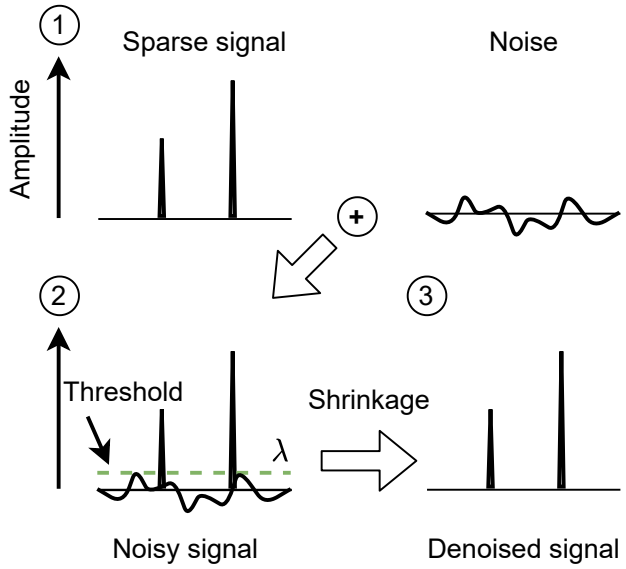

Figure 2.13: Real-world signals are a superposition of the signal of interest and noise (1). Thresholding the superimposed signal removes the bias introduced by noise (2), yielding a denoised signal (3). This concept is used in Compressed Sensing to cut out the undersampling-related artifacts and to reduce the complexity of the optimization problem.

Other than the signal shown in Figure 2.13, MR signals after applying the inverse FT are not intrinsically sparse unless time-of-flight[12] MRI was acquired. Therefore, the signal to reconstruct is transformed to become sparse, e.g., leveraging a Wavelet transform[13]. Thanks to the transform, identifying the basis functions that express most of the data variance is straightforward. Hence, thresholding is utilized only to retain the most essential information (Figure 2.14). This way, the complexity of the optimization problem is significantly reduced, and optimal values are found by shrinkage operations[14].

Non-linear reconstruction and regularization

CS is a non-linear iterative reconstruction algorithm that tries to solve an optimization problem by exploiting sparsity in a suited transform domain. The optimization problem contains a term that exploits sparsity and a data fidelity term that ensures that the new solution remains consistent with the sampled points.

[12]Time of flight angiography is an MRI technique to visualize the vascular system, without the need of additional contrast agents. Only the vessels appear bright, making these images intrinsically sparse.

[13]Similar to the Fourier transform, Wavelet transform enables representing a time-dependent signal as a combination of basis function, e.g., Wavelets. These wavelets represent functions that can be time-shifted, elongated, or compressed to represent various frequencies. A Wavelet analysis decomposes the given signal multiple times into low and high-frequency components while retaining the information.

[14]Shrinkage operations refer to methods that reduce the values toward 0, e.g., hard thresholding. In terms of complex signals, the shrinkage operation is performed on the complex conjugate.

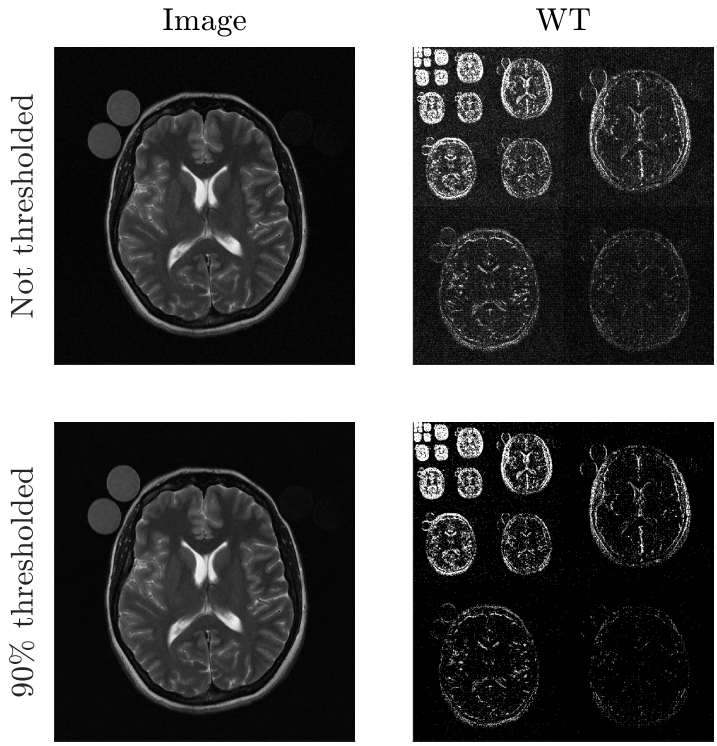

Figure 2.14: Hard thresholding with only 10% of the largest Wavelet transform (WT) coefficients preserved. MR images are highly sparse in suited transform domains but are not always intrinsically sparse.

Finally, optimal reconstruction results are only obtained by setting appropriate regularization parameters[15]. Regularization parameters include the number of iterations, weightings for the sparsity, and the data fidelity term and threshold values. Especially sparsity needs to be balanced to avoid excessive removal of signal information. Setting these parameters is challenging and usually requires extensive study. Therefore, methods have been proposed to set these values automatically.[58]

The complexity of the regularization scales with the dimensions involved and makes multi-dimensional CS challenging. It is important to note that the more prior information about the signal is known and included in the CS algorithm, the more accurate the iterative reconstruction will be. Additionally, it might converge faster to the optimal solution as it constrains the optimization complexity. Even though CS highly relies on the reconstruction parameters, once these values are set, CS' potential to recover signals only from a fraction of the required points is outstanding and a powerful method to accelerate MRI.

[15]Regularization refers to terms/ methods that penalize the objective function one tries to optimize. The regularization terms are added to improve reconstruction results. However, this increases the complexity of the optimization problem and requires careful selection of reconstruction parameters, e.g., weighting of the contribution of these terms.

Compressed Sensing in MRI

In general, sparsity MRI reconstruction, formulated as sparse MRI by Lustig et al.[57], is defined as an optimization problem of the form:

$$\min_{\mathrm{u}} ||\Psi(u)||_1 \, s.t. \, ||\Phi_F(u) - f||_2^2 < \sigma^2 \tag{2.36}$$

The first term is a L_1 regularization term with u being the target image to reconstruct and Ψ the sparsifying transform operator, e.g., Wavelet transform. The second term corresponds to the data fidelity with Φ_F indicating the partial Fourier transform followed by random undersampling, f representing the measured data in the frequency domain, and σ^2 being the variance of the signal noise.[28] The CS algorithm is depicted in Figure 2.15. The Split Bregman method can solve this optimization problem efficiently, with u being a convex function.[59]

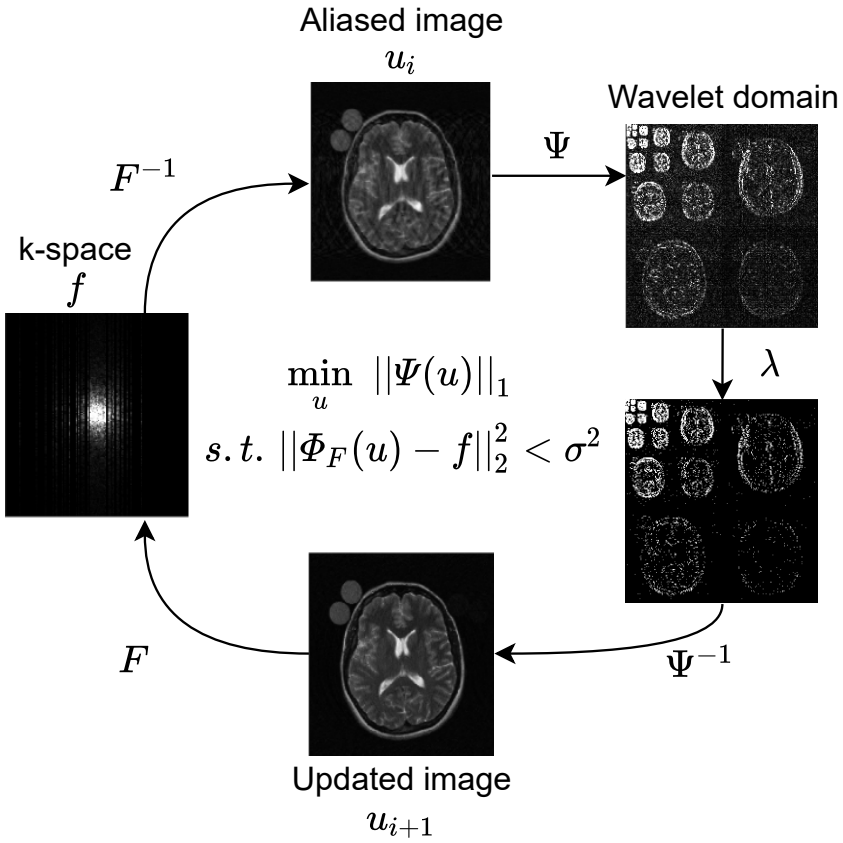

Figure 2.15: A standard CS algorithm leveraging the Wavelet transform as sparsity domain to reconstruct undersampled MRI. VD undersampled k-space, f, is inverse Fourier transformed, F^{-1}, exhibiting the corrupted image, u_i with i being the iteration index. Applying the sparsifying transform, Ψ, to the corrupted image, u_i, enables the identification of relevant structures to retain. Leveraging hard thresholding, with λ representing the threshold value, retains a small fraction (10%) of the initial values. Computing the inverse sparsifying transform, Ψ^{-1}, reconstructs a cleaner image, u_{i+1}, since the most variance of the data is expressed in the retained Wavelet coefficients. Lastly, u_{i+1} is Fourier transformed, F, and the new solution is updated with the acquired k-space lines to ensure data consistency (L_2 norm).

Split-Bregman Method

The Split Bregman Method (*SBM*)[60] iteratively solves constrained optimization problems[16] by leveraging regularization. The explanation given here is based on the work of Goldstein et al.[59] and Montesinos et al.[61]. Leveraging the Bregman iteration technique, it was shown by Yin et al.[62] that the optimization problem, e.g., the one given in Equation 2.36 for sparse MRI, can be split into multiple unconstrained subproblems:

$$u^{k+1} = \min_{\mathrm{u}} ||\Psi(u)||_1 \, s.t. \; \frac{\mu}{2}||\Phi_F(u) - f^k||_2^2 \tag{2.37a}$$

$$f^{k+1} = f^k + f - \Phi_F u^{k+1} \tag{2.37b}$$

with μ being a penalty function weight and ^{k} the iteration index. For each iteration k, the SBM solves and updates u in the frequency domain by applying the discrete Laplacian operator.

Using the image gradient is a common sparsifying transform approach known as Total Variation (*TV*) (Figure 2.16). Extensive details (e.g., noise) can be removed by minimizing TV, and the important features (e.g., edges) are retrieved. The Split-Bregman method is especially well-suited to minimize TV and is computationally efficient as it converges quickly when proper reconstruction parameters are chosen.[59] By replacing, Ψ, with the image gradient, ∇, as sparsifying domain, the L_1 regularization term of Equation 2.37a is rewritten as an isotropic 2D TV model:

$$||(\nabla_x u, \nabla_y u)||_2 = \sum_{i,j} \sqrt{(\nabla_x u_{i,j})^2 + (\nabla_y u_{i,j})^2} \tag{2.38}$$

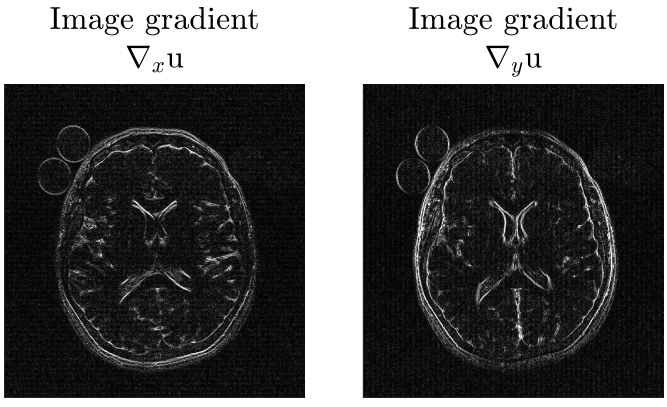

Figure 2.16: The first order derivatives, ∇, along x and y are shown. Computing the image gradient is a suitable sparsifying transform since only strong intensity changes are retained, reflecting important image features.

[16] SBM solves the constrained problem exactly for convex functions.[61] Convex functions exhibit a local minimum, which is also a global minimum. Finding the minimum of a convex function intrinsically represents the best possible solution, making it a desirable property for optimization problems.

Leveraging TV by replacing $d_x \leftarrow \nabla_x u$ and $d_y \leftarrow \nabla_y u$, the SBM can solve the problem stated in Equation 2.37a. Therefore, the problem is rewritten to apply the SBM with the Bregman updates as follows

$$\begin{aligned}\min_{\mathrm{u}} \; & ||(d_x, d_y)||_2 + \frac{\mu}{2}||\Phi_F(u) - f^k||_2^2 \\ & + \frac{\lambda}{2}||d_x^k - \nabla_x u - b_x^k||_2^2 + \frac{\lambda}{2}||d_y^k - \nabla_y u - b_y^k||_2^2\end{aligned} \tag{2.39}$$

d_x and d_y are complex-valued functions, with the optimal values computed by shrinkage operations. Two regularization terms are presented here, but additional regularization terms can extend the expression in Equation 2.39. The adaptation of SBM for ^{23}Na MQC MRI is given in Section 3.1.

SBM has the advantage that it provides an error cancellation effect, which yields fast convergence:

$$\begin{aligned}b_i^{k+1} &= b_i^k + (\nabla_i u^{k+1} - d_i^{k+1}) \\ f^{k+1} &= f^k + f - \Phi_F u^{k+1}\end{aligned} \tag{2.40}$$

with $i = x, y$ and b_i^{k+1} representing the Bregman updates. For each iteration, k, the SBM computes an updated solution for u and d. The errors of the optimized and newly computed u and d are added back into the constraints. It follows from Equation 2.39 that u and d are independent, enabling decoupling and solving them separately by differentiation and isotropic shrinkage operator.[61]

Solving for u first, the following subproblem is defined

$$\begin{aligned}u^{k+1} = \min_{\mathrm{u}} \; & \frac{\mu}{2}||\Phi_F(u) - f^k||_2^2 \\ & + \frac{\lambda}{2}||d_x^k - \nabla_x u - b_x^k||_2^2 + \frac{\lambda}{2}||d_y^k - \nabla_y u - b_y^k||_2^2\end{aligned} \tag{2.41}$$

Following Montesinos et al.[61], the complex expression in Equation 2.41 can be simplified to solve u in the Fourier domain as

$$u^{k+1} = F^{-1}(F(r^k)./K) \tag{2.42}$$

with $K = \lambda F(\Delta) + \gamma + \mu R$ where Δ represents the discrete Laplacian operator and F the n-dimensional Fourier transform.

Optimal values for d are obtained by leveraging isotropic shrinkage operations. First, the optimization problem for d is defined as

$$(d_x^{k+1}, d_y^{k+1}) = \min_{d_x,\, d_y} \; ||(d_x, d_y)||_2 + + \frac{\lambda}{2}||d_x^k - \nabla_x u - b_x^k||_2^2 + \frac{\lambda}{2}||d_y^k - \nabla_y u - b_y^k||_2^2 \tag{2.43}$$

and Equation 2.43 being efficiently solved by leveraging generalized shrinkage operations

$$d_i^{k+1} = max(s^k - \lambda, 0)\frac{\nabla_i u^k + b_i^k}{s^k} \tag{2.44}$$

with $i = x, y$ and s^k defined as

$$s^k = \sqrt{[(\nabla_x u^{k+1} + b_x) \times (\nabla_x u^{k+1} + b_x)^*] + [(\nabla_y u^{k+1} + b_y) \times (\nabla_y u^{k+1} + b_y)^*]} \tag{2.45}$$

and * representing the complex conjugate.

Conclusively, SBM decouples the L_1 and L_2 norms, which enables one to access each constrained function consecutively by minimizing each function separately. Shrinkage operations solve the L_1 subproblem, whereas the L_2 subproblem is solved analytically in the Fourier domain.[61] Hence, the Split Bregman method is well-suited explicitly for large optimization problems,[59] even though it is non-memory efficient when large-scale problems are solved.

2.6.2 Low-rank image reconstruction

The matrix, A, with size $m \times n$, with n spanning the columns, is considered low-rank when most columns are linearly dependent. Hence, the rank of a two-dimensional matrix reflects the degree of the linear dependence of its vectorized column space. The lower the rank of a matrix, with fixed matrix size $m \times n$, the more coherent the information is. The information can, therefore, be expressed as a linear combination of the column vectors in the matrix, A. In this thesis, the rank always refers to the column rank.

$$A_1 = \begin{pmatrix} 3 & 2 & 4 & 8 \\ 5 & 3 & 8 & 11 \\ 3 & 9 & 5 & 8 \\ 2 & 3 & 9 & 11 \end{pmatrix} \quad A_2 = \begin{pmatrix} 1 & 2 & 4 & 8 \\ 4 & 8 & 16 & 32 \\ 2 & 4 & 8 & 16 \\ 6 & 12 & 24 & 48 \end{pmatrix}$$

The given matrix, A_1, has a rank of 4 and is, thus, not of low rank. However, the matrix, A_2, is of low-rank with a rank of 1 since every column vector is a linear combination of the first column vector given. Similarly, this idea can be used in MRI to reconstruct undersampled k-space data. As shown in Figure 2.17, MR images' information is highly compressible and well retained in low-rank approximations. Similar to the sparsity concept, however, leveraging structural transforms can enhance the MR signal's low-rankness.

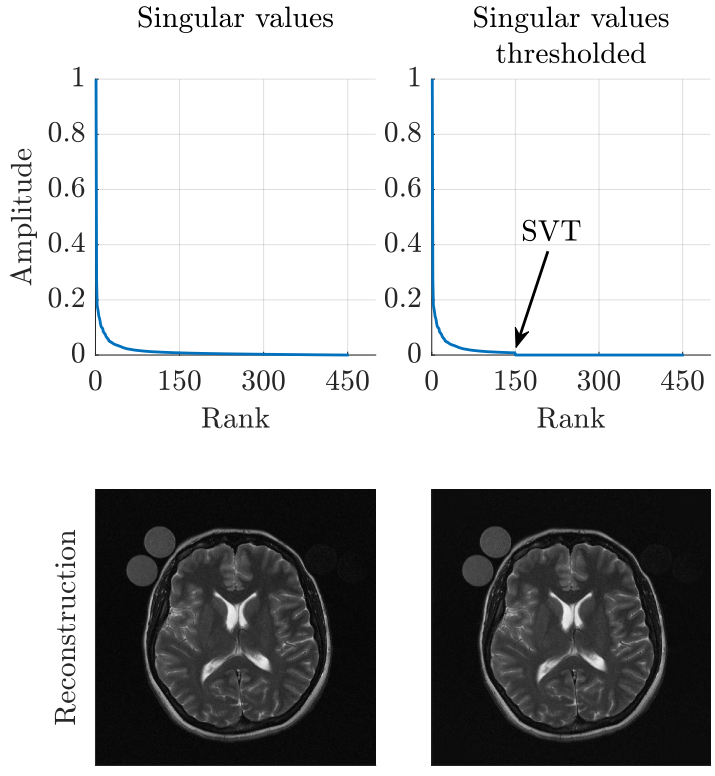

Figure 2.17: Original (left, rank=450) and low-rank approximation (right, rank=150) of a 2D MR image. Most image variance is concentrated in the large singular values, and thresholding (SVT) small numbers enables image compression without compromising image quality. In this example, only a third of the column vectors are retained.

Low-rank image reconstructions are closely related to sparse reconstructions and are also performed iteratively to solve the optimization problem. Whereas sparse reconstructions use a transform domain to obtain sparsity, low-rank reconstructions exploit coherent information by enforcing the low-rankness of the data. To reduce the rank of a matrix, A, a Singular Value Decomposition (SVD)[17] is computed. The main concept is identifying important singular values expressing most data variance (Figure 2.17). Following the idea of sparse reconstruction models, low-rank methods compute the singular values, which can be regarded as the 'sparsifying transform'. Thresholding those only to retain the largest values enforces low-rankness, termed Singular Value Thresholding (SVT). Only the largest singular values express the most data variance (Figure 2.17), enabling high data compression. Additionally, it reduces the complexity of the reconstruction problem. However, similar to sparse models, low-rank models solely approximate the optimal solution.

An example of highly coherent information in MRI is multi-echo snapshots. Multi-echo acquisitions in MRI are intrinsically low-rank[63] because they share information along the echo time. Therefore, the multi-echo data is well expressed by a linear combination of the vectorized snapshots arranged along the echo time. Most MR images' low-rankness can be further enhanced by reshaping the initial data structure into a highly structured matrix. The Hankel structure represents such a matrix and is often used in MR low-rank image reconstruction algorithms.

Hankel matrix

A Hankel matrix, A_H, is a structured square matrix with constant skew diagonals. Hence, a 5×5 Hankel matrix, A_{H5}, is defined as

$$A_{H5} = \begin{pmatrix} a_0 & a_1 & a_2 & a_3 & a_4 \\ a_1 & a_2 & a_3 & a_4 & a_5 \\ a_2 & a_3 & a_4 & a_5 & a_6 \\ a_3 & a_4 & a_5 & a_6 & a_7 \\ a_4 & a_5 & a_6 & a_7 & a_8 \end{pmatrix}$$

Regarding MRI, Hankel matrices are very useful for exploiting coherent information efficiently. Especially for highly multi-dimensional signals, the structured matrix exploits the redundancy across this multi-dimensional space. In other words, the multi-dimensional signal is projected onto a structured 2D space, which is enforced to be low-rank by computing an SVD followed by SVT. It is important to note that the computed Hankel matrix in this thesis exhibits a Hankel-like structure and refers to the Hanekl matrix of the k-space.

[17] Singular value decomposition is the eigendecomposition of a square matrix, A. It factorizes the given matrix A into $A = U\Sigma V^T$, thus enabling in-depth linear analysis of the system matrix. U is the unitary matrix, Σ are the singular values and V are the singular vectors. An SVD determines how much data variance is expressed by leveraging only a subset of U, Σ, and V.

Simultaneous auto-calibrating and k-space estimation

Simultaneous Auto-calibrating and k-space Estimation (*SAKE*)[64] is an MRI reconstruction algorithm that builds a structured Hankel-like matrix, A_H, which is enforced to be low-rank to synthesize missing data points (Figure 2.18). The algorithm tries to find an optimal rank of the matrix, A_H, that expresses the most variance in the data with the least amount of linear combinations of column vectors.

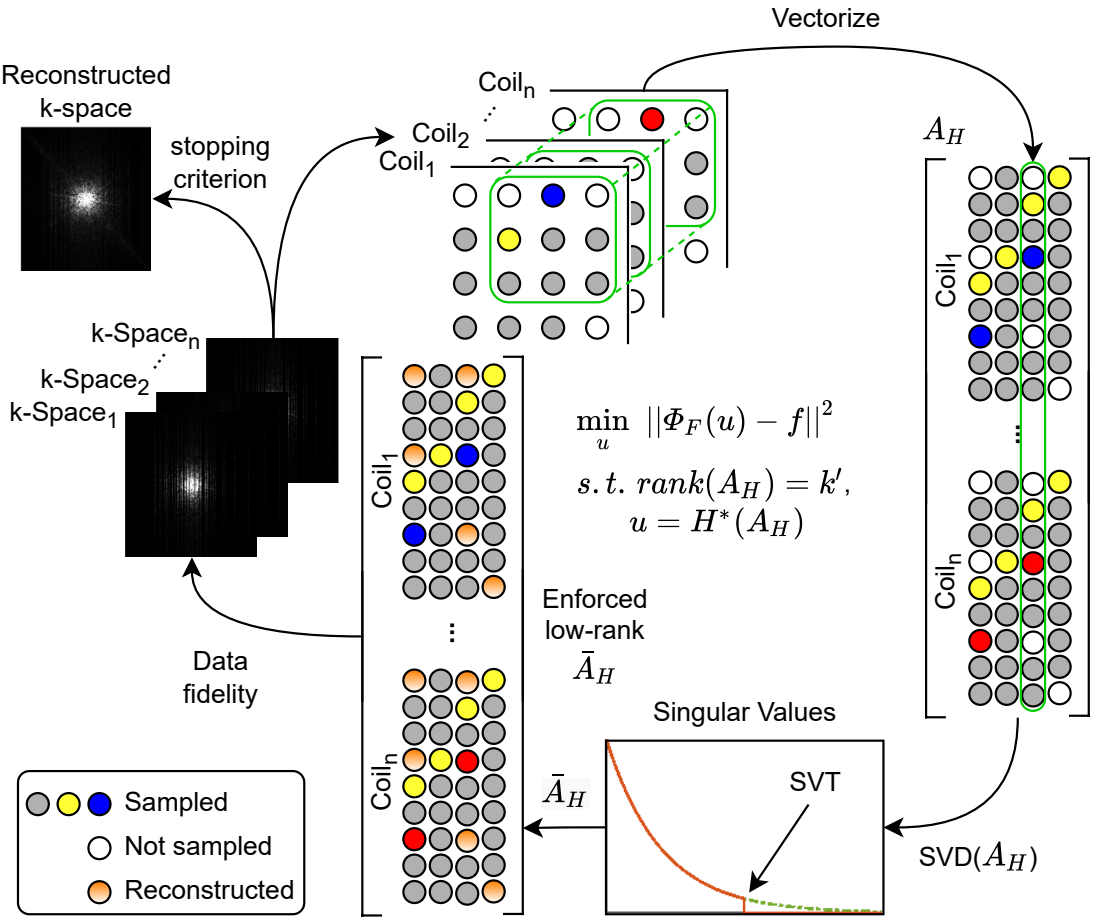

Figure 2.18: The SAKE algorithm reconstructs undersampled k-space data from multiple coil elements by exploiting redundancy. Undersampled k-space subspaces are vectorized into a 2D Hankel-like matrix by sliding a window across all k-spaces. Afterward, an SVD is computed to identify the linear correlations between the multiple subspaces, and by leveraging SVT, low-rankness is enforced to help synthesize missing data points. Finally, the matrix is reshaped into the initial k-space matrices' structures, and by ensuring data fidelity, the solution is iteratively updated. Optimization problem: u is the image one wants to reconstruct, Φ_F is the Fourier sampling operator relating reconstructed with acquired data, f, k' is a prior estimate of $rank(A)$ of matrix A_H, enforcing subspace SVD and H^* is the inverse structured matrix operator.

SAKE tries to solve the following optimization problem of the form:

$$\min_{u} ||\Phi_F(u) - f||^2 \;\; s.t.\; u = H^*(A_H), rank(A_H) = k' \tag{2.46}$$

with u being the image to reconstruct, Φ_F being the Fourier sampling operator relating reconstructed with acquired data, f, k' is a prior estimate of $rank(A_H)$ of matrix A, enforcing subspace SVD. H^* being the inverse structured matrix operator, see [64] and the l_2 norm enforces data consistency. SAKE was developed to exploit redundancy across multi-receive channels. Each receive coil, $\text{Coil}_{1...n}$, exhibits a small redundant sub-space of the original signal, $\text{k-space}_{1...n}$, spanned across all coil elements. Sliding a window across the k-space data, the redundant k-space is restructured with the columns spanning vectorized blocks of the window. The sliding window is moved line by line and, thus, creates a Hankel-like matrix structure. However, owing to the sliding window's finite size, these skew diagonal entries are not constant throughout the matrix.

Double Half-Echo k-space sampling

As described previously, SAKE is a reconstruction algorithm that leverages a highly structured matrix, and by enforcing the low-rankness of this matrix, missing data points are synthesized. However, another low-rank reconstruction framework used in this thesis also leverages structured low-rank matrices to combine two k-space halves. This method is termed Double Half-Echo (*DHE*).[65, 66]

Due to the very short relaxation times the sodium nucleus exhibits, sequences with short echo times are needed to sample the signal rapidly. Then, sodium sequences start sampling at the k-space center to capture most of the signal. Unfortunately, conventional Cartesian sampling is not optimal for UTE sampling. Strong dephasing gradients are needed to start sampling from left to right to fill the k-space matrix adequately (Figure 2.19). Playing the read dephase gradient prolongs the echo time. Hence, non-Cartesian sampling strategies are used that more efficiently cover k-space, e.g., Twisted Projection Imaging (TPI),[67] density-adapted radial,[68] or spiral sampling.[69] These acquisition strategies have the advantage of starting sampling at the k-space center, yielding very short TEs, and are not limited to sampling along a straight line. Despite their advantages of ultrashort echo times, these sampling techniques are highly susceptible to gradient system imperfections and provide slightly blurred images due to oversampling of the k-space center, which yields a degraded PSF.

Cartesian imaging remains one of the most SNR-efficient sampling strategies due to its equal coverage of low and high-frequency components in k-space. Unfortunately, conventional Cartesian imaging is limited by longer TEs, which is unsuitable for ^{23}Na MRI. However, despite using Cartesian sampling, the Double Half-Echo technique dramatically reduces the echo time by starting sampling from the k-space center. Hence, no or small read dephase gradients are needed, enabling the set of TE below 1 ms. However, a reverse (-kx) and a forward (+kx) k-space half must be acquired to form a full k-space line. Therefore, two readout gradients, G_x and $-G_x$, must be leveraged with reverse polarity (Figure 2.19). This increases the acquisition time by a factor of 2, but on the other hand, it provides valuable information about physical parameters such as B_0 inhomogeneities or gradient delays.[65]

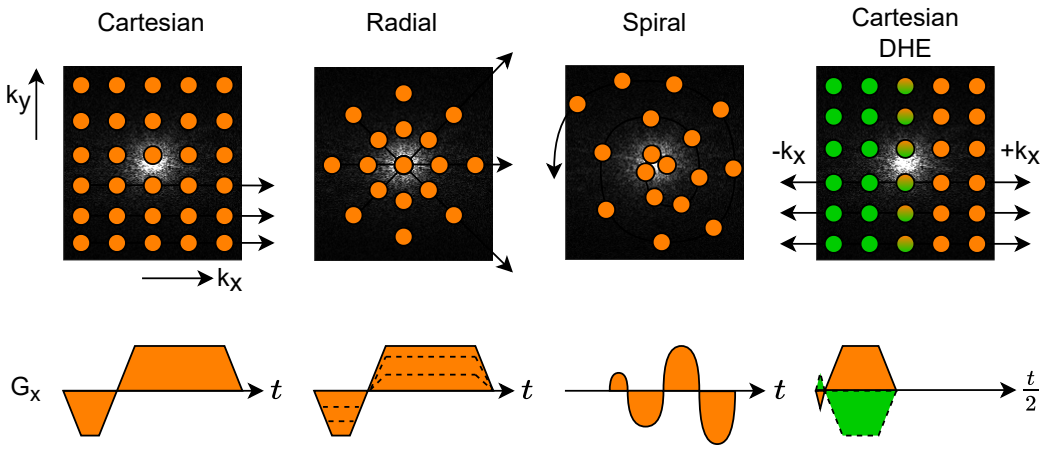

Figure 2.19: Cartesian and non-Cartesian sampling strategies with the respective read gradients. The orange dots represent sampling points obtained with the same gradient, whereas the green dots correspond to those sampled with reversed gradient polarity.

Gradient imperfections

Gradients determine the position in k-space. However, gradients represent a dynamic system of additional magnetic fields that can be turned on or off. Regarding ^{23}Na MRI, switching the gradients on should usually be performed in the shortest time possible to minimize signal relaxation. Following this, the ramp times of the gradients are minimized as much as possible. However, the gradient's amplitude is not consistently stable. After each ramp time, the gradient oscillates until it settles, and a static gradient amplitude is given. If these gradients suffer from slight imperfections, the resulting k-space position is biased by these imperfections, which results in a small offset of the actual k-space position. Following, sampling directly after the ramp time requires corrections of these gradient imperfections by, for instance, leveraging the gradient impulse response function, which is done in non-Cartesian acquisitions, or, to a certain extent, by leveraging a low-rank reconstruction framework, which was used in this thesis.

Image reconstruction of Double Half-Echo

As previously described, sampling the NMR signal right after the gradient's ramp-up results in k-space offsets from the gradient imperfections. However, a low-rank framework can be applied to correct for these biases. Image reconstruction of the DHE technique could be performed by manually inserting the two data sets into a shared k-space matrix. However, this results in corrupted images (Figure 2.20), which is owed to the gradient imperfections at the k-space center. Leveraging low-rank matrices helps concatenate both k-space halves adequately.

The reconstruction algorithm is based on structured matrix completion by leveraging the Hankel-like matrix structure. In particular, the structured Hankel-like matrix is similarly built as in SAKE, but to jointly exploit the coherent information across both k-space halves (Figure 2.21). Following, enforcing the low-rankness of the

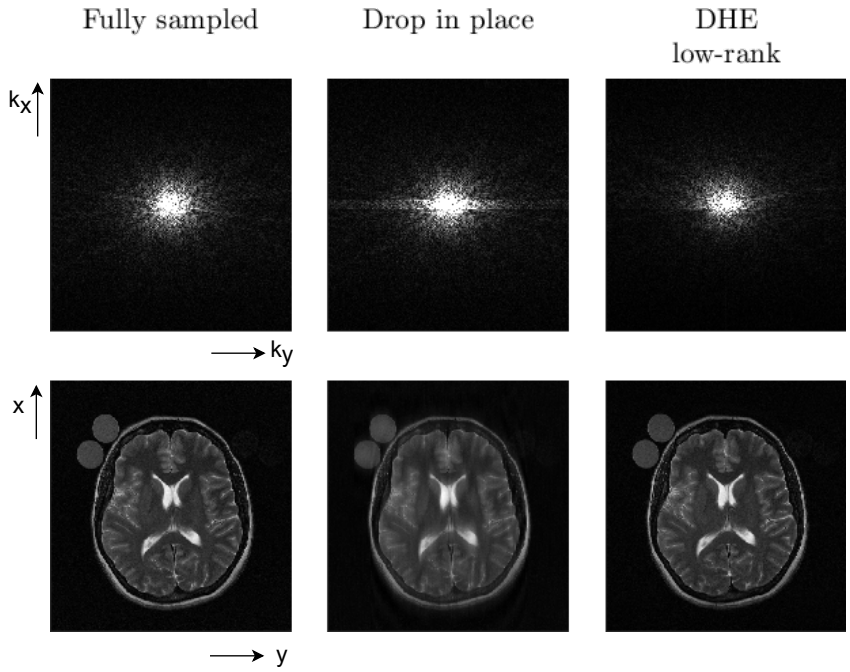

Figure 2.20: Reconstruction performance of manually (drop in place) inserting forward and reverse k-space halves, and by leveraging structured matrix completion (DHE) as proposed by Bydder et al.[65] Reconstructed k-space (top row) is inverse Fourier transformed to obtain the MR image (bottom row).

structured matrix enables the effective exploitation of the correlations along the rows. Thus, the framework provides an artifact-free reconstruction of both k-space halves.

Like SAKE, DHE low-rank reconstruction is an optimization problem that tries to minimize the rank of the structured matrix, A_H, and relates the measured data, f, to the reconstructed data, u with the optimization problem given in Equation 2.46. The algorithm uses both k-space halves, denoted as forward and reverse k-space. Both halves are vectorized by sliding a window across both k-spaces, yielding a column vector spanning all elements under the sliding window. This results in several column vectors in which the forward and reverse k-space halves are stacked. Therefore, some vectors contain shared information about adjacent k-space points of forward and reverse k-space halves, which can be efficiently exploited. Finally, the result is a structured matrix, A_H. The matrix's structure is associated with a block-wise Hankel matrix, with skew diagonal blocks repeating rather than individual values. Afterward, the SVD of the matrix, A_H, is computed to identify the most significant singular values and is then enforced to be of low-rank, $\bar{A}_H$, by leveraging SVT. Retaining only the most essential singular values compresses the data and reduces the complexity of the reconstruction problem. SVT minimizes the extent of the reconstruction artifacts that arose when both k-space halves were manually inserted into a single k-space matrix, e.g., drop in place method (Figure 2.20). Finally, the least squares problem between the newly reconstructed data and the initial solution is solved and fed back into the reconstruction algorithm, yielding both k-space halves aliasing-free reconstructed.

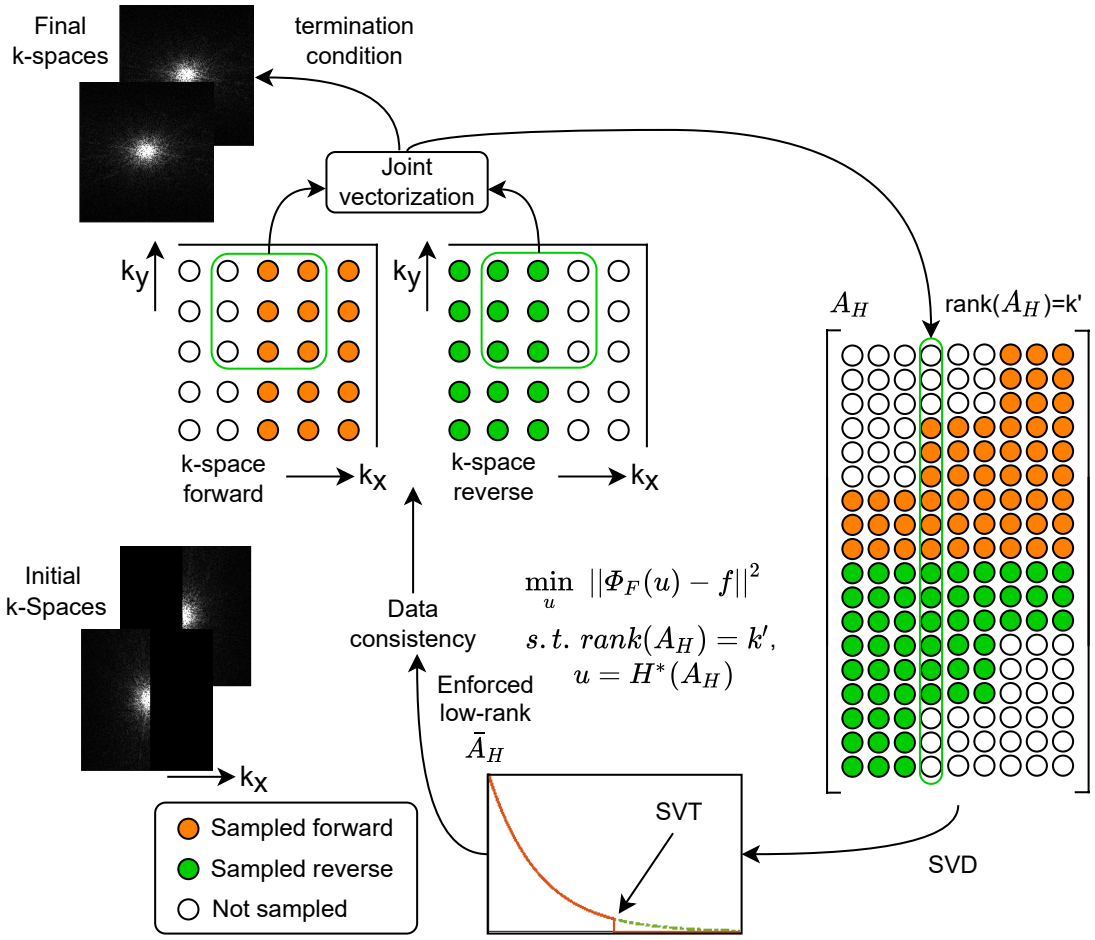

Figure 2.21: Image reconstruction and matrix formation for the DHE low-rank framework. Both k-space halves (forward and reverse) are reshaped into a Hanekl-like 2D matrix by consecutively sliding a window across both k-space halves. The vectorized k-space halves are stacked along the columns of the new matrix, with some vectors containing shared information about both k-space halves. An SVD of the Hankel-like matrix is computed, followed by SVT to enforce low-rankness. Lastly, the data is reshaped into its initial structure, yielding two k-space halves while ensuring data consistency. The solution is iteratively updated until the stopping criterion is met, which yields two fully reconstructed k-space halves. u is the target image, Φ_F representing the Fourier sampling operator, f the acquired data in k-space, H represents the structured matrix transform operator, with H^* being the inverse matrix transform operator and k' the prior rank of the data.

Conclusively, both low-rank frameworks (SAKE and DHE) exploit coherent information by creating a structured Hankel-like matrix. However, the main difference between both techniques is that the matrices fulfill different structural purposes. Whereas SAKE tries to synthesize missing data points by enforcing low rankness, the DHE framework exploits the coherent information across both k-space halves to minimize the extent of the artifacts arising from gradient imperfections. Nevertheless, both frameworks are non-linear reconstruction techniques that try to solve a similar optimization problem related to rank reduction.

3. Methods and Materials

This chapter introduces the experimental setups and has two sections with Section 3.1 covering sparse reconstruction and Section 3.2 explaining low-rank reconstruction for ^{23}Na and ^{23}Na MQC MRI. Parts of this chapter have been published in Licht et al.[28] and Licht et al.[70] by Wiley.

3.1 Multi-Dimensional Compressed Sensing reconstruction to advance ^{23}Na MQC MRI on clinical scanners

3.1.1 Image acquisition

3.1.1.1 Numerical simulation

^{23}Na MQC brain data were simulated based on a numerical phantom from Collins et al.[71] utilizing the Fleysher phase-cycle scheme.[46] Phantom brain data were resized via interpolation of nearest neighbor to approximate ^{23}Na MQC resolution with 7x7x10mm^3, resulting in a three-compartment model consisting of WM, GM and Cerebrospinal fluid (CSF). T_1 and T_2^* values for each compartment were assigned according to the literature as [24, 72]: (T_1/ T_{2f}^*/ T_{2s}^* in ms) for WM (34/ 3.4/ 18), GM (32/ 3.6/ 15) and CSF (55/ 51/ 51) with a magnetic field strength of B_0 = 3 T. ^{23}Na NMR dynamics were simulated by leveraging the irreducible spherical tensor operator formalism of Hancu et al.[73] and the evolution equations of van der Maarel[16] with hard pulse approximation. Random Gaussian noise with varying power defined as $P = mean(\eta^2)$ was added.

3.1.1.2 Phantom and in vivo

Imaging was performed on a NaCl/agarose phantom and 7 healthy volunteers at 3 T (4 volunteers) and 7 T (3 volunteers) MRI (Siemens MAGNETOM Trio and Magnetom, Erlangen, Germany) systems, each equipped with a 1Tx/Rx dual-tuned ^{1}H/^{23}Na head coil (3 T: RAPID Biomedical, Rimpar, Germany, 7 T: QED, Cleveland, OH, USA). According to the Declaration of Helsinki, a local ethical committee approved the study, and volunteers were recruited after providing written informed consent. A custom 3D multi-echo multi-quantum sequence termed CRISTINA [15] was used to obtain the single and triple-quantum filtered images with an optimized 2x6-step phase cycle.[74] Before each measurement, B_0 shimming was performed to minimize field inhomogeneities, and the flip angle of RF pulses was globally calibrated. CRISTINA evolution time for 3 T acquisitions was determined via a global TQ time proportional phase incrementation (TQTPPI[75]) spectroscopic prescan followed by a subsequent offline fit to map the TQ signal evolution over time to determine optimal echo sampling time. The evolution time for 7 T scans was pre-set to 10 ms.[74]

To validate accurate signal intensity reconstruction, fully sampled (R=1) images of a phantom consisting of 9 tubes (350 mL each) with varying agarose (0, 2, and 4%) and sodium (50, 100, 150-mM) concentrations were obtained. For 3 T in vivo acquisitions, a 2D anatomical ^{1}H T_1 scan was performed with a nominal resolution

Table 3.1: Sequence parameters for numerical simulations, phantom study at 3 T, retrospective in vivo study at 3 T, and prospective in vivo study at 7 T. *Hard pulse approximation was used.

Parameter	Numerical Simulation 3 T	Phantom 3 T	In vivo 3 T	In vivo 7 T
FoV (mm^3)	181x217x181	190x190x200	230x230x160	220x220x220
Matrix size	30x30x20	24x24x10	24x24x8	36x36x22
TE_1/ ΔTE (ms)	1.0/ 5.0	1.67/ 6.4	1.62/ 6.2	1.16/ 4.5
Bandwidth (Hz/px)	-	200	220	330
TR (ms)	200	150	150	196
Pulse duration (ms)	0*	0.5	0.5	0.7
Evolution time (ms)	10	12.1	10.1±2.12	10
Averages	1	17	11	7
TA (min)	-	2x60	2x31	2x34

of 1x1x5mm^3 within 4 min. For 7 T acquisitions, a prototype Compressed Sensing 3D anatomical ^{1}H MP2RAGE [76] scan was performed with a nominal resolution of 1x1x1mm^3 within 4 min. Four vials were placed next to the head, with concentrations of agarose and ^{23}Na of: (4%; 100 mM), (4%; 50 mM), (2%; 100 mM) and (2%; 50mM).

Numerical simulations, phantom, and 3 T in vivo data were retrospectively undersampled by factors of R=2 to 7, and in vivo 7 T data were prospectively undersampled by R=2. Additionally, one data set was more drastically undersampled with R=3, yielding a matrix size 30x30x26. 3D variable-density random sampling patterns, with undersampling solely performed along ky and kz, following a Poisson distribution[77] were used to retrospectively and prospectively undersample ^{23}Na MQC k-space data. Undersampling patterns were alternated along phase-cycling to enhance incoherence. The level of incoherence was measured by computing the number of points sampled at least once during the phase-cycling, divided by the size of the k-space matrix.

3.1.2 Image reconstruction

Split-Bregman method for accelerated ^{23}Na MQC MRI

Owed to the fact that only 3D ^{23}Na MQC MRI was acquired, the isotropic TV model defined in Equation 2.38 was extended to 3D giving rise to:

$$||(\nabla_x u, \nabla_y u \nabla_z u)||_2 = \sum_{i,j,l} \sqrt{(\nabla_x u_{i,j,l})^2 + (\nabla_y u_{i,j,l})^2 + \nabla_z u_{i,j,l})^2} \tag{3.1}$$

The CS algorithm proposed by Goldstein et al.[59] was used to develop the multi-dimensional CS model for accelerated ^{23}Na MQC MRI. It has been shown that optimal reconstruction results are achieved by exploiting sparsity in all imaging dimensions.[61] ^{23}Na MQC MRI involves multi-echo sampling paired with RF phase-cycling, which makes ^{23}Na MQC MRI a Five-dimensional (*5D*) signal structure.

Therefore, leveraging the multi-dimensional space of the signal by exploiting sparsity in each dimension separately improves image reconstruction results. Subsequently, the constrained optimization problem for ^{23}Na MQC MRI is formulated as

$$\min_{\mathrm{u}} \; |||\nabla_x u, \nabla_y u, \nabla_z u)||_2 + ||\Psi_{TE} u||_2 + ||\Psi_\phi u||_2 \;\; , s.t. \; ||\Phi_F(u) - f||_2^2 < \sigma^2 \tag{3.2}$$

Ψ_{TE} and Ψ_ϕ represent the sparsifying transforms, e.g., Fourier transform along the multi-echo and phase cycle dimensions, respectively. In analogy to Equation 2.39, replacing $d_{TE} \leftarrow \Psi_{TE} u$ and $d_\phi \leftarrow \Psi_\phi u$ allows to apply the SBM with the Bregman updates to the optimization problem stated in Equation 3.2 as follows:

$$\begin{aligned}
\min_{\mathrm{u}} \; & ||(d_x, d_y, d_z)||_2 + ||d_{TE}||_2 + ||d_\phi||_2 + \frac{\mu}{2}||\Phi_F(u) - f^k||_2^2 \\
& + \frac{\lambda}{2}||d_x^k - \nabla_x u - b_x^k||_2^2 + \frac{\lambda}{2}||d_y^k - \nabla_y u - b_y^k||_2^2 \\
& + \frac{\lambda}{2}||d_z^k - \nabla_z u - b_z^k||_2^2 + \frac{\lambda}{2}||d_{TE}^k - \Psi_{TE} u - b_{TE}^k||_2^2 \\
& + \frac{\lambda}{2}||d_\phi^k - \Psi_\phi u - b_\phi^k||_2^2
\end{aligned} \tag{3.3}$$

Again, d_{TE} and d_ϕ are complex-valued, with b_n^k for $n = x, y, z, TE, \phi$ being the Bregman updates at each iteration k. Consequently, the SBM solves and updates u and d iteratively, where the error in the constraint is added back. Following, to solve Equation 3.3 separately, it is decomposed into subproblems to solve u^{k+1} by differentiation and d^{k+1} by isotropic shrinkage operators according to Equation 2.44.

$$\begin{aligned}
u^{k+1} = \min_{\mathrm{u}} \; & \frac{\mu}{2}||\Phi_F(u) - f^k||_2^2 + \frac{\lambda}{2}||d_x^k - \nabla_x u - b_x^k||_2^2 \\
& + \frac{\lambda}{2}||d_y^k - \nabla_y u - b_y^k||_2^2 + \frac{\lambda}{2}||d_z^k - \nabla_z u - b_z^k||_2^2 \\
& + \frac{\lambda}{2}||d_{TE}^k - \Psi_{TE} u - b_{TE}^k||_2^2 + \frac{\lambda}{2}||d_\phi^k - \Psi_\phi u - b_\phi^k||_2^2
\end{aligned} \tag{3.4}$$

Meanwhile, spatial, temporal, and phase-cycle sparsity are introduced as individual regularization terms. Hence, they are solved separately as:

$$\begin{aligned}
(d_x^{k+1}, d_y^{k+1}, d_z^{k+1}) = \min_{\mathrm{d}} \; & ||(d_x, d_y, d_z)||_2 + \frac{\lambda}{2}||d_x^k - \nabla_x u^{k+1} - b_x^k||_2^2 \\
& + \frac{\lambda}{2}||d_y^k - \nabla_y u^{k+1} - b_y^k||_2^2 + \frac{\lambda}{2}||d_z^k - \nabla_z u^{z+1} - b_x^k||_2^2
\end{aligned} \tag{3.5}$$

$$s^k = \sqrt{\begin{aligned}&[(\nabla_x u^{k+1} + b_x) \times (\nabla_x u^{k+1} + b_x)^*] + [(\nabla_y u^{k+1} + b_y) \times (\nabla_y u^{k+1} + b_y)^*] + \\ &[(\nabla_z u^{k+1} + b_z) \times (\nabla_z u^{k+1} + b_z)^*]\end{aligned}}$$

with $(.)^*$ being the complex conjugate. Equivalently, the added regularization terms to exploit sparsity along multi-echo and phase-cycle dimensions are solved by leveraging the general shrinkage operations as defined in Equation 2.44, according to

$$\begin{aligned}
(d_{TE}^{k+1}) &= \min_{d_{TE}} \; ||(d_{TE})||_2 + \frac{\lambda}{2}||d_{TE}^k - \Psi_{TE} u^{k+1} - b_{TE}^k||_2^2 \\
(d_\phi^{k+1}) &= \min_{d_\phi} \; ||(d_\phi)||_2 + \frac{\lambda}{2}||d_\phi^k - \Psi_\phi u^{k+1} - b_\phi^k||_2^2
\end{aligned} \tag{3.6}$$

$$s_{TE}^k = \sqrt{[(\Psi_{TE}u^{k+1} + b_{TE}) \times (\Psi_{TE}u^{k+1} + b_{TE})^*]}$$
$$s_{\phi}^k = \sqrt{[(\Psi_{\phi}u^{k+1} + b_{\phi}) \times (\Psi_{\phi}u^{k+1} + b_{\phi})^*]}$$

Hence, the SBM for solving 2D regularized problems was further extended to 3D and, finally, to 5D to apply to ^{23}Na MQC MRI.

Multiple repetitions obtained with the same undersampling pattern were averaged before reconstruction. Each phase-cycle data set, χ_0 and χ_{90}, were reconstructed individually. The constrained optimization algorithm for 3D and 5D CS aims to solve the following problems:

$$\begin{aligned}
&\textbf{3D CS}: \min_u \ \lambda_p||(\nabla_x u, \nabla_y u, \nabla_z u)||_2 \ s.t. \ ||\Phi_F(u) - f||_2^2 < \sigma^2 \\
&\textbf{5D CS}: \min_u \ \lambda_p||(\nabla_x u, \nabla_y u, \nabla_z u)||_2 + \lambda_{TE}||\Psi_{TE}u||_2 + \lambda_{\varphi}||\Psi_{\varphi}u||_2 \\
&\qquad s.t. \ ||\Phi_F(u) - f||_2^2 < \sigma^2
\end{aligned} \tag{3.7}$$

with u being the target image to reconstruct, ∇ represents the first order derivative along the spatial dimensions, x, y and z, Ψ the Fourier transform along the temporal and phase cycle dimension and λ being the sparsity weighting parameter for spatial, $p = [x, y, z]$, multi-echo, TE, and phase-cycle dimension, ϕ. The optimal values for each regularization term were explicitly computed by leveraging shrinkage operations[59] that used different sparsity thresholds (β). The second term corresponds to the data fidelity with Φ_F indicating the partial Fourier transform followed by random undersampling, f representing the measured data in the frequency domain, and σ^2 being the variance of the signal noise. 3D CS reconstructed each 3D volume separately. The pseudo-code for the proposed 5D CS algorithm is given below.

Algorithm 1 Proposed CS algorithm for ^{23}Na MQC MRI based on Split-Bregman method.

Require: $f^0 = f, \hat{K}$
  while $\frac{||u^{k+1}-u^k||}{||u^k||} > 10^{-4}$ **do**
    $S^{k+1} = \lambda_p \nabla_x^T(\nabla_x u^k - bx^k) + \lambda_p \nabla_y^T(\nabla_y u^k - by^k) + \lambda_p \nabla_z^T(\nabla_z u^k - bz^k) +$
    $\lambda_{TE}\Psi_{TE}^T(\Psi_{TE}u^k - bTE^k) + \lambda_{\varphi}\Psi_{\varphi}^T(\Psi_{\varphi}u^k - b\varphi^k)$ ▷ S: Sparse components
    $rhs^{k+1} = (\mu\mathcal{F}^{-1}Rf)^k + \gamma u^k + S^{k+1}$
    $u^{k+1} = \mathcal{F}^{-1}(\mathcal{F}(rhs)./\hat{K})$
    $[x^{k+1}, y^{k+1}, z^{k+1}] = shrink_3(\nabla_x u^{k+1} + bx^k, \nabla_y u^{k+1} + by^k, \nabla_z u^{k+1} + bz^k, \beta_p)$ ▷ Thresholding
    $TE^{k+1} = shrink_1(dTE^{k+1} + bTE^k, \beta_{TE})$
    $\varphi^{k+1} = shrink_1(d\varphi^{k+1} + b\varphi^k, \beta_{\varphi})$
    $bx^{k+1} = bx^k + dx^{k+1} - x^{k+1}$ ▷ Bregman updates
    $by^{k+1} = by^k + dy^{k+1} - y^{k+1}$
    $bz^{k+1} = bz^k + dz^{k+1} - z^{k+1}$
    $bTE^{k+1} = bTE^k + dTE^{k+1} - TE^{k+1}$
    $b\varphi^{k+1} = b\varphi^k + d\varphi^{k+1} - \varphi^{k+1}$
    $f^{k+1} = f^k + f^0 - R\mathcal{F}^{-1}(u^{k+1})$ ▷ Data fidelity
  end while

Wavelet transform and Total Variation are common approaches to sparsify MR images. To select the best option, a comparison between these methods was performed. Reconstruction performances of Wavelet transform and TV were tested, with both performing similarly (Figure 9.1). Hence, TV was utilized as the transform to exploit sparsity in the spatial domains.

In the 5D CS optimization problem, the latter regularization terms exploit sparsity along the multi-echo and phase-cycle dimensions. A sparser domain is obtained by separately computing the 1D Fourier transform along the multi-echo and phase-cycle dimensions (Figure 3.1).

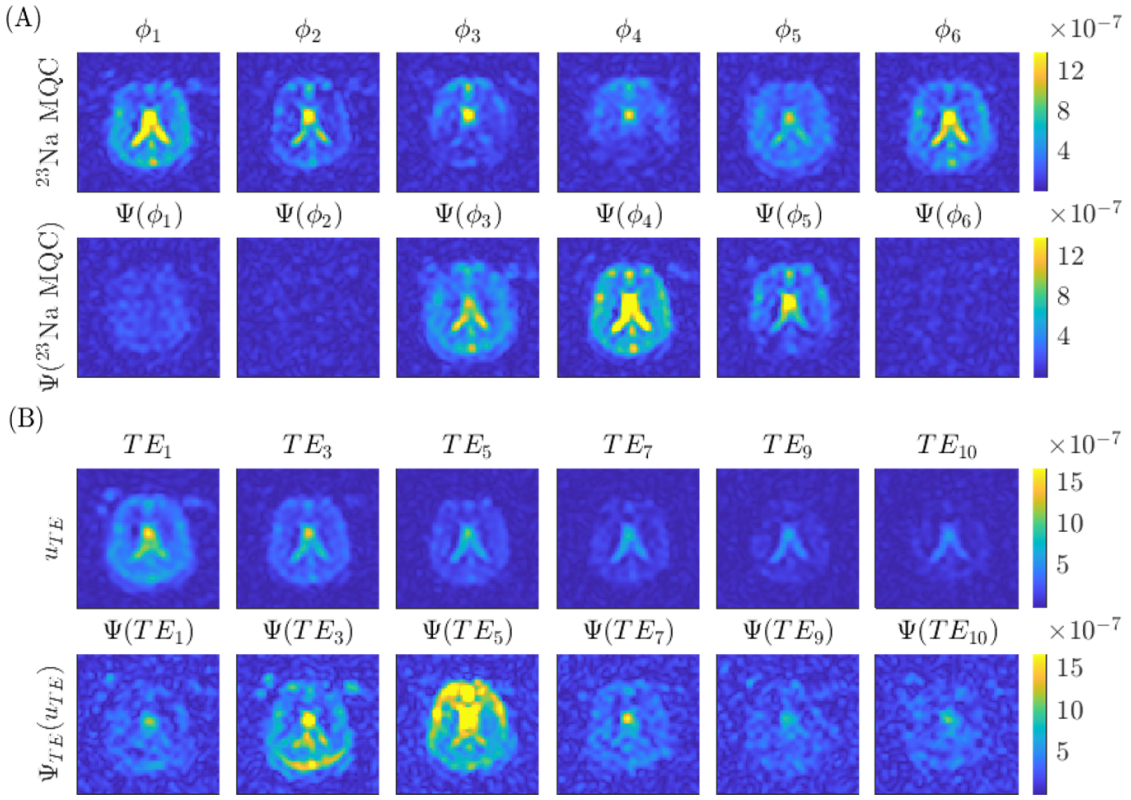

Figure 3.1: Demonstration of sparsity along the phase-cycling (A) and the multi-echo, TE (B) with u being the image. (A) Performing the Fourier transform along the phase-cycle dimension reveals the ^{23}Na MQC spectrum. The TQ image is depicted in image ϕ_1, and the SQ images are shown in images ϕ_3 and ϕ_5. It is demonstrated that the images at index 2 and 6 are pure noise, which shows that the image is sparser in the transformed domain. Additionally, the Fourier transform directly enables the regularization on the ^{23}Na MQC spectrum, further improving reconstruction performance by tuning the reconstruction towards either the SQ or TQ signal component. (B) Performing a Fourier transform along the multi-echo dimension reveals the dominant Fourier coefficients, depicted at the center (TE_5). Smaller Fourier coefficients represent noise and are shown in TE_1,TE_9 and TE_{10}. Conclusively, applying the Fourier transform along the echo time and the phase-cycle dimension results in sparser images, reducing the optimization problem's complexity. This sparsity is exploited within the additional regularization terms of the 5D CS model to find a better solution.

Based on empirical evaluation, spatial sparsity term weighting was set to $\lambda_p = 1$, with the optimal threshold being $\beta_p = 1.5$ and $\beta_p = 0.3$ for 3D and 5D CS, respectively. However, multi-dimensional sparsity is challenging to balance. Therefore, additional sparsity term weightings for 5D CS were determined by performing 144 CS reconstructions with weighting factors $\lambda_{TE} = 0.1...1.2$ and $\lambda_\phi = 1...2.1$ (12x12 combinations), enabling to find the optimal regularization parameters (Figure 9.2). Identically, optimal sparsity thresholds for the additional terms in the 5D CS model were empirically determined with $\beta_{TE} = 0.1...1.2$ and $\beta_\phi = 1.0...2.1$ (Figure 9.3). Based on the empirical results, optimal sparsity weightings were $\lambda_{TE} = 0.2$ and $\lambda_\phi = 1.9$ and optimal sparsity thresholds were $\beta_{TE} = 0.5$ and $\beta_\phi = 1.6$. Reconstruction times for numerical simulations were 550 seconds for 3D (50 iterations) and 227 seconds for 5D CS (300 iterations), and 3 T in vivo 313 seconds for 3D (100 iterations) and 55 seconds (250 iterations) for 5D CS.

3.1.3 Image processing

k-Space was zero-padded with the addition of 3D Hamming windowing. The first two echoes of CRISTINA phase data were used to compute a 3D B_0 map to obtain the signal off-resonances for the combination of the two-phase cycles (χ_0 and χ_{90}) according to Fleysher et al.[46]. Finally, applying a Fourier transform along the phase-cycle dimension revealed the SQ and TQ spectra. Reconstructed SQ and TQ images were fitted to the MQC bi-exponential model in Equation 3.8.

$$\begin{aligned} \textbf{TQ}: \; & A_{TQ}\left(e^{-\frac{TE}{T_{2s}^*}} - e^{-\frac{TE}{T_{2f}^*}}\right) e^{-\frac{\tau_1}{T_{2s}^*}} + DC_{TQ} \\ \textbf{SQ}: \; & \left(A_{SQ_1} e^{-\frac{TE+\tau_1+\tau_2}{T_{2s}^*}} + A_{SQ_2} e^{-\frac{TE+\tau_1+\tau_2}{T_{2f}^*}}\right) e^{-\frac{TE+\tau_1+\tau_2}{T_{2s*}}} + DC_{SQ} \end{aligned} \tag{3.8}$$

with A_{TQ}, A_{SQ_1}, A_{SQ_2} being triple- and single-quantum amplitude terms (slow and fast), $DC_{TQ,SQ}$ = DC offset accounting for noise, T_{2s}^*= T_2^* slow, T_{2f}^*= T_2^* fast, τ_1 = evolution time and τ_2 = mixing time (time between second and third RF pulse). The value of TQC at TE = 0 ms is 0 from theory and was added to the multi-echo data to enhance the fit. First, the voxel-wise multiparametric fit of TQ was performed, followed by the SQ fit with updated initial values, using non-linear least squares solver in Matlab (R2020a, Mathworks, Natick, MA, USA) leveraging parallel computing, providing T_{2s}^* and T_{2f}^* maps. The proposed workflow for the project is depicted in Figure 3.2.

3.1.4 Image analysis

Quantitative analysis of the phantom study was performed in a pre-determined Region of Interest (*ROI*) that was drawn over each tube on a single central slice, avoiding edges. ROI mean values served to compute SQ and TQ/SQ ratios for each tube. Linear regression was performed between SQ and prior known sodium concentration, TQ/SQ ratio, and known agar concentrations. Retrospectively undersampled numerical simulations and 3 T in vivo data, provided the fully sampled images, were analyzed using the Structural Similarity Index (*SSIM*)[78], the Root Mean Squared Error (*RMSE*), and the Signal-to-Noise Ratio (*SNR*). For numerical

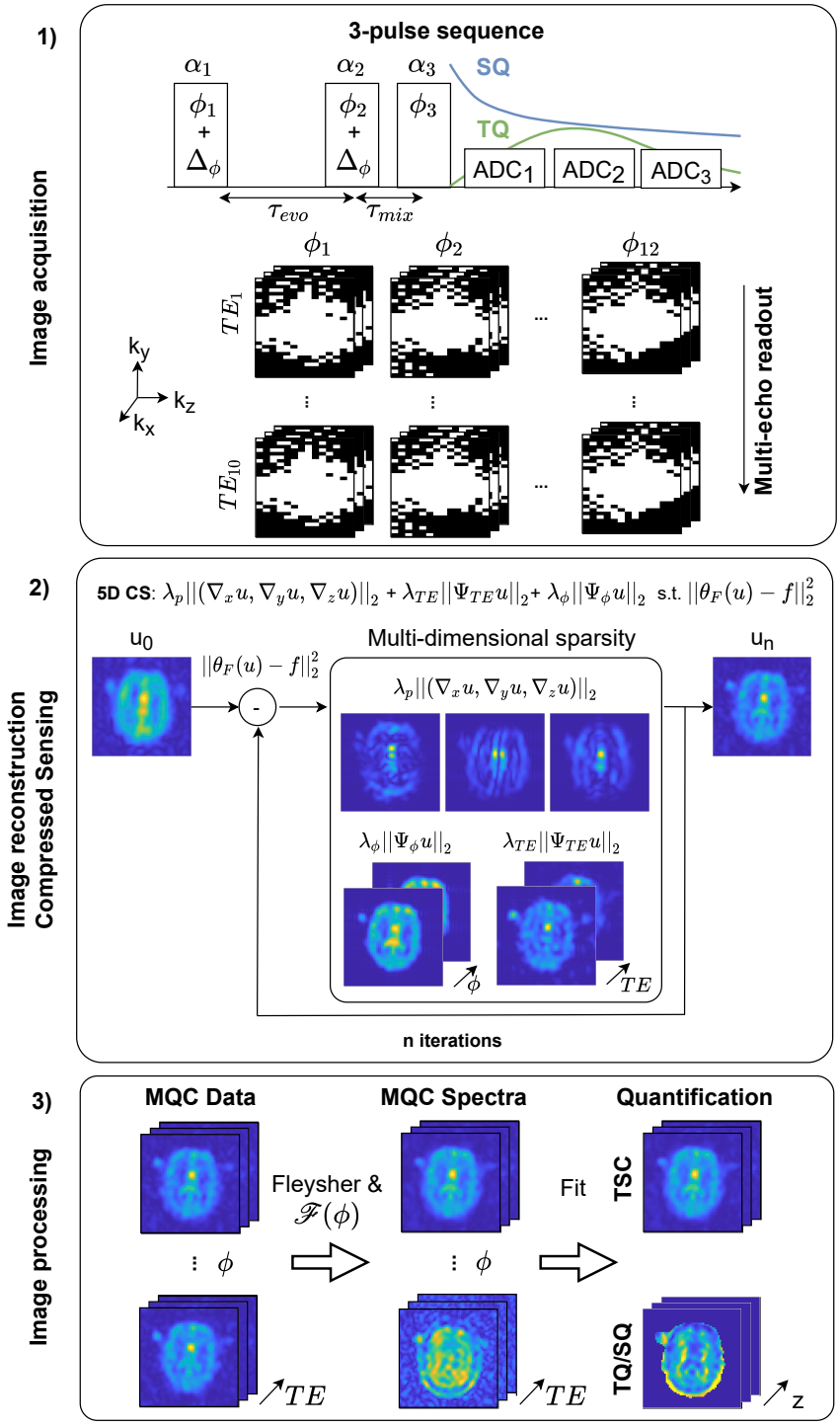

Figure 3.2: Workflow including variable density undersampling and CS reconstruction for accelerated ^{23}Na MQC MRI. (1) Image acquisition uses a 3-pulse RF phase-cycled 3D Cartesian multi-echo readout sequence, yielding a 5-dimensional signal structure involving 3D spatial, multi-echo, and phase-cycle dimensions. Undersampling is performed along ky and kz (phase-encoding) by alternating the patterns along the phase-cycle dimension, ϕ. (2) Undersampled high-multidimensional k-space data is reconstructed leveraging a conventional 3D or a custom-built 5D CS algorithm that exploits sparsity in all imaging dimensions. (3) The CS reconstructed data is processed using Fleysher combination and applying a Fourier transform along the phase cycle dimension revealed the ^{23}Na MQC spectra, e.g., SQ and TQ signal components. Finally, the reconstructed and processed images enable in vivo quantification of Tissue Sodium Concentration (TSC) and TQ/SQ ratio.

simulations, the metrics were evaluated over the whole image, whereas for the in vivo study, the metrics were computed for the head only.

$$\begin{aligned} \text{SSIM}(u, ref) &= l(u, ref) * c(u, ref) * s(u, ref) \\ \text{RMSE}(u, ref) &= \sqrt{\frac{1}{n}\sum_{i=1}^{n} |u_i - ref_i|^2} \\ \text{SNR}(u, ref) &= 20log_{10}\left(\frac{\overline{u}_{ROI}}{\sigma_{BG}}\right) \end{aligned} \tag{3.9}$$

with ref being the fully sampled reference image and SSIM(u, ref) the product of luminescence, $l(u, ref)$, contrast, $c(u, ref)$ and structure, $s(u, ref)$. $\overline{SI}$ represents the mean signal intensity in a specific region. u_{ROI} is the region of interest and u_{BG} is the noise obtained from the background, BG. Normalized intensity complex magnitude images were used to compute the SSIM and the RMSE. For 7 T prospectively undersampled data, the relative degree of focus was measured by computing the focus measure as the energy of the Laplacian[79] inside the region of interest.

3.2 Low-Rank reconstruction to advance ^{23}Na MQC MRI on clinical scanners

3.2.1 Modified CRISTINA sequence design

The three-pulse 3D Cartesian simultaneous Single and Triple Quantum ^{23}Na (*CRISTINA*)[15] sequence was modified to enable a one-line k-space sampling between the first and second RF pulse to capture a conventional sodium image. A Cartesian Double Half-Echo (DHE) time was chosen to achieve a very short echo time (TE). A fixed evolution time of 10 ms[74] and a bandwidth of 330 Hz/px were used for all experiments. Compared to the MQC signals, the DHE signal benefits from 1) a shorter echo time, 2) the contribution from the total sodium signal and 3) a faster signal accumulation throughout the multiple phase-cycling steps. As such, DHE and MQC shared the same FoV, but were decoupled for their matrix sizes and k-space undersampling patterns. DHE data achieved higher-resolution sodium images while MQC data targeted tissue sodium characterization, albeit with a lower spatial resolution. To accelerate MQC ^{23}Na acquisition and improve its spatial resolution, the MQC ^{23}Na data were undersampled with Cartesian 3D ky-kz variable-density random undersampling patterns following a Poisson distribution.[77] ^{23}Na MQC k-space data were undersampled first retrospectively and then prospectively. Undersampling patterns were varied for each phase-cycling step to enhance incoherence.

3.2.2 Numerical simulations

Double Half-Echo sodium images were simulated considering the two sodium signal compartments according to Equation 3.10 with T_1 and fast and slow T_2^* values (T_1/ T_{2s}^*/ T_{2f}^*, in ms): WM (34/ 3.4/ 18), GM (32/ 3.6/ 15) and CSF (55/ 51/ 51).[24, 72]

$$S_{^{23}Na} = 0.6 * e^{-\frac{TE}{T_{2f}^*}} + 0.4 * e^{\frac{-TE}{T_{2s}^*}} \tag{3.10}$$

Gradient imperfections were simulated by adding random phase offsets to the first row of each k-space half. Additionally, noise, η, with the power of $P = 0.0016$ defined as $P = mean(\eta^2)$, was added. Both k-space halves were simulated with an echo fraction of 50 (i.e., no k-space overlap), 52, 54 and 56% of k-space sampled (Figure 2) to obtain short echo times. Sampling an echo fraction below 60% of each k-space line has induced artifacts without the DHE low-rank framework.[65] Therefore, both k-space halves were jointly reconstructed with a low-rank coupling constraint with additionally added sparsity as detailed below. Following, two reconstructed k-space halves are obtained. However, combining both k-space halves does not benefit SNR since information was already shared during reconstruction.[65] Therefore, only the fully reconstructed forward k-space half was retained.

Multi-quantum coherences data was simulated with the same T1 and T2* values for each compartment. Simulation parameters included an evolution time set to $\tau_{evo} = 10$ ms, $TR = 200$ ms and field strength of $B_0 = 7$ T. ^{23}Na NMR dynamics were simulated using the irreducible spherical tensor operator formalism of Hancu et al.[73] and the evolution equations of van der Maarel[16] with the hard pulse approximation. Random Gaussian noise with varying power was then added to the data.

3.2.3 Data acquisition

Experimentally, prior to the MQC sodium scans, B_0 shimming was repeated with a ^{1}H-based vendor provided 3D shimming routine until convergence. A custom-built B_1^+ calibration sequence was employed to calibrate the three global 90° RF pulses. Modified CRISTINA acquisition parameters were summarized in Table 3.2. The DHE and MQC samplings shared the same FOV but were decoupled for their matrix sizes, and thus their resolutions.

Phantom:
Fully sampled (R[MQC]=1) images of a phantom consisting of 9 tubes (350 mL each) with varying agarose (0, 2 and 4%) and sodium (50, 100, 150-mM) concentrations were obtained. Prospectively undersampled (R[MQC]=3) MQC images of the same phantom were obtained conjointly with fully sampled DHE data.

in vivo:
The new CRISTINA sequence was tested on 6 volunteers (4 females, 2 males) undergoing ^{23}Na and ^{23}Na MQC MRI with 2 fully-sampled and 4 prospectively undersampled datasets. The study was approved by local ethical committee and volunteers were recruited after providing written informed consent according to the Declaration of Helsinki. Four reference vials were placed next to the head, with concentrations of agarose and ^{23}Na of: (4%; 100 mM), (4%; 50 mM), (2%; 100 mM) and (2%; 50 mM). Each examination included a prototype 3D anatomical ^{1}H MP2RAGE[76, 80] scan performed with a nominal resolution of 1x1x1mm^3 and accelerated 4-fold with Compressed Sensing to fit within 4 min.

3.2.4 Image reconstruction

3.2.4.1 Double Half-Echo

DHE images were reconstructed by a low-rank coupling constraint proposed by Bydder et al.[65, 66]. Manually inserting the data ('drop-in-place' method) into a single k-space matrix results in strong aliasing artifacts.[65] To compensate for artifacts arising from k-space undersampling, the framework identifies correlations along the rows of both k-space halves by enforcing low-rankness of the structured k-space matrix, as detailed in Figure 1 (1). Singular value filtering was used, leading to the following optimization problem that is regularized by an additional sparsity constraint:

$$\min_u ||\Phi_F(u) - f||^2 + \lambda_{WT}||\Psi_F(u)||_1 \;\; s.t.\; rank(A_H) = k', u = H^*(A_H) \tag{3.11}$$

with u being the target image, Φ_F representing the Fourier sampling operator, f the acquired data in k-space, λ_{WT} sparsity weighting parameter and Ψ_F the sparsifying transform performing an inverse Fourier transform followed by a Wavelet transform. H represents the structured matrix transform operator, with H^* being the inverse matrix transform operator and k' the prior rank of the data. DHE reconstruction was performed slice-wise, a kernel of size of 3x3 was used for simulations, phantom and in vivo data. Reconstruction was performed for a maximum of 80 iterations (70 seconds) and with up to 75% of Wavelet sparsity.

Table 3.2: Sequence parameters for numerical simulations, phantom, retro- and prospective in vivo study at 7 T. *Hard pulse approximation was used.

Parameter	**Image**	**Numerical Simulation**	**Phantom Retrospective**	**Phantom Prospective**	**In vivo Retrospective**	**In vivo Prospective**
FoV (mm^3)		181x217x181	240x240x210	240x240x210	225x225x210	240x240x210
Matrix size	DHE	54x54x45	50x50x50	50x50x50	68x68x14	40x40x40
	MQC	30x30x20	30x30x14	30x30x26	28x28x14	30x30x26
$TE_1/\Delta TE$ (ms)	DHE	0.5	0.6	0.6	0.7	0.5
	MQC	1.0/ 5.0	1.15/ 4.2	1.15/ 4.2	1.20/ 4.2	1.15/ 4.15
TR (ms)		200	173	173	200	212
Pulse length (ms)		0*	0.8	0.8	0.8	0.8
Averages	DHE	1	4	2	4	2
	MQC	1	4	4	4	4
Undersampling R	DHE	1	1	1	1	1
	MQC	1	1	3	1	3
TA (min)		-	2x29	2x19	2x31	2x23

3.2.4.2 Multi-Quantum Coherences

Simultaneous autocalibrating and k-space estimation (SAKE[64]) is a low-rank reconstruction framework that builds a highly structured matrix to exploit coherent information across various k-space subspaces, summarized in Figure 1 (2). It has already been mentioned by Shin et al.[64] and Holme et al.[81] that a major drawback of SAKE is it is computationally expensive because, for each iteration, a new SVD needs to be computed. We address this shortcoming by setting a prior rank for the data matrix only to calculate a subset of singular vectors[82] (available from [1]) reducing reconstruction time as suggested by Shin et al.[64]. ^{23}Na MQC data were jointly reconstructed by 5D Compressed Sensing (5D CS[28]) or by SAKE, which solves the following optimization problem

$$\min_{u} ||\Phi_F(D(u)) - f||^2 \;\; s.t.\; u = H^*(A_H), rank(A_H) = k' \tag{3.12}$$

with u being the image one wants to reconstruct, Φ_F being the Fourier sampling operator relating reconstructed with acquired data, f, D represents the matrix operator to reshape the 5D signal input into a structured 4D matrix with alternating echo and phase-cycle snapshots. k' is a prior estimate of $rank(A_H)$ of matrix A, enforcing subspace SVD. H^* being the inverse structured matrix operator, see[64] and the l_2 norm enforces data consistency. A kernel size of 3x3x2 for simulations, phantom and in vivo data was used with a maximum of 100 iterations (reconstruction time <2 min). The proposed workflow for the project is depicted in Figure 3.3.

Our experiments revealed that SAKE highly depends on optimal shrinkage thresholds and the appropriate selection of ranks to retain a sufficient amount of singular values that express most of the data variances. This is especially crucial for ^{23}Na MQC MRI since SQ and TQ signal components are jointly reconstructed by exploiting coherent information of the superimposed ^{23}Na MQC signal. Our experiments showed that a shrinkage value that was too high led to signal leakage of SQ into the TQ component, whereas a shrinkage value that was too low produced aliased images (Figure 9.7).

3.2.5 Image processing

After reconstruction of the two undersampled ^{23}Na MQC data sets (χ_0 and χ_{90}), they were combined according to the method of Fleysher et al.[46]. Finally, applying a Fourier Transform along the phase-cycle dimension revealed the SQ and TQ spectra. Reconstructed SQ and TQ images were fitted to the MQC bi-exponential model.

$$\begin{aligned} \mathbf{TQ}: \;& A_{TQ}\left(e^{-\frac{TE}{T_{2s}^*}} - e^{-\frac{TE}{T_{2f}^*}}\right) e^{-\frac{\tau_1}{T_{2s}^*}} + DC_{TQ} \\ \mathbf{SQ}: \;& \left(A_{SQ_1} e^{-\frac{TE+\tau_1+\tau_2}{T_{2s}^*}} + A_{SQ_2} e^{-\frac{TE+\tau_1+\tau_2}{T_{2f}^*}}\right) e^{-\frac{TE+\tau_1+\tau_2}{T_{2s*}}} + DC_{SQ} \end{aligned} \tag{3.13}$$

with A_{TQ}, A_{SQ_1}, A_{SQ_2} being triple- and single-quantum amplitude terms (slow and fast), $DC_{TQ,SQ}$ = DC offset accounting for noise, T_{2s}^*= T_2^* slow, T_{2f}^*= T_2^* fast, τ_1 = evolution time and τ_2 = mixing time (time between second and third RF pulse).

[1] *https://github.com/cpmusco/bksvd*

The value of the TQ signal at TE = 0 ms is 0 from theory and was added to the multi-echo data to enhance the fit. First, the voxel-wise multi-parametric fit of TQ was performed, followed by the SQ fit with updated initial values, using a non-linear least squares solver in Matlab (R2020a, Mathworks, Natick, MA, USA) leveraging parallel computing, providing T_{2s}^* and T_{2f}^* maps.

3.2.6 Image analysis

For the phantom study, quantitative analysis was performed in a pre-determined region of interest (ROI) drawn over each tube on a single central slice, avoiding edges. Linear regression was computed between the SQ signal, prior known sodium concentrations, and the TQ/SQ ratio and prior known agar concentrations. For the numerical simulations and in vivo data, provided the fully sampled images, structural similarity index (SSIM)[78], root mean squared error (RMSE) and signal-to-noise ratio (SNR) were computed for each undersampling experiment.

$$\begin{aligned} \text{SSIM}(u, ref) &= l(u, ref) * c(u, ref) * s(u, ref) \\ \text{RMSE}(u, ref) &= \sqrt{\frac{1}{n}\sum_{i=1}^{n} |u_i - ref_i|^2} \\ \text{SNR}(u, ref) &= 20 log_{10}\left(\frac{\overline{u}_{ROI}}{\sigma_{BG}}\right) \end{aligned} \tag{3.14}$$

with ref being the fully sampled reference image and SSIM(x, y) the product of luminescence, $l(x, y)$, contrast, $c(x, y)$ and structure, $s(x, y)$. $\overline{SI}$ represents the mean signal intensity in a specific region. u_{ROI} is the region of interest and u_{BG} is the noise obtained from the background, BG. Normalized intensity complex magnitude images were used to compute the SSIM and the RMSE. MP2RAGE images were segmented with SPM12 [83] into WM, GM, and CSF masks. TSC estimates were obtained using linear interpolation based on reference vials placed next to the volunteer's head and/ or the CSF [84]. In addition, TSC and TQ/SQ ratios were compared employing a two-sided t-test with $\alpha = 0.05$. The DHE images were reconstructed by manually inserting both k-space halves into a matrix ('drop-in place') or leveraging the low-rank coupling constraint. To evaluate the DHE reconstruction, the relative degree of focus (FM) was measured by computing the focus measure as the energy of the Laplacian [79] inside the region of interest.

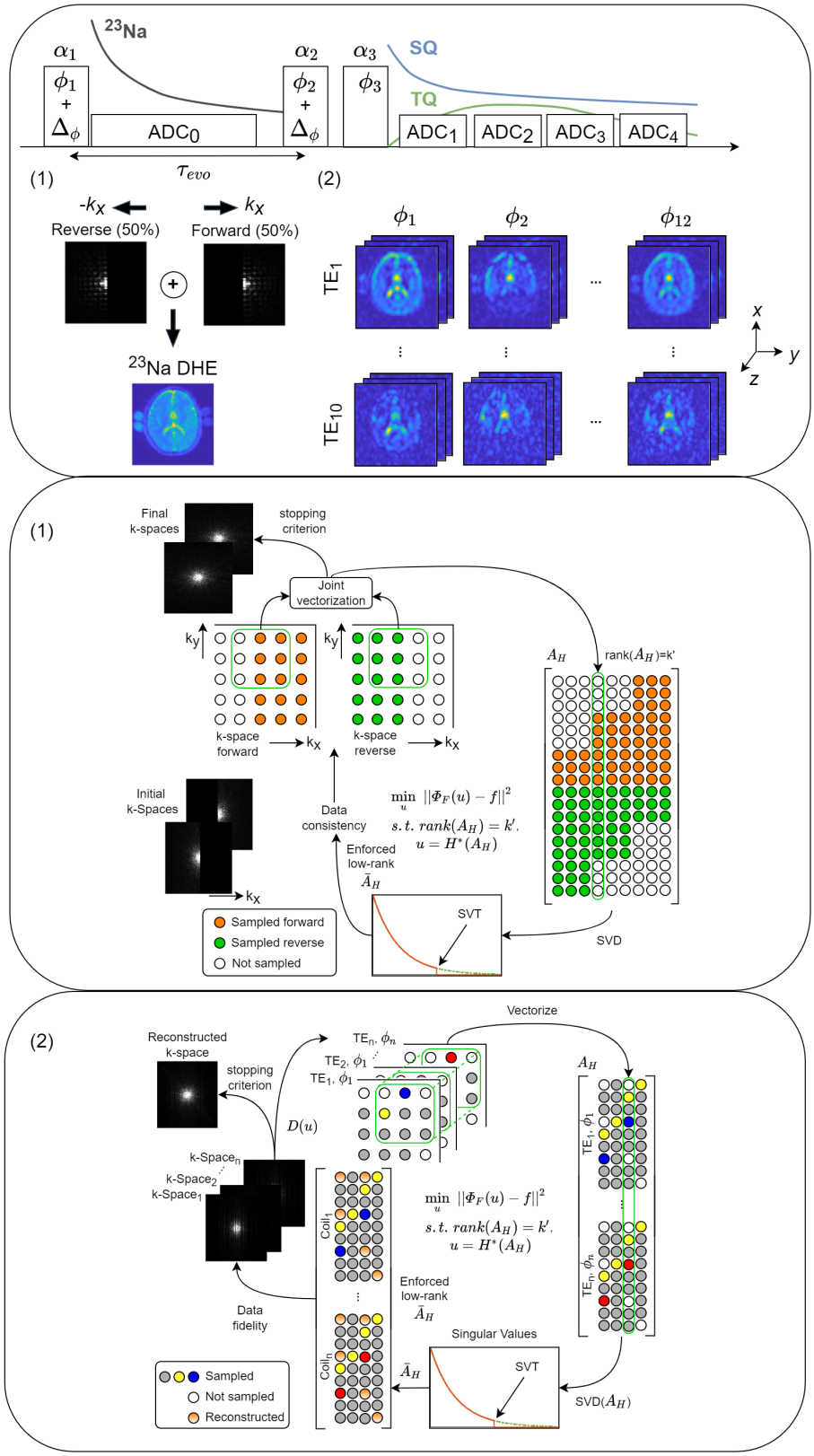

Figure 3.3: Proposed workflow to simultaneously acquire ^{23}Na by leveraging the DHE technique (1) and undersampled ^{23}Na MQC MRI by utilizing the SAKE framework. (1) Forward and reverse k-space halves are reconstructed by a low-rank coupling constraint exploiting coherences along the k-space rows. (2) Undersampled Multi-Quantum Coherences MRI is reconstructed using the SAKE framework. Both image reconstruction frameworks utilize structured 2D matrices to exploit coherences across the ^{23}Na and multi-dimensional ^{23}Na MQC k-spaces.

4. Results

Sparse and low-rank reconstructions to advance ^{23}Na MQC MRI on clinical scanners were investigated and the results are given in this chapter. Section 4.1 shows the results for Compressed Sensing-based reconstructions at 3 and 7 T and Section 4.2 demonstrates the results for low-rank reconstruction for ^{23}Na and ^{23}Na MQC MRI at 7 T. Parts of this chapter have been published in Licht et al.[28] and Licht et al.[70] by Wiley.

4.1 Multi-Dimensional Compressed Sensing reconstruction to advance ^{23}Na MQC MRI on clinical scanners

4.1.1 Numerical simulations

The realistic numerical simulation of a CRISTINA acquisition from the 3-compartment 3D brain enabled the anticipation of the SQ and TQ noise levels with and without k-space undersampling (Figure 4.1). Alternating the sampling masks along the phase-cycle enabled to cover k-space by 82%, 76%, 62%, 50%, 40%, and 24% for R=2 to 7, respectively. Indeed, 3D and 5D Compressed Sensing improved image reconstruction compared to zero-filling. Discrepancies between 3D and 5D CS reconstructions were already observed at an undersampling factor of R=3. Mean TSC values in WM, GM and CSF were found to be on par: 43 ± 14 mM, 45 ± 21 mM, 132 ± 31 mM for fully sampled, 43 ± 16 mM, 44 ± 20 mM, 118 ± 45 mM for 3D CS and 43 ± 15 mM, 45 ± 22 mM, 131 ± 32 mM for 5D CS reconstructions, respectively. Similarly, mean TQ/SQ ratio values in WM, GM, and CSF were 0.17 ± 0.05, 0.14 ± 0.06, 0.08 ± 0.06 for fully sampled, 0.16 ± 0.05, 0.14 ± 0.06, 0.10 ± 0.07 for 3D CS and 0.17 ± 0.05 and 0.14 ± 0.06, 0.08 ± 0.06 for 5D CS reconstructions, respectively.

All metrics, SSIM, RMSE, and SNR, confirmed 5D CS outperformed 3D CS both along the echo time dimension for R=3 (Figure 4.1, B) or at various undersampling rates (Figure 4.2, B). Mean values and standard deviations were reported in Table 4.1, A. 5D CS proved to achieve low errors (RMSE), especially at R=2 and R=3. Especially for the TQ reconstruction at R=3, 5D CS improved SSIM by 47% and reduced RMSE by 2.5-fold. The SNR evolution over time revealed characteristic SQ and TQ signal evolutions for both CS models. 5D CS consistently provided improved reconstruction results across all undersampling factors, especially for higher undersampling factors (R>3).

Reconstruction from 5D CS also proved to be more resilient to increased noise levels than 3D CS (Figure 4.2, A). The SSIM, RMSE, SNR mean, and standard deviation were given in Table 9.1. Notably, errors for R=3 TQ images increased almost linearly with noise power for 5D CS. Although the TQ signal had a low SNR, 5D CS recovered this signal component despite increasing noise levels. Especially remarkable is the consistently improved SSIM and SNR for the TQ signal reconstructed by 5D CS.

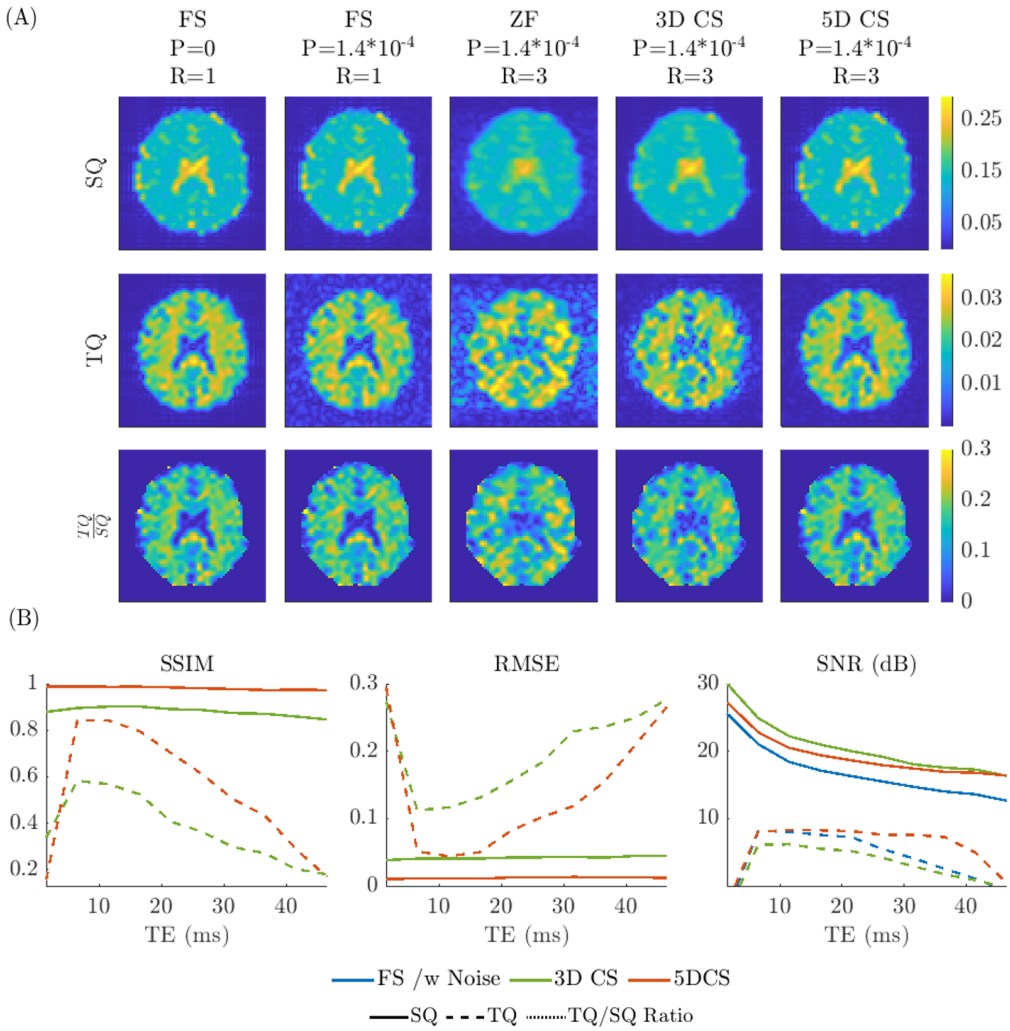

Figure 4.1: (A) Simulated SQ, TQ, and TQ/SQ brain data with a nominal resolution of 7x7x10mm^3 fully sampled and undersampled with R=3. The noise was added (noise power P=1.4*10^{-4}), and undersampled data were reconstructed with zero-filling, 3D, and 5D CS. (B) Quantitative evaluation of reconstruction performance for R=3 via SSIM, RMSE, and SNR for simulated SQ and TQ brain data depicted in (A).

4.1.2 Phantom study

Image reconstruction from 3-fold retrospectively undersampled phantom data acquired at 3T confirmed that 5D CS outperformed 3D CS. (Figure 4.3): undersampling artifacts were reduced, especially for vials 1-3, and image sharpness was increased. Linear regression (Figure 4, C) was confirmed between the SQ signal and the known NaCl concentration and between the TQ/SQ ratio and the known agar concentration in each vial. The TSC was well preserved in both reconstructions. Still, the 3D CS TQ/SQ ratio in vials 1 to 3 deviated more from the fully sampled data, indicated by the arrow in the linear regression plot. Fully sampled phantom data exhibited an SNR of 21.93 dB and 8.26 dB, 3D CS of 27.56 dB and 6.18 dB, and 5D CS of 28.44 dB and 13.65 dB for SQ and TQ, respectively. Results of fit parameter maps can be appreciated in supporting information (Figure 9.4), with

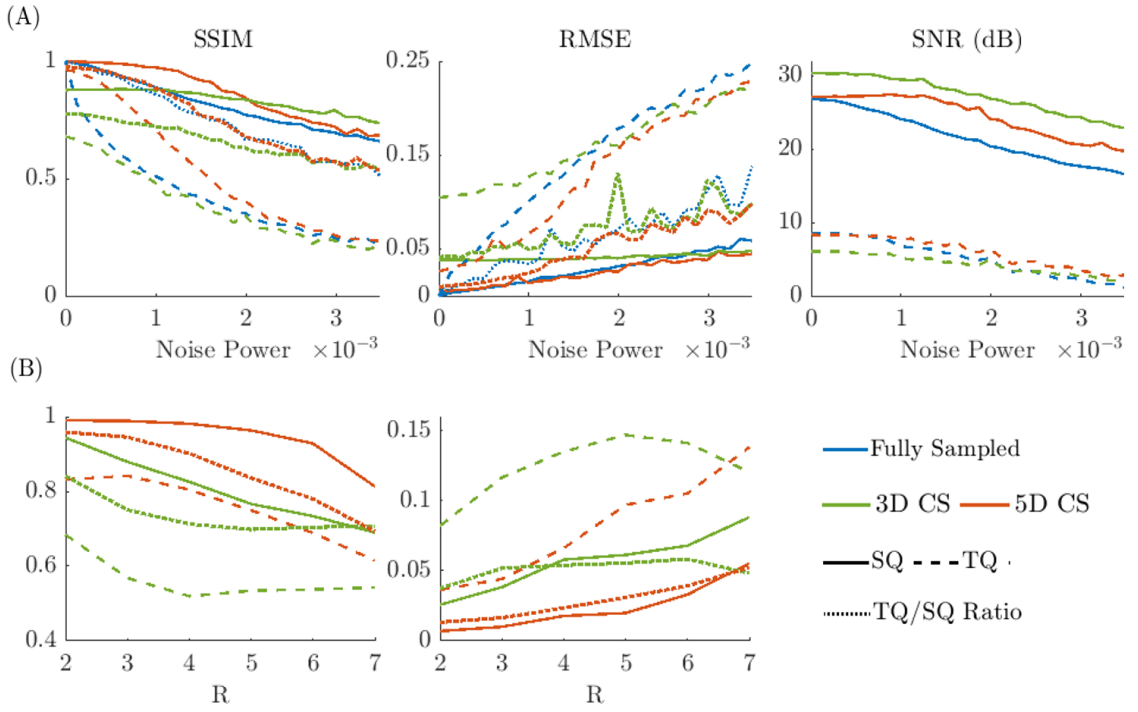

Figure 4.2: Quantitative evaluation of reconstruction performance via SSIM, RMSE, and SNR for simulated SQ and TQ brain data depicted in Figure 4.1. (A) Additive noise performance evaluation regarding SSIM, RMSE, and SNR for R=3, with 3D and 5D CS reconstructed and increasing noise levels. (B) Reconstruction evaluation for different acceleration factors, R, for 3D and 5D CS models obtained with the same noise power as used in Figure 4.1.

a summary of the T_2^* slow and fast components given in Table 9.2. There was no significant difference between fully sampled and reconstructed T_2^* values for both 3D and 5D CS.

4.1.3 3 T in vivo study

It was found that exploiting sparsity along the multi-echo and phase-cycle dimensions improved reconstruction results compared to only exploiting sparsity along either one of the dimensions (Figure 9.5, Table 9.3). Results from retrospectively undersampled in vivo ^{23}Na MQC brain data acquired at 3 T confirmed the superiority of 5D CS over 3D CS (Figure 4.4). Images reconstructed by 3D CS exhibited severe blurring, notably the SQ image and aliasing artifacts, as seen in the TQ image. In contrast, most features observed in fully sampled images were preserved in images reconstructed by 5D CS. The TSC and TQ/SQ ratio quantification in the WM, GM, and CSF compartments demonstrated minimal discrepancies in region-wise quantification. TSC for fully sampled data was 49 ± 66mM 36 ± 41mM and 141 ± 123mM, for 3D CS 54 ± 69mM 32 ± 42mM and 142 ± 128mM and for 5D CS 51 ± 67mM 34 ± 38mM and 141 ± 126mM, for WM, GM and CSF, respectively. TQ/SQ ratio was found to be 0.16 ± 0.06, 0.13 ± 0.04 and 0.11 ± 0.05 for fully sampled, 0.15 ± 0.04, 0.14 ± 0.03 and 0.12 ± 0.04 for 3D CS, and 0.16 ± 0.06, 0.13 ± 0.04 and 0.11 ± 0.04 for 5D CS. At an undersampling factor of R=2, 3D and 5D CS performed similarly (Figure 4.4, A). However, at R=3, TQ reconstructed

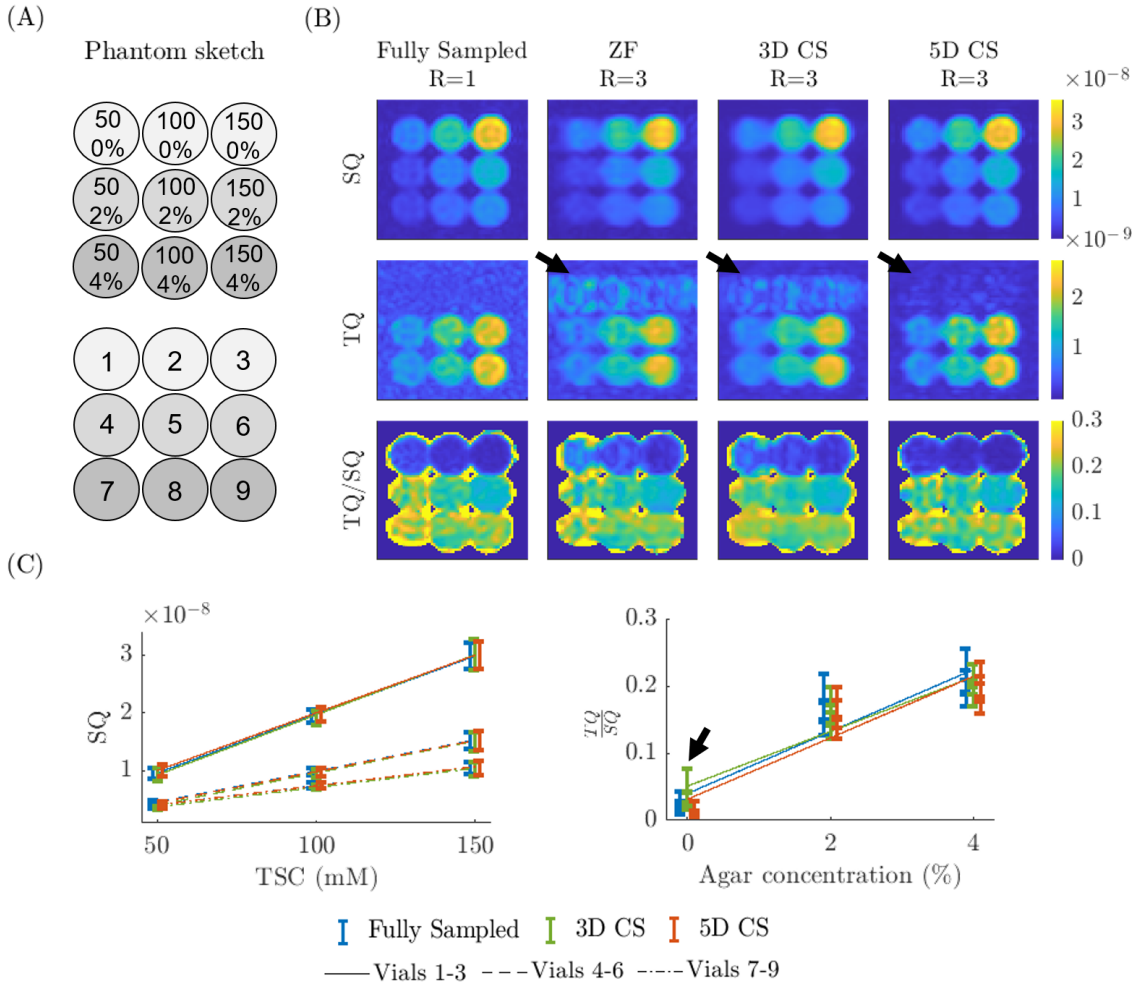

Figure 4.3: Phantom study: (A) Phantom design consisting of 9 different vials (350-mL each) with different NaCl (50, 100, 150 mM) and varying agar concentrations (0, 2 and 4%). Phantom vial enumeration for subsequent reconstruction performance evaluation within each vial. (B) SQ, TQ, and TQ/SQ ratio comparison of fully sampled, 3D, and 5D CS reconstruction for a retrospective undersampling factor of R=3. SQ and TQ images were fitted with corresponding equations in Equation 3.8, respectively. Note the residual undersampling artifacts in the 3D CS reconstruction. (C) Shows the linear regression for the mean SQ signal intensity versus prior known TSC in each vial for the fitted data. Data exhibited linear relationships of R^2=0.99* for fully sampled, 3D, and 5D CS reconstructed images. Additionally, linear regression was performed on each vial's mean TQ/SQ signal intensity versus known agar concentration. For the fitted data, linear relationship were found to be R^2=0.84*, R^2=0.87*, R^2=0.86* for fully sampled, 3D and 5D CS, respectively. With R^2 being the adjusted goodness-of-fit and * representing statistical significance ($p<0.05$). Computed T_2^* values can be found in supporting information Table 9.3 and Figure 9.4.

with 3D CS exhibited residual undersampling artifacts, which were suppressed in the 5D CS reconstruction. SSIM, RMSE, and SNR evaluated for R=3 along the echo time showed consistently improved performance for the 5D CS model (Figure 4.4,

B). With increasing undersampling factor, expected blurring and image degradation were observed. Nevertheless, 5D CS systematically provided higher quality SQ images than 3D CS, even for high acceleration factors. Quantitative metrics were given in Table 4.1, B.

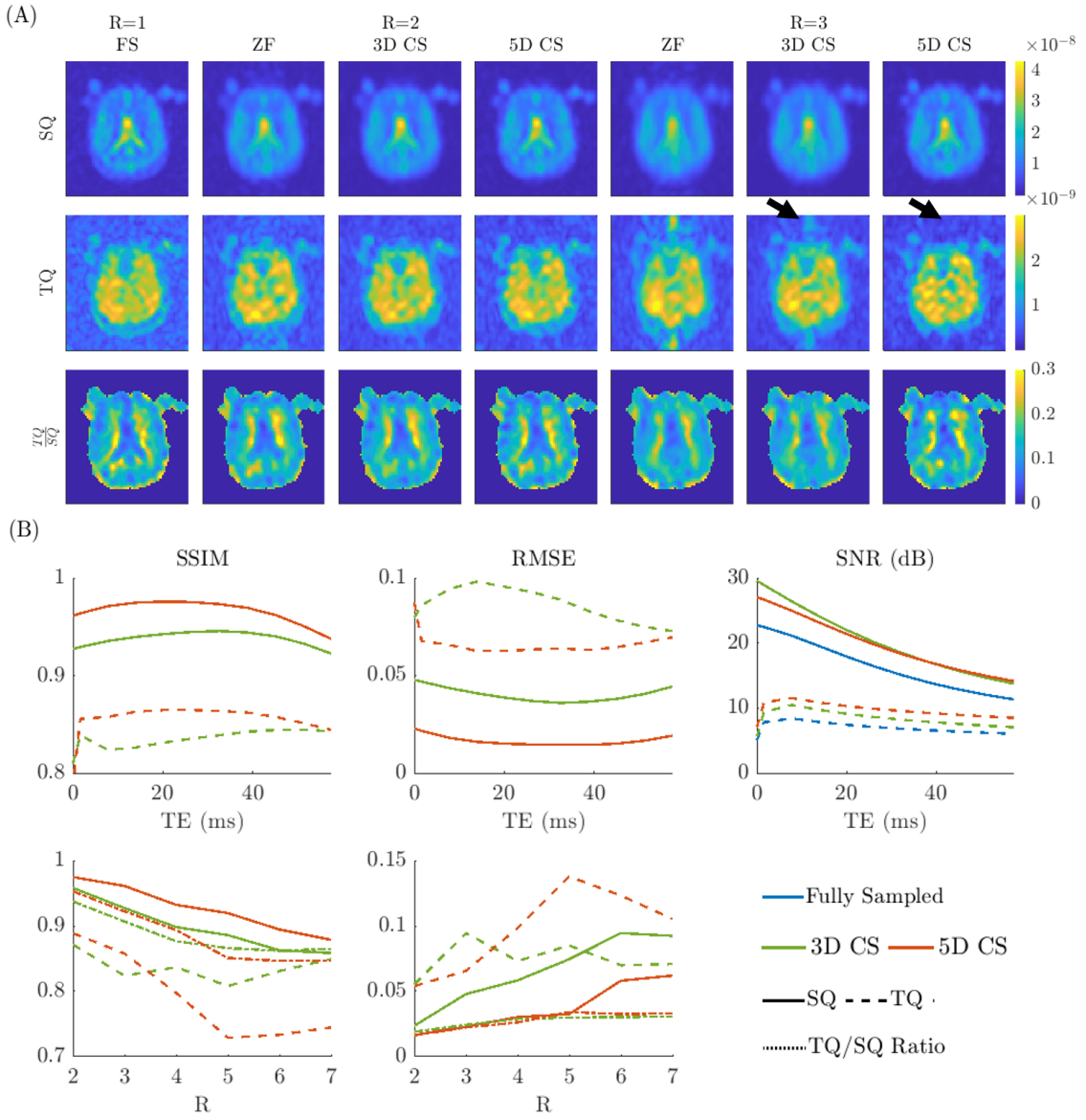

Figure 4.4: (A) Visual representation of reconstruction performance for different undersampling factors, R=2 to 3, for one volunteer acquired at 3 T. (B) In vivo SNR, RMSE, and SSIM evaluation over all echoes and for one echo over all undersampling factors for retrospectively undersampled in vivo brain 3 T data are shown.

Figure 4.5 shows three slices of a second volunteer's T_1w ^{1}H and ^{23}Na MQC brain data acquired at 3 T and retrospectively undersampled by a factor R=3. Over the multiple slices, SQ images reconstructed with the proposed 5D CS model exhibited less blurring and finer imaging details. Similarly, joint CS reconstruction reduced undersampling-related aliasing artifacts. Additionally, 5D CS provided fewer erroneous TQ/SQ ratio maps, as indicated by the arrow, and improved visual delineation

between WM, GM, and CSF. Pushing acceleration further by reducing the number of averages, 5D CS still proved to reconstruct reliable SQ and TQ images within an acquisition time of less than 5 minutes (Figure 9.6).

4.1.4 7 T in vivo study

Leveraging a conservative two-fold prospective undersampling, the results of the 7 T in vivo study provided unprecedented resolution for MQC ^{23}Na images (Figure 7). Zero-filling yielded blurry SQ and aliased TQ images. 5D CS provided increased SQ image sharpness, which was also confirmed by the focus measure metric: ZF $= 2.19 * 10^{-8}$, 3D CS $= 2.28 * 10^{-8}$, 5D CS $= 2.50 * 10^{-8}$. Additionally, 5D CS reconstructed images provided increased SNR: ZF = 13.10/ 4.56 dB, 3D CS = 13.34/ 6.87 dB, 5D CS = 17.62/ 11.88 dB for SQ and TQ, respectively. The SQ images showed high signal intensity in the CSF compartment, whereas the TQ signal mostly originated from the brain parenchyma. Combining these two images, the TQ/SQ ratio for 3D and 5D CS was on par with 5D CS images, showing an improved delineation between WM, GM, and CSF. It can be appreciated that WM exhibited the highest TQ/SQ ratio 0.21 ± 0.11 and 0.19 ± 0.11, GM intermediate 0.11 ± 0.06 and 0.10 ± 0.06 and CSF the lowest 0.07 ± 0.04 and 0.07 ± 0.05 for 3D and 5D CS, respectively. The improved 3D spatial resolution can also be appreciated in the sagittal and coronal views, where the 5D CS reconstruction also enhances the delineation between the respective compartments.

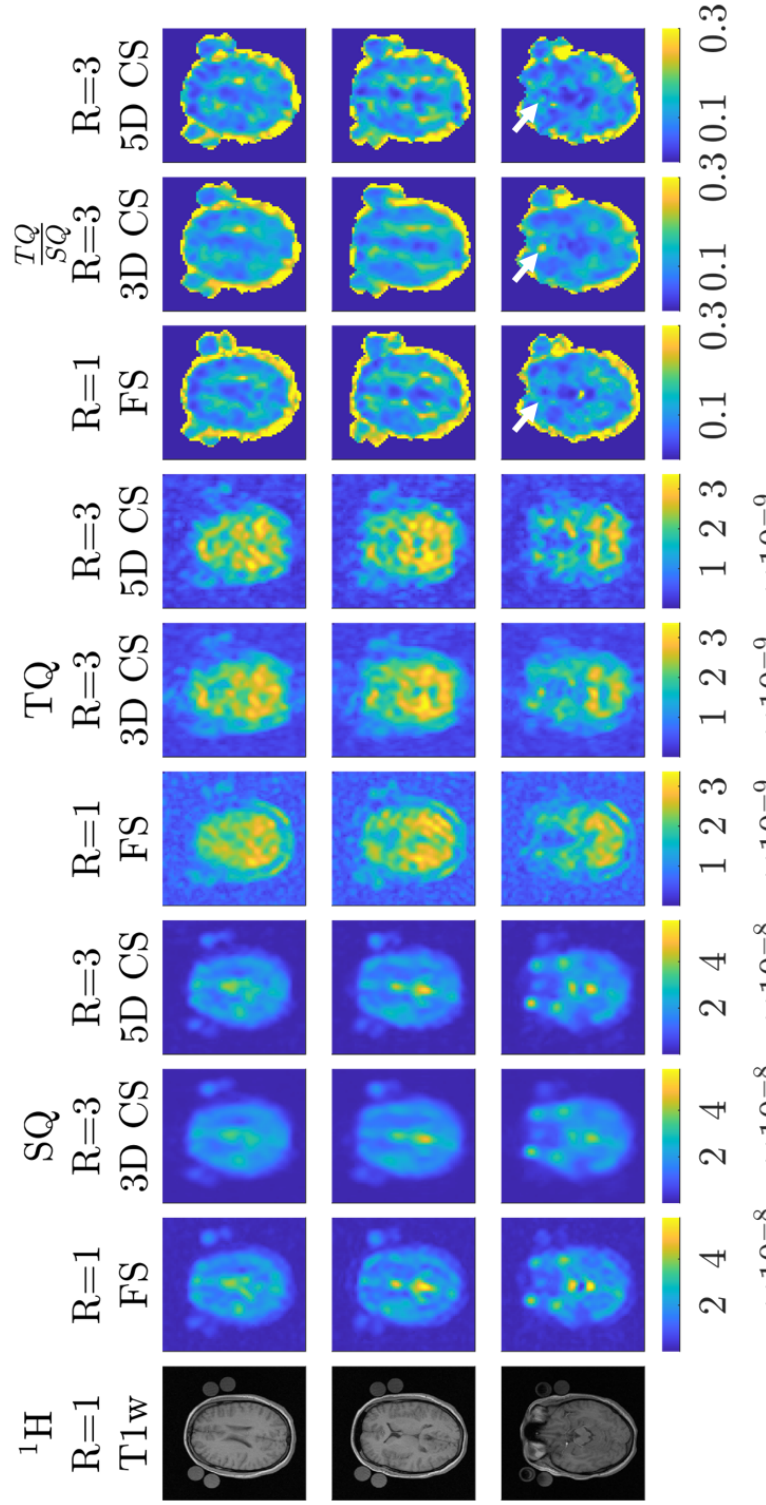

Figure 4.5: Retrospectively 3-fold undersampled 3 T in vivo brain data reconstructed with 3D and 5D CS shown for multiple slices of one volunteer. Indeed, 5D CS provided enhanced detail in TQ/SQ ratio maps with clear delineation between WM, GM, and CSF.

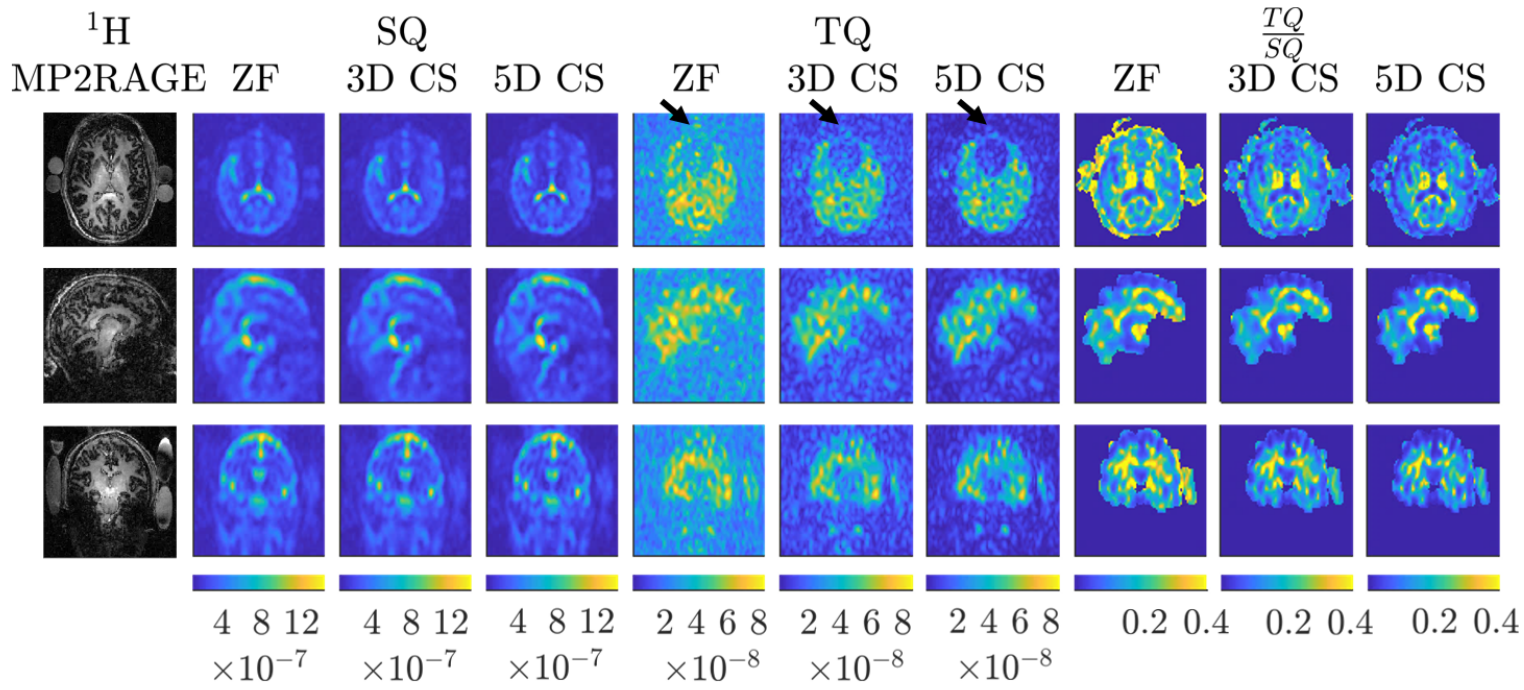

Figure 4.6: Prospectively 2-fold undersampled 7 T in vivo brain data reconstructed with zero-filling, 3D and 5D CS shown for transversal, sagittal and coronal plane with the corresponding anatomical ^{1}H reference images.

Table 4.1: Mean and standard deviations for SSIM, RMSE, and SNR of reconstructed SQ and TQ for (A) in silico and (B) in vivo. $CS_{R=3}$ represents the metrics for R=3 for SQ at TE=1 or TQ at TE=3. CS_R represents the metric evaluation averaged over all undersampling factors, R=2 to 7. Table (A) corresponds to the numerical simulation (fully sampled: SNR SQ = 25.56 dB, TQ = 7.94 dB) and (B) to the in vivo study performed at 3 T (fully sampled: SNR SQ = 22.73 dB, TQ = 8.40 dB).

	Model	**Signal**	**SSIM**	**RMSE**	**SNR (dB)**
(A)		SQ	0.88	0.038	30.01
	3D $CS_{R=3}$	TQ	0.57	0.117	6.19
		TQ/SQ	0.75	0.052	–
		SQ	0.99	0.010	27.27
	5D $CS_{R=3}$	TQ	0.84	0.044	8.28
		TQ/SQ	0.95	0.017	–
		SQ	0.81 ± 0.10	0.057 ± 0.022	–
	3D CS_R	TQ	0.56 ± 0.06	0.124 ± 0.024	–
		TQ/SQ	0.74 ± 0.05	0.051 ± 0.008	–
		SQ	0.94 ± 0.07	0.024 ± 0.018	–
	5D CS_R	TQ	0.76 ± 0.09	0.081 ± 0.040	–
		TQ/SQ	0.85 ± 0.10	0.029 ± 0.015	–
(B)		SQ	0.93	0.048	29.59
	3D $CS_{R=3}$	TQ	0.82	0.094	10.46
		TQ/SQ	0.91	0.024	–
		SQ	0.96	0.023	277
	5D $CS_{R=3}$	TQ	0.86	0.066	11.54
		TQ/SQ	0.92	0.022	–
		SQ	0.90 ± 0.04	0.065 ± 0.027	–
	3D CS_R	TQ	0.84 ± 0.02	0.075 ± 0.014	–
		TQ/SQ	0.89 ± 0.03	0.027 ± 0.005	–
		SQ	0.93 ± 0.04	0.037 ± 0.019	–
	5D CS_R	TQ	0.79 ± 0.07	0.097 ± 0.032	–
		TQ/SQ	0.89 ± 0.05	0.027 ± 0.007	–

4.2 Low-Rank reconstruction to advance ^{23}Na MQC MRI on clinical scanners

4.2.1 Numerical simulations

DHE:
The quantitative analysis revealed an optimal echo fraction of around 52% (Figure 4.7). Below 52%, blurred images with lower SSIM, increased RMSE, and reduced SNR were observed. At an echo fraction of 52%, corresponding to a forward and reverse k-space halves echo overlap of 4%, the reconstructed DHE image revealed an SSIM of 0.90, an RMSE of 0.029, and an increased SNR of 14% when compared to the fully sampled input image. Increased oversampling (>4%) did not show an increase in quantitative metrics such as SSIM but further prolonged TE. Thus, all DHE employed a 52% echo fraction. TSC estimations for fully sampled and DHE reconstructed sodium images were found to be on par with 59 ± 6.55/ 61 ± 8.09, 64 ± 14.00/ 64 ± 13.54 and 90 ± 28.09/ 90 ± 29.54 for WM, GM and CSF respectively.

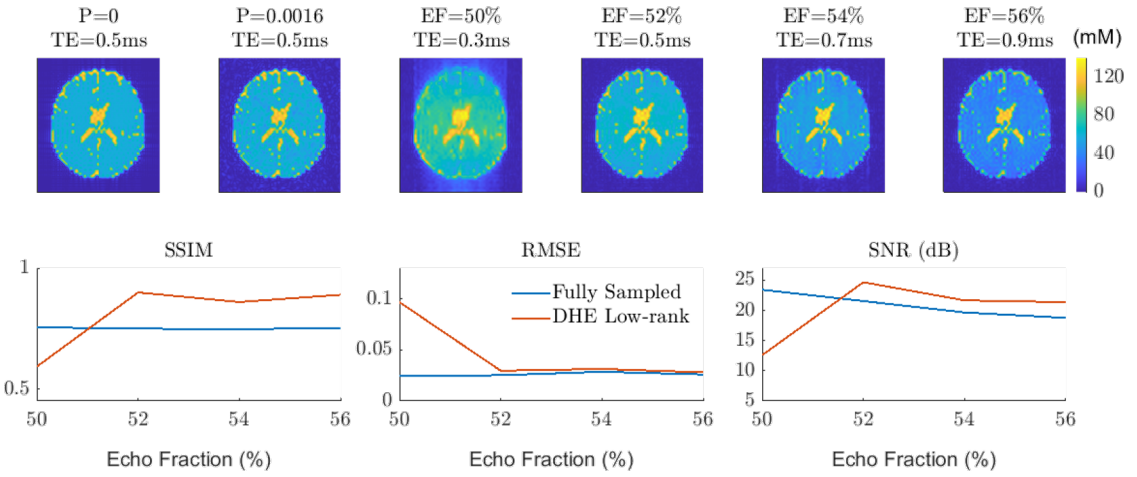

Figure 4.7: Numerical simulations of varying echo fractions and corresponding echo times. Quantification of low-rank reconstruction performance revealed an optimal echo fraction of around 52%.

MQC:
^{23}Na MQC MRI was confirmed intrinsically redundant, and most of the variance in the data was expressed by retaining 10% of the most significant singular values (Figure 9.7, A). By combining χ_0 and χ_{90} to be reconstructed simultaneously, data redundancy could be further enhanced, thus strengthening reconstruction performance when compared to reconstructing χ_0 and χ_{90} separately (Figure 9.7, B, Table 9.4). At an R[MQC]=3 undersampling factor, 5D CS and SAKE provided aliasing-free images (Figure 4.8, A). SQ images revealed their highest signal intensity in the CSF compartment, whereas the TQ signal was highest in WM. TQ/SQ ratio was found to be 0.16 ± 0.06/ 0.13 ± 0.06/ 0.07 ± 0.05 for fully sampled, 0.16 ± 0.06/ 0.13 ± 0.06/ 0.07 ± 0.05 for 5D CS and 0.15 ± 0.05/ 0.13 ± 0.06/ 0.07 ± 0.05 for SAKE, in WM, GM and CSF, respectively. No statistical significance was found for the TQ/SQ ratio between reconstruction models. However, improved SQ metrics were provided by 5D CS, whereas SAKE yielded enhanced metrics for TQ reconstruction (Figure 4.8,

B and Table 4.2, A). Interestingly, SAKE reconstructed TQ snapshots along TE exhibited greatly improved SSIM and RMSE compared to 5D CS, especially for later echoes (TE_5=20 ms to TE_{10}=46 ms). SAKE improved SSIM by 50% and reduced RMSE by 2-fold. Interestingly, for R[MQC]=3 and small noise levels, 5D CS provided improved image reconstruction for SQ, TQ, and the ratio maps. However, with increasing noise levels (P>1x10^{-3}), SAKE demonstrated consistently improved TQ reconstruction (Figure 4.9, A), showing up to 2-fold improvement in SSIM and RMSE. SAKE proved a more reliable reconstruction concerning SSIM, RMSE, and SNR for SQ, TQ, and TQ/SQ ratio maps, particularly at higher noise levels.

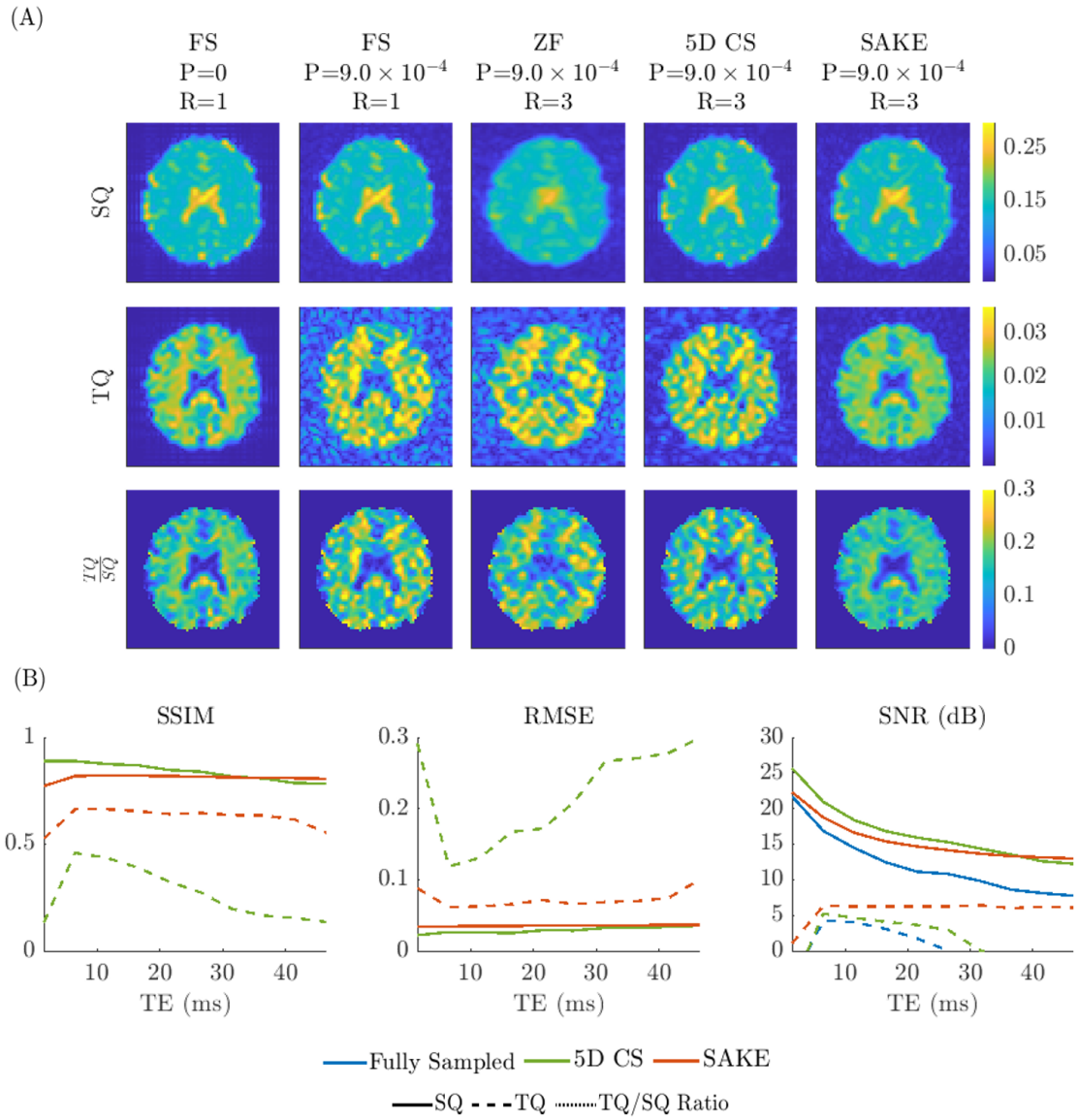

Figure 4.8: (A) Numerical simulations of 3-fold undersampled ^{23}Na MQC MRI reconstructed with 5D CS and the SAKE framework. (B) Quantitative evaluation of reconstruction performance via SSIM, RMSE, and SNR over different undersampling factors, R.

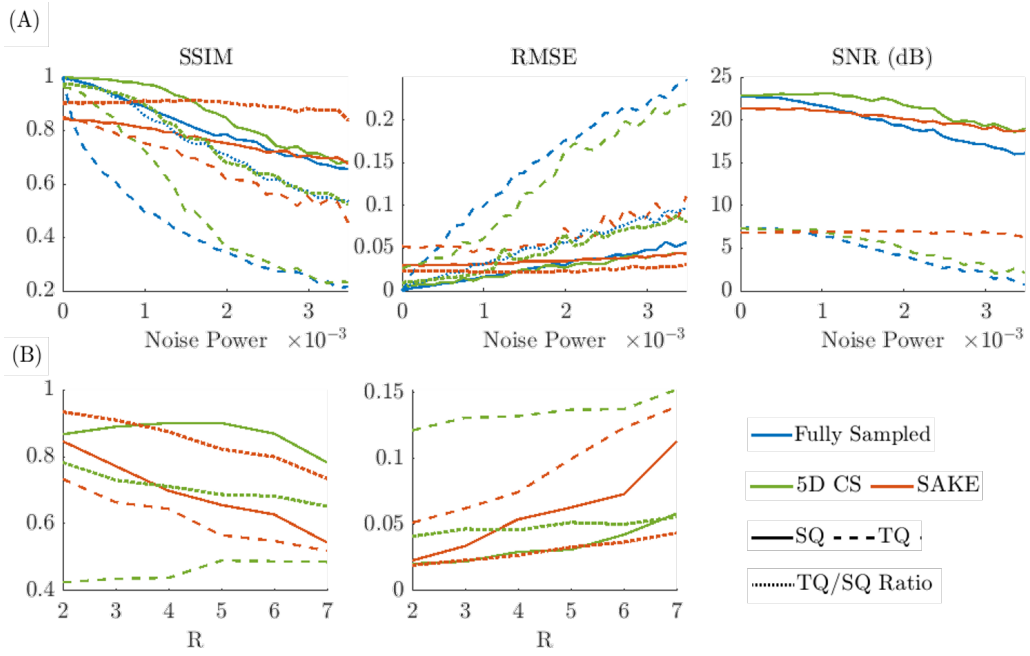

Figure 4.9: Quantitative evaluation of reconstruction performance regarding SSIM, RMSE, and SNR for simulated SQ and TQ brain data. (A) Additive noise performance evaluation for R=3, with 5D CS and SAKE reconstructed and increasing noise levels. (B) Reconstruction evaluation for different acceleration factors, R, for 5D CS and SAKE models obtained with the same noise power as used in Figure 4.8. All noise levels' mean and standard deviations were given in Table 9.5.

4.2.2 Phantom study

DHE:
A conventional ^{23}Na MR image was obtained both in conjunction without (R[MQC]=1) and with (R[MQC]=3) prospective undersampling of the ^{23}Na MQC data. The DHE image obtained from (R[MQC]=1) corresponded to 4 averages, which provided sharp image details and a high signal-to-noise ratio. The DHE image obtained with prospective MQC undersampling (R[MQC]=3) corresponded to 2 averages and suffered a lower SNR. It was found that the vials with the highest sodium concentrations (3, 6, and 9) exhibited the highest signal intensity, and vials 1, 4, and 7, with 50 mM, had the lowest signal intensity. DHE images allowed to estimate TSC regardless of agar concentrations thanks to its very short echo time reducing its sensitivity to T_2^* decay: regression between DHE ^{23}Na signal intensity versus prior known TSC confirmed a linear relationship with R^2=0.99* for both DHE images ($p<0.05$). The SNR of the DHE images was 17.31 dB and 16.32 dB for fully sampled and prospectively undersampled MQC acquisitions, respectively.

MQC:
SNR of fully sampled and retrospectively undersampled, reconstructed with either 5D CS or SAKE, ^{23}Na MQC images were 19.68/ 6.69 dB, 23.58/ 8.77 dB, and 21.56/ 9.70 dB, for SQ and TQ, respectively. Similarly, SNR for prospectively undersampled SQ and TQ signals were 20.98/ 9.36 dB and 19.25/ 6.94 dB for 5D CS and SAKE, respectively. Vials without agar (1 to 3) did not show any TQ signal, while vial 9,

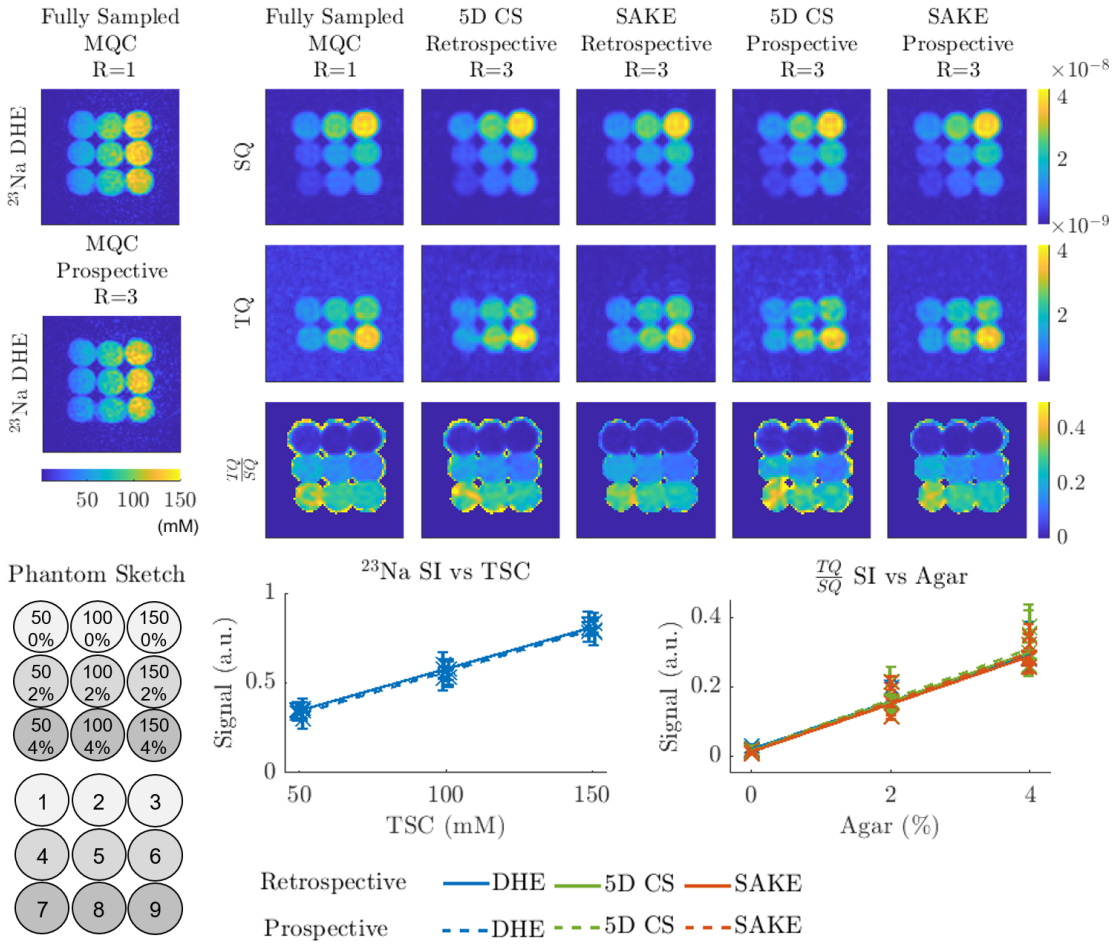

Figure 4.10: Phantom design consisting of 9 different vials (350 mL each) with different NaCl (50, 100, 150 mM) and varying agar concentrations (0, 2 and 4%). Center slice image reconstruction comparison of 5D CS and SAKE for 3-fold retro- and prospectively undersampled ^{23}Na MQC MRI. Additionally, the ^{23}Na DHE image is shown, which is obtainable without and with prospective undersampling of ^{23}Na MQC MRI. Linear regression was performed to evaluate the linear relationship of the average signal intensity (SI) of ^{23}Na and TQ/SQ ratio with respect to the prior known TSC or agar gel concentration. Solid lines correspond to retrospectively, dashed lines to prospectively undersampled ^{23}Na MQC MRI.

with the highest agar and sodium concentrations, exhibited the highest TQ signal intensity. Regression on both 5D CS or SAKE reconstructed images between mean TQ/SQ ratio signal intensity and prior known agar concentration revealed excellent linear relationships (R^2=0.92* for fully sampled, R^2=0.93* and R^2=0.94* for retrospective 5D CS and SAKE, respectively). Prospectively undersampled TQ/SQ ratio exhibited equivalent linear relationships of R^2=0.91* and R^2=0.92* for 5D CS and SAKE, respectively.

4.2.3 Drop-in-place and low-rank Double Half-Echo reconstruction

The 'drop-in-place' method showed residual smearing artifacts along the readout direction. In contrast, the low-rank DHE framework provided artifact-free images

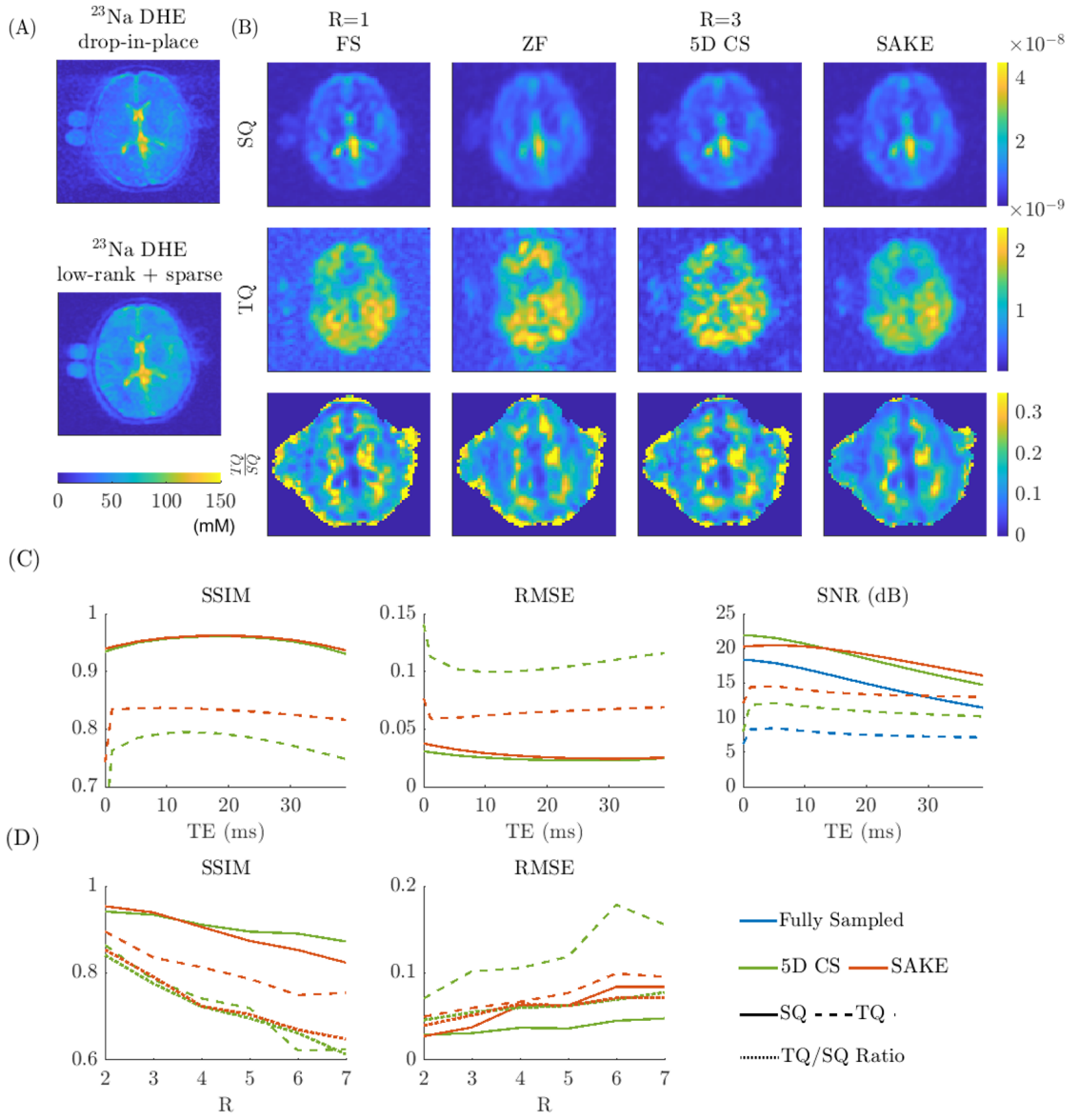

Figure 4.11: Retrospective in vivo undersampling study. (A) In vivo reconstruction results shown for 'drop-in-place' and low-rank + sparse method of ^{23}Na DHE. (B) Original and retrospectively undersampled (R=3), with zero-filling (ZF), 5D CS, and SAKE reconstructed ^{23}Na MQC MRI. (C) Quantitative analysis regarding SSIM, RMSE, and SNR evaluated over the echo time, TE.

with enhanced imaging details, confirmed by the focus measure, $FM = 0.0026$ vs 0.0029 for the 'drop-in-place' and DHE methods. DHE images reconstructed with the low-rank framework exhibited estimated mean TSC values of 52 ± 12, 51 ± 9, and 113 ± 16 mM for WM, GM, and CSF, respectively.

4.2.4 MQC retrospective undersampling in vivo study

Despite 3-fold undersampling, SAKE enabled adequate reconstruction of SQ and TQ signal components. The TQ image quality was improved over 5D CS, exhibiting apparent structures corresponding to the fully sampled image (Figure 4.11, C and D,

and Table Table 4.2, B). These similarities were also reflected in the TQ/SQ ratio, which was highest in WM and lowest in the CSF. Interestingly, 5D CS provided slightly higher SQ image quality (SSIM = 0.934 vs 0.939, RMSE = 0.031 vs 0.038, respectively), whereas SAKE provided improved TQ image reconstruction (SSIM = 0.784 vs 0.836, RMSE = 0.101 vs 0.051). SAKE proved enhanced TQ image reconstruction across various undersampling factors (Figure 4.11, D).

4.2.5 MQC prospective undersampling in vivo study

DHE:
The new sequence and the two low-rank frameworks enabled a complete depiction of ^{23}Na and ^{23}Na MQC MRI, Figure 4.13. DHE acquisition enabled TSC estimation, with TSC being the highest in the CSF compartment. Averaged TSC estimation revealed 38 ± 9, 39 ± 11 and 135 ± 20 for all shown WM, GM, and CSF volunteers.

MQC:
Prospective undersampling enabled higher spatial resolution ^{23}Na MQC MRI while reducing scan time from 2x30[28] to 2x19 minutes. TQ/SQ ratio maps enabled delineation between WM, GM, and CSF thanks to the increased spatial resolution. It was found that TQ/SQ ratios for all shown volunteers were consistently the lowest for the CSF and the highest for WM, with TQ/SQ ratios of 0.11 ± 0.03, 0.09 ± 0.02 and 0.05 ± 0.01 for WM, GM and CSF, respectively.

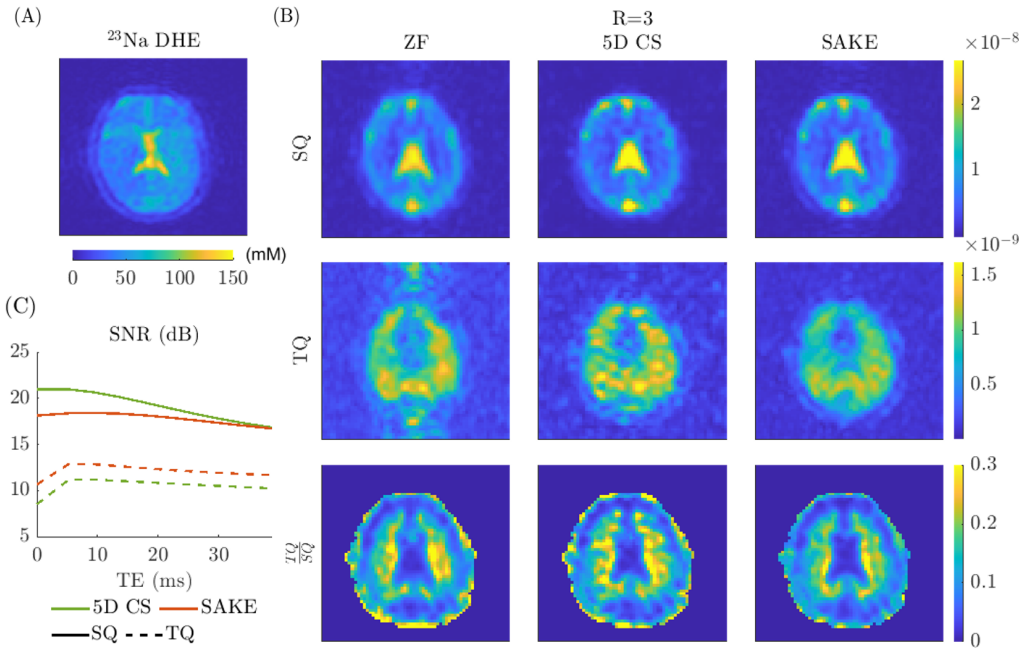

Figure 4.12: Prospective in vivo undersampling study. (A) Fully sampled ^{23}Na image obtained by leveraging the Double Half-Echo technique. (B) Prospectively undersampled (R=3), with zero-filling (ZF), 5D CS, and SAKE reconstructed ^{23}Na MQC MRI. (C) Quantitative SNR evaluation over the echo time, TE.

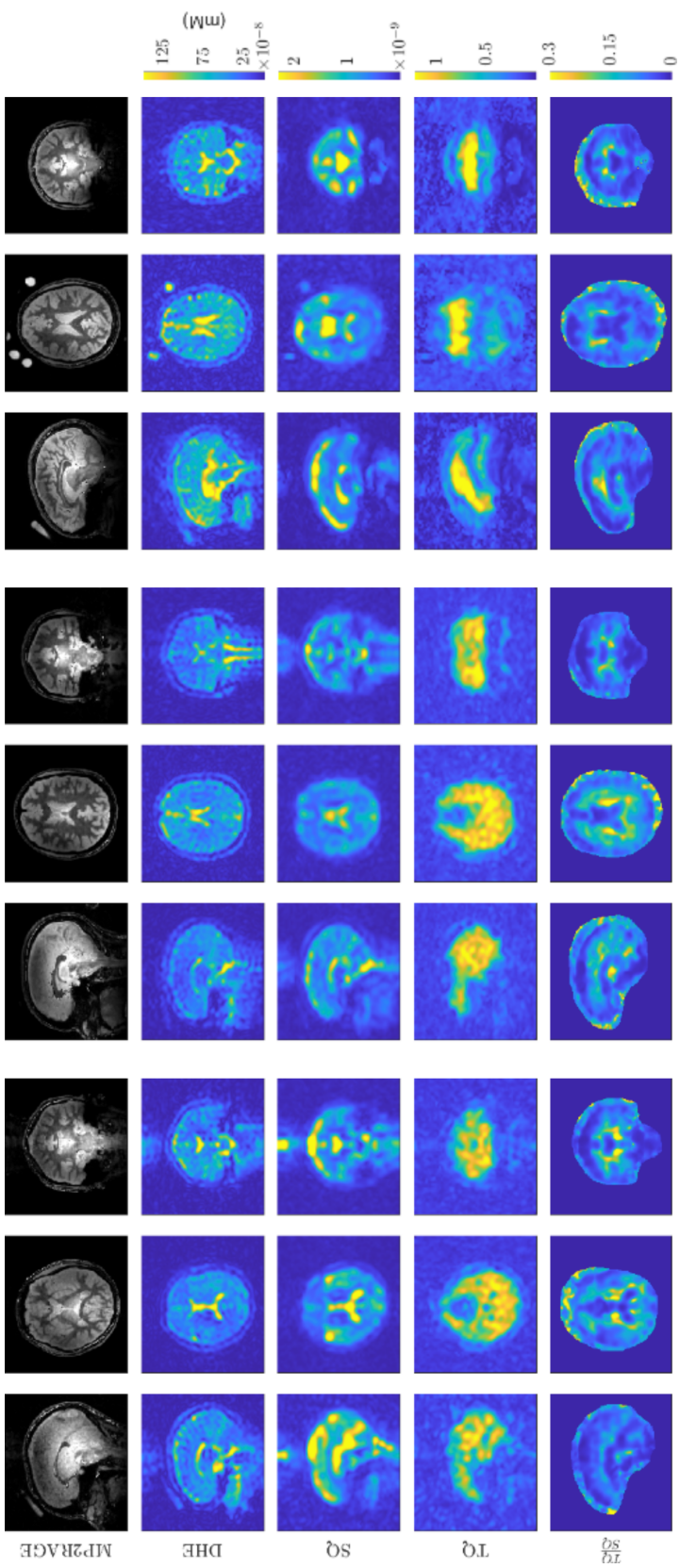

Figure 4.13: Prospective in vivo undersampling study. Reconstructed MP2RAGE, DHE, and prospectively undersampled (R=3) ^{23}Na MQC MRI shown for three volunteers in sagittal, transverse, and coronal orientations.

Table 4.2: SSIM, RMSE, and SNR evaluation of retrospectively undersampled ^{23}Na MQC MRI, reconstructed with either 5D CS or SAKE for (A) in silico and (B) in vivo. $CS_{R=3}$ and $SAKE_{R=3}$ represent the metrics for R=3 for SQ or TQ. Table (A) corresponds to the numerical simulation (fully sampled: SNR SQ = 21.72 dB, TQ = 4.03 dB) and (B) to the in vivo study performed at 7 T (fully sampled: SNR SQ = 18.52 dB, TQ = 8.62 dB).

	Model	Signal	SSIM	RMSE	SNR (dB)
(A)		SQ	0.89	0.022	25.66
	5D $CS_{R=3}$	TQ	0.44	0.131	4.63
		TQ/SQ	0.73	0.047	–
		SQ	0.82	0.033	22.31
	$SAKE_{R=3}$	TQ	0.66	0.062	6.24
		TQ/SQ	0.91	0.023	–
(B)		SQ	0.934	0.031	21.91
	5D $CS_{R=3}$	TQ	0.784	0.101	12.11
		TQ/SQ	0.876	0.055	–
		SQ	0.939	0.038	20.24
	$SAKE_{R=3}$	TQ	0.836	0.060	14.53
		TQ/SQ	0.792	0.051	–

5. Discussion

This chapter discusses the presented sparse and low-rank reconstruction frameworks to advance ^{23}Na MQC MRI on clinical scanners. Section 5.1 discusses Compressed Sensing-based reconstructions and Section 5.2 discusses the results for low-rank reconstruction for ^{23}Na and ^{23}Na MQC MRI. Parts of this chapter have been published in Licht et al.[28] and Licht et al.[70] by Wiley.

5.1 Multi-Dimensional Compressed Sensing reconstruction to advance ^{23}Na MQC MRI on clinical scanners

This study showed that Compressed Sensing (CS) could be used for two major limitations of ^{23}Na multi-quantum coherence MRI: elongated acquisition time and poor spatial resolution. Compressed Sensing for ^{23}Na MQC MRI was evaluated in four steps. First, a numerical simulation framework allowed to demonstrate the limitations of 3D CS and the necessity to deploy 5D CS for this application. However, numerical simulations, based on a simplistic segmentation of the human brain, lacked realistic data with considerations for imperfect B_1^+ and B_0. Second, a calibrated phantom confirmed experimentally the advantages of 5D CS over 3D CS. These experiments clearly showed the limitations of 3D CS in providing reliable results in low sodium concentration compartments. Nevertheless, phantom experiments offer beneficial conditions such as large homogeneous regions. Third, a retrospective study was performed on in vivo data acquired at 3 T. These data provided the first opportunity to test various undersampling rates on in vivo data retrospectively. The challenge was complete with all the elements to account for the B_1^+ and B_0 relative inhomogeneity, the relatively lower SNR of a 3 T sodium head MRI, and the elongated scan duration for a fully sampled acquisition. Conventional distance metrics such as SSIM and RMSE did not always reflect visually perceived reconstruction improvement. These reconstruction performance evaluations may not be appropriate since they also take irrelevant structures, such as the skull, into account, skewing the metric evaluation. Strong from all these incremental validations of our 5D CS framework, a prospectively undersampled in vivo acquisition was implemented. An unprecedented spatial resolution for ^{23}Na MQC MRI was sought as a fourth step. Alternatively, a shortened acquisition could have been performed, although this option was not significantly different from the retrospective study. Eventually, with an undersampling rate of 2, a 2.7-fold reduction of voxel volumes and the boost in SNR thanks to the 7 T, whole brain ^{23}Na MQC MRI was acquired with a resolution of 6x6x10mm^3. A sharper distinction between gray and white matter MQC properties could be observed in these images.

5.1.1 7 T in vivo study

Transitioning from 3 T to 7 T boosted the SNR, enabling potentially higher acceleration. However, higher field strengths come with stricter SAR limitations, adversely prolonging acquisition due to increased TR and diminishing the benefits of ultra-high field ^{23}Na MQC MRI. Moreover, the TQ signal highly depends on B_1^+ as it scales with $sin^5(\alpha)$, further penalizing 7 T acquisitions. Future work could utilize

flip angle mapping for B_1^+ post-processing correction.[42] This study only considered dual-tuned birdcage coils with single transmit and receive channels, both at 3 T and 7 T. Utilizing multi-receive channels could further push acceleration thanks to SNR improvements and by simultaneously leveraging parallel acquisition techniques.[85] Nevertheless, further work is needed to improve in vivo TSC quantification, which could be achieved by including more echoes to enhance the fit.

5.1.2 Potential extensions to proposed image reconstruction

Additionally, changing the sampling pattern more frequently, e.g., for each repetition and/or along the echo time, would reduce the fully sampled center region and increase incoherence, potentially improving reconstruction quality. CRISTINA phase-cycle leveraged 2x6 steps for the Fleysher combination[46] to compensate for B_0 inhomogeneity-induced signal loss occurring during the evolution time. To accommodate the Fleysher combination, data sets χ_0 and χ_{90} were identically undersampled in the current implementation. However, one could consider undersampling each data set differently and combining them to extend the phase cycle dimension for CS reconstruction, albeit with a different transform than the Fourier transform employed in the presented algorithm.

Another extension from the proposed CS model could be to exploit joint constraints across the multi-dimensional space instead of individual constraints. The chosen separated framework permitted independent scaling of each regularization term, allowing tuning them for optimal reconstruction results since sparsity might differ among the 5 dimensions. Another joint approach could be tensor sparsity. Leveraging multi-dimensional sparsity simultaneously, as proposed by Yu et al.[86] or Roohi et al.[87] could improve image reconstruction. Additionally, improved reconstruction could be achievable by exploiting k-space similarity such as in LORAKS[88] or SAKE[89] and thus not limiting the reconstruction to sparsity assumptions only. It is also noteworthy that CS reconstruction performances are highly dependent on the initial SNR of the signal. Hence, reconstruction performance and achievable acceleration factors are severely limited by ^{23}Na MQC MRI's intrinsically poor SNR, yielding noisy images even though fully sampled k-space was acquired. Following, spatial TV sparsity could be improved by leveraging anatomical prior constraints as proposed by Gnahm et al.[90], Lachner et al.[91], and Zhao et al.[92].

Another limitation of ^{23}Na MQC MRI is that its TSC differs from the TSC measured by conventional ^{23}Na MRI. Indeed, CRISTINA's apparent TSC is affected by T_2^* due to the long evolution time. A more accurate TSC estimation could be obtained by using an additional readout during the evolution time by leveraging a UTE readout as included in the SISTINA[40] sequence. Following Aldung et al.[84] work, the CSF was used as a reference in vivo to quantify TSC since it is less affected by B_1^+ inhomogeneity and noise due to short T_2 components compared to external vials placed at the edges of the coil with agar content reducing their T_2 values.

5.1.3 Alternatives for improved image reconstruction

First, further reconstruction improvements could be expected by leveraging convolutional neural networks proposed by Adlung et al.[93]. In particular, deep learning techniques could be used to find optimal sparse signal representations.[94] Joint frameworks combining Deep Learning and Compressed Sensing have also shown promising results in regards to reduced reconstruction time[95] or overall enhanced reconstruction quality by exploiting relevant features in the images.[96] Nevertheless, the performance highly depends on the amount of training data, which remains limited for ^{23}Na MQC MRI.

Second, reconstruction parameters were determined empirically based on SSIM and RMSE assessment. Due to the intrinsic low SNR of the signal, optimization of reconstruction parameters was challenging. Further research could utilize Automated Parameter Selection for Accelerated MRI Reconstruction as proposed by Ilicak et al.[58] Furthermore, estimating the noise floor and computing the sparsity threshold for this parameter could help find optimal sparsity thresholds for each dimension.

Third, the presented workflow was separated into image reconstruction (CS) and image post-processing, which consisted of the Fleysher combination and model-based reconstruction of fitting the signal equations. Future work could evaluate the benefits of combining these steps by leveraging CS coupled with a model-based reconstruction[97] that incorporates SQ and TQ signal fitting into CS. The presented 5D CS model exploits shared information of the superimposed ^{23}Na MQC signal and the spectrum by computing the 1D Fourier transform along the phase-cycling dimension. Hence, the proposed 5D CS algorithm could easily be extended, with additions for T_2^* signal decay, to a model-based image reconstruction that considers relevant physical parameters and leverages the theoretical SQ and TQ signal models. However, these model-based approaches add another level of complexity and risk overfitting[97], which was deemed beyond the scope of this study.

Finally, the CRISTINA sequence is based on Cartesian readouts, which are SNR efficient since they sample k-space more evenly. Alternatively, non-Cartesian readouts might be better suited to fulfill the prerequisite of incoherent undersampling noise required for CS. Nevertheless, Cartesian sampling eases reconstruction procedure, notably memory when handling large datasets, and is more robust to hardware imperfections, potentially fostering reproducibility across different platforms. Furthermore, alternating the sampling patterns along the phase cycle dimension promoted incoherent undersampling artifacts, thus better satisfying CS reconstruction theory. Further acceleration, however, could be achieved by leveraging Twisted Projection Imaging[67] or radial density-adapted[68] radial k-space sampling because these methods provide increased initial SNR and additionally, enhance sampling randomness. However, the 3D variable density Cartesian sampling technique has already demonstrated potential in multiple CS applications. Furthermore, the proposed multi-dimensional CS model's strength lies in regularizing the phase-cycle dimension, which would be similar between Cartesian and non-Cartesian sampling trajectories. Finally, paired with a strong asymmetric first echo, ^{23}Na MQC signal Cartesian sampling could be performed with a short first echo time, benefiting the SQ signal. Later echoes were fully sampled to balance the lower SNR, especially for sampling the TQ signal.

5.2 Low-Rank reconstruction to advance ^{23}Na MQC MRI on clinical scanners

It was demonstrated that low-rank reconstruction frameworks offer a double benefit to advance ^{23}Na and ^{23}Na MQC MRI. By leveraging the Double Half-Echo technique, we have shown that Cartesian sampling can acquire ^{23}Na MR images. Utilizing a low-rank coupling constraint, aliasing free ^{23}Na MR images were reconstructed. Additionally, we demonstrated that ^{23}Na MQC MRI could be accelerated by taking advantage of the shared information across its multi-dimensional space. The SAKE framework was used to reconstruct the undersampled images. Based on the analysis of in silico, in vitro, and in vivo experiments, we further showed the possibility of combining both low-rank reconstruction frameworks into one acquisition to simultaneously obtain high-quality ^{23}Na and higher resolution ^{23}Na MQC MRI of the human brain at 7 T.

DHE
The low-rank coupling constraint identifies correlations along the rows, and by minimizing the rank and singular value thresholding, artifacts arising from undersampled k-space were reduced. The oversampling of the k-space center represents a redundant subspace exhibiting highly coherent information. The DHE reconstruction framework uses this redundant subspace to concatenate both k-space halves efficiently.

MQC
The discrepancy between 5D CS and SAKE in improving the reconstruction of SQ and TQ images parallels the nature of their signals. Our results showed that 5D CS favored SQ while SAKE was more suited for TQ reconstruction. SQ signal offers a higher initial SNR but is evanescent, with an exponential decay well suited for sparsity transformations but undermines its coherence across echo times. Oppositely, the TQ signal is of low SNR but persists in time. Thus, the TQ signal is challenging to dissociate from background noise using sparsifying transforms, as in Compressed Sensing, but adequate for the low-rank assumption employed in the presented framework. The question remains whether the two approaches can be combined to adapt the reconstruction of each signal to their inherent nature and offer the best of the two worlds.

5.2.1 Numerical simulations

DHE:
The simulations provided a theoretical framework to test optimal sequence and image reconstruction parameters. A slightly increased echo fraction (52%) provided the best image reconstruction. This was owed to the fact that if 50% of k-space was sampled, no overlap in the k-space center was given, which could be used to exploit coherent information shared across the two k-space halves. Once the echo fraction exceeds 50%, the low-rank coupling constraint exploited redundant data in the k-space center to optimally concatenate both k-space halves by minimizing the joint rank of both halves. However, ^{23}Na MRI requires short echo times, which favors slight k-space center overlaps for both k-space halves. Numerical simulations demonstrated that an echo fraction of 52% was a good compromise between accurate image reconstruction (high SSIM) and enabling a short echo time (TE=0.5 ms).

MQC:
It has been demonstrated that most of the data's variance along the echo and phase-cycle dimension is concentrated in a subset of singular values (Figure 9.7, A). ^{23}Na MQC MRI's multi-dimensional signal structure is therefore well captured in low-rank matrices and optimally suited for low-rank reconstruction frameworks. Interestingly, the TQ's quantitative metric evaluation (Figure 4.8, B and Figure 4.11, C) reconstructed with SAKE revealed that exploiting the multi-dimensional structure of ^{23}Na MQC MRI simultaneously, efficiently identified coherent information, which in return supported the reconstruction of later echoes. This is owed to the fact that the largest singular values correspond to the signal components with the highest magnitude, which in the case of the TQ signal is at TE=$\approx$ 10 ms. The information was used to reconstruct later echoes, which suffered lower SNR (Figure 4.8, B). This claim was supported by the high SSIM and reduced RMSE that SAKE exhibited for TQ. Furthermore, since noise is highly incoherent, the low-rank approximation intrinsically filters noise and improves TQ signal reconstruction. As a result, the SNR evaluation over TE is almost constant for SAKE reconstructed ^{23}Na MQC MRI, especially when compared to the fully sampled data (Figure 4.8, B and Figure 4.11, C). On the other hand, SAKE failed to provide optimal reconstruction results for the SQ signal. Even though SAKE yielded aliasing-free and reduced blurring in SQ images, 5D CS still outperformed SAKE in SQ reconstruction. SQ signal decays rapidly after excitation, which intrinsically full-fills sparsity assumptions. As a result, SQ is optimally reconstructed by leveraging a sparse reconstruction model, and TQ benefits primarily from low-rank reconstruction frameworks that exploit coherent information across the multi-dimensional space. It is shown that low-rank matrices are very well suited to filter for a high amount of noise across the multi-dimensional space (Figure 4.8). As noise is highly incoherent, the singular values are small and, thus, thresholded by leveraging SVT. With increasing noise levels, SAKE provided highly increased reconstruction performance compared to 5D CS, already at noise levels of >1x10^{-3} (Figure 4.9.

5.2.2 Phantom study

DHE:
Based on the results of the phantom DHE images (2 and 4 averages), it could be concluded that the DHE reconstruction framework benefits from increased initial SNR. The DHE image reconstructed from 4 averages exhibited sharper imaging details and less background noise than the DHE image obtained from two averages, supported by the SNR analysis. However, doubling the number of averages should yield an SNR increase of $\approx \sqrt{2}$, which was not seen in this case. This is owed to the fact that the DHE reconstruction framework is non-linear because it optimizes the objective function iteratively. In addition, using singular value thresholding by leveraging a minimum variance filter influenced SNR. Despite the varying agar concentrations in vials 3, 6, and 9, the DHE images' signal intensity was similar. Conclusively, the employed echo time was short enough to determine accurate TSC. The DHE images obtained with and without prospective undersampling of MQC data exhibited similar signal intensities and R^2 values, indicating that obtaining a ^{23}Na DHE image is possible with and without undersampling of ^{23}Na MQC MRI.

MQC:
The phantom study revealed accurate SQ and TQ signal reconstruction despite a high retrospective and prospective undersampling factor of R=3. Since vials 1 to 3 did not contain agar gel, no TQ signal was observed for the respective tubes. Nevertheless, incorporating a model-based reconstruction by fitting the signal equations during each iteration of SAKE could improve the reconstruction results. Additionally, SAKE's performance highly relies on accurate thresholding values, which are yet to be found. Furthermore, the complexity of finding the optimal regularization value scales with the dimensionality of the data and, therefore, future work could leverage an automated parameter selection algorithm as proposed by Ilicak et al.[58]. Nevertheless, a strong linear relationship was observed between the TQ/SQ ratio and prior known agar concentration, indicating accurate TQ signal reconstruction.

5.2.3 Retrospective and prospective in vivo study

DHE:
Leveraging the knowledge from numerical simulations, the DHE framework enabled the acquisition of high-resolution sodium MRI in vivo. Since a relatively conservative spatial resolution of 3x3x15 mm^3 was chosen, severe partial volume effects were observed, especially in the central CSF compartment (Figure 4.11, A). Finally, completely decoupling the DHE acquisition from the MQC acquisition enabled the acquisition of conventional high-resolution sodium MRI while prospectively undersampling the MQC acquisition. Hence, a high-resolution DHE sodium MRI of 6x6x6 mm^3 was obtained (Figure 4.13). Nevertheless, partial volume effects were observed, which suggests a further increase in the spatial resolution of the DHE images by also enhancing sampling efficiency.

MQC:
The retrospective analysis revealed that SAKE accurately reconstructed undersampled ^{23}Na MQC MRI (Figure 4.11, B and C). Accurate reconstruction performance was given for an acceleration factor of R=3; therefore, prospective undersampling was performed with the same acceleration factor. This enabled to reduce acquisition time while increasing the spatial resolution of ^{23}Na MQC MRI from 8x8x15 mm^3 to 8x8x8 mm^3. Similarly to the numerical phantom study, SAKE improved TQ image reconstruction regarding SSIM and RMSE. Again, by simultaneously exploiting coherent information across the multi-dimensional space spanned by ^{23}Na MQC MRI, information from earlier echoes could be leveraged to support the reconstruction of later echoes. Despite the TQ signal being of small amplitude, it is highly coherent along the echo time, efficiently exploited in the 2D Hankel-like matrix involved in the SAKE framework.

One advantage of the proposed sequence and the low-rank frameworks is that all images are Cartesian sampled, which enables direct correlation of the images. Correlating ^{23}Na and ^{23}Na MQC MRI revealed that the conventional sodium and the SQ signal exhibited similar intensity distributions, with the highest signal intensity found in the CSF compartment. On the other hand, the direct correlation showed that the TQ signal pre-dominantly arose from the brain parenchyma, e.g., WM and GM. The presented SQ and TQ contrasts carry different information about the tissue, with the TQ signal being sensitive to restricted sodium ions.

Computing the TQ/SQ ratio maps revealed consistent ratio values, which could enable the normalization of the TQ signal with respect to the SQ signal. Following this, the TQ/SQ ratio could potentially provide an additional quantitative metric besides TSC. This study demonstrated that a consistent TQ/SQ ratio throughout retro- and prospectively undersampled ^{23}Na MQC MRI was found and fostered the potential to be used as an additional quantitative metric.

5.2.4 Potential extensions to proposed image reconstruction

Similarly to Liu et al.[98], complementary information of adjacent partitions could be leveraged to improve DHE image reconstruction. Variable density undersampling coupled with a Compressed Sensing iterative reconstruction scheme could improve DHE ^{23}Na MRI sampling. Furthermore, an oversampling factor of 2 along the readout direction was used in this study but could be increased to enhance redundancy, improving image reconstruction and potentially enabling 50% echo fraction sampling. Thanks to the Cartesian nature of DHE, its utilization with ^{23}Na multi-coil arrays would allow parallel imaging acquisition techniques to improve acquisition speed further. However, this work was limited to a single-channel transmit and receive coil; thus, this option was not further investigated. Nevertheless, the low-rank framework reconstruction can easily be extended with parallel imaging.[99] Alternatively, leveraging convolutional neural networks proposed by Adlung et al.[93] is a promising avenue for improved reconstruction results.

Future work could leverage the DHE technique for ^{23}Na MQC echoes to sample the signal evolution more densely. Hence, small echo spacings could be possible, potentially providing higher SNR TQ images. Generally, multi-echo acquisitions, especially for sodium MRI, could benefit from the DHE sampling scheme. Short relaxation times lead to T_2^* blurring, which could be mitigated by reduced readout times because only half of k-space is acquired. The discretized signal along the multi-echo dimension could be denser sampled with fewer blurring artifacts, yielding the potential to quantify T_2^* more accurately. In addition, leveraging the Cartesian DHE to acquire sodium MRI also opens the possibility of utilizing a non-isotropic field of view, which could benefit the emerging field of sodium skin MRI.[100]

6. Summary

This thesis work's main objective was to advance ^{23}Na MQC MRI on clinical scanners. The motivation for investigating ^{23}Na MQC MRI is to offer novel tissue information closely related to cellular health status. Nevertheless, it suffers from low SNR, long acquisition times, and limited spatial resolution. Following, acceleration by drastic undersampling of ^{23}Na MQC MRI coupled with dedicated reconstruction frameworks that take advantage of the ^{23}Na MQC MRI's signal structure was proposed. This thesis' key contributions were:

1. For the first time, the reconstruction frameworks for ^{23}Na MQC MRI were extensively studied in silico, in vitro, and particularly interesting, in vivo at both 3 T and 7 T MRI, enabling sound conclusions.
2. Application of the Compressed Sensing theory and the development of a dedicated multi-dimensional model to enable 3-fold acceleration of ^{23}Na MQC MRI.
3. For the first time, prospective undersampling enabled higher resolution 6x6x10 mm^3 TQ/SQ ratio maps acquired at 7 T MRI.
4. An efficient sequence for simultaneous ^{23}Na and ^{23}Na MQC MRI was proposed.
5. Low-rank reconstructions exploiting signal's intrinsic redundancy enable Double Half-Echo ^{23}Na and undersampled ^{23}Na MQC MRI.

Regarding the leading research question of this thesis, defined as "**Can knowledge-driven image reconstruction improve ^{23}Na MQC MRI towards faster and better resolved whole-brain sodium quantitative imaging?**", it has been demonstrated that robust acceleration, coupled with sparse and low-rank reconstruction models, led to better resolved whole-brain sodium quantitative imaging by 1) enhanced spatial resolution and 2) enabling a comprehensive analysis of sodium signals in a single acquisition.

With the basics for accelerated ^{23}Na MQC MRI given, future research could, in particular, investigate:

1. Extension of the reconstruction frameworks to also account for T_2^* signal decay by leveraging a physical signal model.
2. Analysis of the potential to further accelerate the acquisition by undersampling the phase-cycling steps and the phase-encoding lines of the k-space matrix.
3. Leverage prospective undersampling to increase spatial resolution on >7 T MRI scanners.
4. Investigation of ^{23}Na MQC MRI in clinically-focused studies such as brain tumors or radiotherapy.
5. Application of machine-learning-based approaches to improve post-processing.
6. Deploying prospective variable-density undersampling combined with sparse image reconstruction to improve ^{23}Na DHE MRI and utilization of multi-receive coils.
7. Exploration of the benefits of leveraging parallel RF transmit techniques.
8. In-depth study to compare non-Cartesian against Cartesian Double Half-Echo ^{23}Na MRI.

A more detailed description of each point can be found in the Outlook section.

7. Outlook

Multiple avenues exist to further research sodium multi-quantum MRI and explore proposed acceleration techniques in other multidimensional MRI techniques. One interesting step to improve the reconstruction would be to leverage the theoretical information about the signal. Including physical signal models taking T_2^* decay into account would help improve image reconstruction. Furthermore, this prior information could be used to synthesize missing data points and, therefore, increase undersampling potential. Extending the presented CS-based approach to a more model-based refinement approach, with model-based image reconstructions getting increased attention due to its wide range of applications,[97] could improve image reconstruction quality. Despite the computational load, model-based reconstructions have the advantage of providing quantitative maps of physical parameters.[101]

This thesis focused on undersampling the phase-encoding lines of the k-space matrix to reduce acquisition time. However, closely related to the model-based approach, one could also consider undersampling the phase-cycling steps, i.e., only acquiring 4 out of 6 phase-cycle steps to speed up the acquisition. As we have demonstrated, phase cycling creates replicas of the signal that vary in phase and magnitude. Following, phase-cycling produces redundant subspaces, making it a linear reconstruction problem restricted to the pre-determined subspace of the fixed number of phase-cycle steps and, therefore, ideally suited for subspace reconstruction frameworks.[102] Leveraging prior information about the RF pulses and phase-cycling scheme coupled with the model-based reconstruction framework could enable the reconstruction of missing phase-cycle steps. This framework would not be limited to ^{23}Na MQC MRI. Still, it would apply to all MRI experiments that involve RF phase-cycling, such as balanced steady-state free precession (bSSFP) for non-contrast-enhanced MRI[103] or simultaneous T_1 and T_2 mapping.[104]

^{23}Na MQC MRI on different field strengths

Despite this thesis' work being majoritarily focused on 7 Tesla MRI, ^{23}Na MQC MRI could also benefit from the acceleration at other lower fields (<3 T). Despite the initially low SNR, short TRs with several repetitions to oversample the k-space center could enable MQC MRI on 1.5 T. Another benefit would be the decrease in B_1^+-related issues and shortened RF pulses, which would minimize relaxation effects during excitation.

Providing access to MQC acquisitions on clinical 3 T scanner enables more ^{23}Na MQC MRI data to be collected that could be leveraged for Machine Learning approaches, i.e., deep-learning-based reconstructions. Unfortunately, MQC MRI data is still rare and thus hinders the potential to create dictionaries or AI-based post-processing frameworks as proposed by Adlung et al.[93]. Further, considering the clinical aspect, 3 T MRI is highly interesting for clinical studies.

While there is a clear advantage of acceleration on clinically used field strengths, ^{23}Na MQC MRI on ultra-high field systems (>7 T) is also of particular interest. Even though B_1^+ issues and longer TRs are more severe,[105] acceleration could also benefit ultra-high field acquisitions, making it more applicable as a research tool.

Concerning B_1^+-related issues, parallel transmit techniques could help improve TQ imaging, especially in regions at the periphery of the brain.

The advantage of simultaneous ^{23}Na and ^{23}Na MQC MRI

This thesis is the first to offer combined and accelerated conventional and multi-quantum sodium MRI solely based on Cartesian sampling. This combination is especially interesting as an extensive application of ^{23}Na and ^{23}Na MQC MRI in brain tumors. Fiege et al.[40] have already demonstrated altered TQ signal intensity in brain tumors. Paired with the TQ/SQ ratio, a new parameter could be investigated throughout treatment to track treatment response. We have demonstrated that the TQ/SQ ratio is reproducible across various acquisitions and is well suited to be tested in a more clinical-oriented setting, i.e., radiotherapy.[106] With the increasing interest in multinuclear MRI, improved hardware, and the herein proposed sequence, an efficient framework offers the potential to correlate directly ^{23}Na and ^{23}Na MQC. Hence, future research on the clinical application of ^{23}Na MQC MRI will significantly benefit from the proposed sequence and image reconstruction frameworks.

Post-processing non-Cartesian ^{23}Na MRI is challenging as it requires gradient corrections and complex image reconstruction. The Cartesian DHE framework presented here might ease these steps and offer a simple plug-and-play solution for different scanners and institutions. Furthermore, the given DHE sequence has the potential to acquire an asymmetric field of view, which could be of high interest for the emerging field of sodium skin or breast MRI.[100, 107].

To extend the benefits of Cartesian ^{23}Na DHE MRI, its sampling needs to be optimized, for example, by deploying 3D elliptical scanning. Elliptical selection would reduce acquisition time by skipping high-frequency information, which can be regained by homodyne reconstructions.[108, 109] However, more advanced sampling strategies, e.g., using variable density undersampling, could accelerate ^{23}Na DHE MRI. It would necessitate leveraging non-linear reconstruction frameworks, such as sparse reconstruction models.[57] However, to take complete advantage of the DHE framework, a multi-receive coil must be used. The low-rank framework exploits the redundancy of both k-space halves, and this redundancy is enhanced with an increasing number of coil elements. Furthermore, the phased-array coils provide higher SNR gains,[110] which will also benefit DHE reconstruction.

Finally, an extensive study comparing non-Cartesian (e.g., radial, elliptical k-space sampling) with Cartesian DHE is warranted. Despite non-Cartesian sampling providing ultra-short echo times and efficient k-space coverage, it suffers from degraded point-spread functions and is susceptible to gradient system imperfections. Considering these differences, an extensive study in vitro and in vivo is thus warranted to demonstrate the performance of Cartesian DHE when compared to the gold standard non-Cartesian UTE sequences.

Impact to the ^{23}Na community

The sodium MRI community remains exclusive to a few research centers but is rapidly growing thanks to the advent of multinuclear ultra-high field MRI scanners. This thesis is a perfect example as it emerged from a two-center collaboration to investigate ^{23}Na MQC MRI on 3 and 7 T scanners. Testing clinically relevant field strengths is essential to embed sodium MRI as a clinical tool. Following, this thesis work showed the broad applicability of ^{23}Na MQC MRI on different field strengths, also accounting for clinically relevant field strength. In conclusion, the studies extended beyond mere research scanners, yet further investigation at 3 T is required to draw more robust conclusions.

However, concepts of multi-dimensional image reconstruction frameworks are still rare in MRI, especially in ^{23}Na MRI. However, we have demonstrated the benefits of leveraging our understanding of the MR signal structure to advance the acquisition. Even though sparse reconstructions in terms of Compressed Sensing and anatomically constrained reconstructions have been proposed, low-rank reconstruction frameworks are still lacking in the sodium MR field. Indeed, we have demonstrated that sparsity and low-rank approximations are well suited for even initially low SNR signals and, therefore, further illustrate the strength of these frameworks in the context of ^{23}Na MRI.

Low-rank frameworks, however, are not limited to image reconstruction. They can also be leveraged for post-processing. Following, it could be investigated how well relaxation times, e.g., T_2^* are captured in low-rank analysis, i.e., by leveraging Dynamic Mode Decomposition (DMD[111]). Additionally, since T_2^* measurements require multi-echo sampling, it offers great potential to boost SNR by leveraging the low-rank approximations computed along the echo time. Hence, an SNR boost might improve TSC quantification and T_2^* estimations in multi-echo acquisitions. Furthermore, densely sampling the T_2^* curve is of concern for accurate relaxation time estimations. The DHE technique could enable short inter-echo spacing in two ramp times, improving multi-echo ^{23}Na MRI.

Indeed, the new sequence leveraging Cartesian DHE ^{23}Na and ^{23}Na MQC MRI combined with the reconstruction frameworks is easy to use and could be rapidly implemented at various institutions. Each sodium acquisition could thus be accompanied by MQC sampling without extending imaging time. The complete ^{23}Na signal could always be investigated instead of being limited to the TSC estimation only. However, the new sequence also allows the acquisition of ^{23}Na MRI only. Hence, the proposed sequence offers increased versatility for the sodium community and a simple-to-use image reconstruction algorithm, making it a very convenient framework overall. With the robust Cartesian sampling and low susceptibility to gradient imperfections, even further suppressed by the low-rank reconstruction, and also supporting conventional ^{1}H acceleration techniques, it could be considered to be a vendor-based sequence, which could also apply to other nuclei than ^{23}Na. Furthermore, DHE offers exciting properties that could be used even for ^{1}H MRI, i.e., reduction of TR and increased robustness against banding artifacts.[65]

8. Bibliography

[1] P. Allisy-Roberts and J. Williams, "Chapter 10 - magnetic resonance imaging," in *Farr's Physics for Medical Imaging (Second Edition)* (P. Allisy-Roberts and J. Williams, eds.), pp. 169–195, W.B. Saunders, second edition ed., 2008. (cited on Page 3, 4, and 11)

[2] U. Büll, *Klinische Nuklearmedizin*. Edition Medizin, Edition Medizin VCH, 1987. (cited on Page 3 and 6)

[3] D. Nishimura, *Principles of Magnetic Resonance Imaging*. Editor no identificado, 1996. (cited on Page 3, 4, 7, and 11)

[4] R. Brown, Y. Cheng, E. Haacke, M. Thompson, and R. Venkatesan, *Magnetic Resonance Imaging: Physical Principles and Sequence Design*. Wiley, 2014. (cited on Page 4, 6, 7, and 11)

[5] F. Bloch, "Nuclear induction," *Phys. Rev.*, vol. 70, pp. 460–474, Oct 1946. (cited on Page 4)

[6] M. Hoesl, *23Na multi-quantum coherences: from cellular spectroscopy to clinical imaging development*. PhD thesis, Ruprecht-Karls-Universität Heidelberg, 01 2020. (cited on Page 5 and 18)

[7] R. K. Harris, E. D. Becker, S. M. C. de Menezes, R. Goodfellow, and P. Granger, "Nmr nomenclature. nuclear spin properties and conventions for chemical shifts(iupac recommendations 2001)," *Pure and Applied Chemistry*, vol. 73, no. 11, pp. 1795–1818, 2001. (cited on Page 6)

[8] D. Kleimaier, *Exploring Protein Interactions with 23Na Triple-quantum MRS and 1H Chemical Exchange Saturation Transfer MRI*. PhD thesis, Ruprecht-Karls-Universität Heidelberg, 01 2021. (cited on Page 9, 15, 17, 18, and 20)

[9] I. Hermann, *Development of novel methods in quantitative magnetic resonance imaging*. PhD thesis, Ruprecht-Karls-Universität Heidelberg, 2021. (cited on Page 11)

[10] S. Kane, *Introduction to Physics in Modern Medicine*. Taylor & Francis, 2002. (cited on Page 11)

[11] G. Madelin and R. R. Regatte, "Biomedical applications of sodium mri in vivo," *Journal of magnetic resonance imaging : JMRI*, vol. 38, pp. 511–529, Sep 2013. (cited on Page 11, 16, 19, and 20)

[12] L. V. Gast, T. Platt, A. M. Nagel, and T. Gerhalter, "Recent technical developments and clinical research applications of sodium (23na) mri," *Progress in Nuclear Magnetic Resonance Spectroscopy*, vol. 138-139, pp. 1–51, 2023. (cited on Page 15)

[13] W. D. Rooney and C. S. Springer, Jr, "A comprehensive approach to the analysis and interpretation of the resonances of spins 3/2 from living systems," *NMR Biomed*, vol. 4, pp. 209–226, Oct. 1991. (cited on Page 15, 16, 17, and 20)

[14] J. Bacon, R. Gillespie, and J. Quail, "Quadrupole relaxation for a spin i = 3/2: The f19 n.m.r. spectra of bf3 and clo3f," *Canadian Journal of Chemistry*, vol. 41, pp. 3063–3069, 02 2011. (cited on Page 16)

[15] M. A. U. Hoesl, L. R. Schad, and S. Rapacchi, "Efficient 23na triple-quantum signal imaging on clinical scanners: Cartesian imaging of single and triple-quantum 23na (cristina)," *Magnetic Resonance in Medicine*, vol. 84, no. 5, pp. 2412–2428, 2020. (cited on Page 17, 20, 41, and 49)

[16] J. R. van der Maarel, "Thermal relaxation and coherence dynamics of spin 3/2. i. static and fluctuating quadrupolar interactions in the multipole basis," *Concepts in Magnetic Resonance Part A*, vol. 19A, no. 2, pp. 97–116, 2003. (cited on Page 18, 41, and 49)

[17] G. Bowden, W. Hutchison, and J. Khachan, "Tensor operator formalism for multiple-quantum nmr. 2. spins 3/2, 2, and 5/2 and general i," *Journal of Magnetic Resonance (1969)*, vol. 67, no. 3, pp. 415–437, 1986. (cited on Page 18)

[18] R. Hu, *Exploring Quadrupolar Interactions of 23Na and 35Cl with Triple-Quantum MRS/MRI*. PhD thesis, Ruprecht-Karls-Universität Heidelberg, 01 2020. (cited on Page 18)

[19] O. Zaric, V. Juras, P. Szomolanyi, M. Schreiner, M. Raudner, C. Giraudo, and S. Trattnig, "Frontiers of sodium mri revisited: From cartilage to brain imaging," *Journal of Magnetic Resonance Imaging*, vol. 54, no. 1, pp. 58–75, 2021. (cited on Page 19)

[20] R. Ouwerkerk, *Sodium MRI*, pp. 175–201. Totowa, NJ: Humana Press, 2011. (cited on Page 19)

[21] R. Ouwerkerk, K. B. Bleich, J. S. Gillen, M. G. Pomper, and P. A. Bottomley, "Tissue sodium concentration in human brain tumors as measured with 23na MR imaging," *Radiology*, vol. 227, pp. 529–537, Mar. 2003. (cited on Page 19)

[22] A. Lu, I. C. Atkinson, and K. R. Thulborn, *Sodium Magnetic Resonance Imaging and its Bioscale of Tissue Sodium Concentration*. John Wiley & Sons, Ltd, 2010. (cited on Page)

[23] K. R. Thulborn, "Quantitative sodium MR imaging: A review of its evolving role in medicine," *Neuroimage*, vol. 168, pp. 250–268, Nov. 2016. (cited on Page 19)

[24] G. Madelin, J.-S. Lee, R. R. Regatte, and A. Jerschow, "Sodium mri: Methods and applications," *Progress in Nuclear Magnetic Resonance Spectroscopy*, vol. 79, pp. 14–47, 2014. (cited on Page 19, 41, and 49)

[25] K. R. Thulborn, D. Davis, H. Adams, T. Gindin, and J. Zhou, "Quantitative tissue sodium concentration mapping of the growth of focal cerebral tumors with sodium magnetic resonance imaging," *Magn Reson Med*, vol. 41, pp. 351–359, Feb. 1999. (cited on Page)

[26] S. K. Hilal, A. A. Maudsley, J. B. Ra, H. E. Simon, P. Roschmann, S. Wittekoek, Z. H. Cho, and S. K. Mun, "In vivo NMR imaging of sodium-23 in the human head," *J Comput Assist Tomogr*, vol. 9, pp. 1–7, Jan. 1985. (cited on Page)

[27] O. Zaric, H. Beiglböck, V. Janacova, P. Szomolanyi, P. Wolf, M. Krebs, S. Trattnig, M. Kršśák, and V. Juras, "Repeatability assessment of sodium (23na) MRI at 7.0 T in healthy human calf muscle and preliminary results on tissue sodium concentrations in subjects with addison's disease," *BMC Musculoskeletal Disorders*, vol. 23, p. 925, Oct. 2022. (cited on Page 19)

[28] C. Licht, S. Reichert, M. Guye, L. R. Schad, and S. Rapacchi, "Multidimensional compressed sensing to advance 23na multi-quantum coherences mri," *Magnetic Resonance in Medicine*, 2023. (cited on Page 19, 20, 29, 41, 52, 55, 69, and 73)

[29] L. O. Poku, M. Phil, Y. Cheng, K. Wang, and X. Sun, "23na-mri as a non-invasive biomarker for cancer diagnosis and prognosis," *Journal of Magnetic Resonance Imaging*, vol. 53, no. 4, pp. 995–1014, 2021. (cited on Page 19)

[30] L. P. Nunes Neto, G. Madelin, T. P. Sood, C.-C. Wu, D. Kondziolka, D. Placantonakis, J. G. Golfinos, A. Chi, and R. Jain, "Quantitative sodium imaging and gliomas: a feasibility study," *Neuroradiology*, vol. 60, pp. 795–802, Aug 2018. 29862413[pmid]. (cited on Page 19)

[31] S. Regnery, N. G. Behl, T. Platt, N. Weinfurtner, P. Windisch, K. Deike-Hofmann, F. Sahm, M. Bendszus, J. Debus, M. E. Ladd, H.-P. Schlemmer, S. Rieken, S. Adeberg, and D. Paech, "Ultra-high-field sodium mri as biomarker for tumor extent, grade and idh mutation status in glioma patients," *NeuroImage: Clinical*, vol. 28, p. 102427, 2020. (cited on Page 19)

[32] S. A. Mohamed, K. Herrmann, A. Adlung, N. Paschke, L. Hausner, L. FrÖlich, L. Schad, C. Groden, and H. U. Kerl, "Evaluation of sodium ((23)na) mr-imaging as a biomarker and predictor for neurodegenerative changes in patients with alzheimer's disease," *In vivo (Athens, Greece)*, vol. 35, no. 1, pp. 429–435, 2021. 33402493[pmid]. (cited on Page 19)

[33] K. Huhn, T. Engelhorn, R. A. Linker, and A. M. Nagel, "Potential of sodium mri as a biomarker for neurodegeneration and neuroinflammation in multiple sclerosis," *Frontiers in neurology*, vol. 10, pp. 84–84, Feb 2019. (cited on Page 19)

[34] R. Stobbe, A. Boyd, P. Smyth, D. Emery, D. Valdés Cabrera, and C. Beaulieu, "Sodium intensity changes differ between relaxation- and density-weighted mri in multiple sclerosis," *Frontiers in Neurology*, vol. 12, 2021. (cited on Page 19)

[35] G. LaVerde, E. Nemoto, C. Jungreis, C. Tanase, and F. Boada, "Serial triple quantum sodium mri during non-human primate focal brain ischemia," *Magnetic Resonance in Medicine*, vol. 57, no. 1, pp. 201–205, 2007. (cited on Page 20)

[36] V. D. Schepkin, I. O. Choy, T. F. Budinger, D. Y. Obayashi, S. E. Taylor, W. M. Decampli, S. C. Amartur, and J. N. Young, "Sodium tqf nmr and intracellular sodium in isolated crystalloid perfused rat heart," *Magnetic Resonance in Medicine*, vol. 39, no. 4, pp. 557–563, 1998. (cited on Page 20)

[37] A. Tsang, R. W. Stobbe, and C. Beaulieu, "Triple-quantum-filtered sodium imaging of the human brain at 4.7 t," *Magnetic Resonance in Medicine*, vol. 67, no. 6, pp. 1633–1643, 2012. (cited on Page 20)

[38] I. Hancu, F. E. Boada, and G. X. Shen, "Three-dimensional triple-quantum–filtered 23na imaging of in vivo human brain," *Magnetic Resonance in Medicine*, vol. 42, no. 6, pp. 1146–1154, 1999. (cited on Page)

[39] M. Petracca, R. O. Vancea, L. Fleysher, L. E. Jonkman, N. Oesingmann, and M. Inglese, "Brain intra- and extracellular sodium concentration in multiple sclerosis: a 7 T MRI study," *Brain*, vol. 139, pp. 795–806, 01 2016. (cited on Page 20)

[40] D. P. Fiege, S. Romanzetti, C. C. Mirkes, D. Brenner, and N. J. Shah, "Simultaneous single-quantum and triple-quantum-filtered mri of 23na (sistina)," *Magnetic Resonance in Medicine*, vol. 69, no. 6, pp. 1691–1696, 2013. (cited on Page 20, 74, and 84)

[41] A. Shymanskaya, W. A. Worthoff, G. Stoffels, J. Lindemeyer, B. Neumaier, P. Lohmann, N. Galldiks, K.-J. Langen, and N. J. Shah, "Comparison of [18F]Fluoroethyltyrosine PET and sodium MRI in cerebral gliomas: a pilot study," *Molecular Imaging and Biology*, vol. 22, pp. 198–207, Feb. 2020. (cited on Page 20)

[42] A. Borthakur, I. Hancu, F. E. Boada, G. X. Shen, E. M. Shapiro, and R. Reddy, "In vivo triple quantum filtered twisted projection sodium mri of human articular cartilage," *Journal of Magnetic Resonance*, vol. 141, no. 2, pp. 286–290, 1999. (cited on Page 20 and 74)

[43] K. J. Ooms, M. Cannella, A. J. Vega, M. Marcolongo, and T. Polenova, "23na tqf nmr imaging for the study of spinal disc tissue," *Journal of Magnetic Resonance*, vol. 195, no. 1, pp. 112–115, 2008. (cited on Page 20)

[44] F. Boada, D. Davis, K. Walter, A. Torres-Trejo, D. Kondziolka, W. Bartynski, and F. Lieberman, "Triple quantum filtered sodium mri of primary brain tumors," in *2004 2nd IEEE International Symposium on Biomedical Imaging: Nano to Macro (IEEE Cat No. 04EX821)*, pp. 1215–1218 Vol. 2, 2004. (cited on Page 20)

[45] M. Tseytlin, "Concept of phase cycling in pulsed magnetic resonance using sinusoidal magnetic field modulation," *Z Phys Chem (N F)*, vol. 231, pp. 689–703, Nov. 2016. (cited on Page 20)

[46] L. Fleysher, N. Oesingmann, and M. Inglese, "B0 inhomogeneity-insensitive triple-quantum-filtered sodium imaging using a 12-step phase-cycling scheme," *NMR in Biomedicine*, vol. 23, no. 10, pp. 1191–1198, 2010. (cited on Page 22, 41, 46, 52, and 74)

[47] C. Shannon, "Communication in the presence of noise," *Proceedings of the IRE*, vol. 37, no. 1, pp. 10–21, 1949. (cited on Page 23)

[48] G. McGibney, M. R. Smith, S. T. Nichols, and A. Crawley, "Quantitative evaluation of several partial fourier reconstruction algorithms used in mri," *Magnetic Resonance in Medicine*, vol. 30, no. 1, pp. 51–59, 1993. (cited on Page 24)

[49] M. A. Griswold, P. M. Jakob, R. M. Heidemann, M. Nittka, V. Jellus, J. Wang, B. Kiefer, and A. Haase, "Generalized autocalibrating partially parallel acquisitions (grappa)," *Magnetic Resonance in Medicine*, vol. 47, no. 6, pp. 1202–1210, 2002. (cited on Page 24)

[50] K. P. Pruessmann, M. Weiger, M. B. Scheidegger, and P. Boesiger, "Sense: Sensitivity encoding for fast mri," *Magnetic Resonance in Medicine*, vol. 42, no. 5, pp. 952–962, 1999. (cited on Page 24)

[51] S. L. Brunton and J. N. Kutz, *Data-driven science and engineering: Machine learning, dynamical systems, and control*. Cambridge University Press, 2019. (cited on Page 24)

[52] E. J. Candes and T. Tao, "Near-optimal signal recovery from random projections: Universal encoding strategies?," *IEEE Transactions on Information Theory*, vol. 52, no. 12, pp. 5406–5425, 2006. (cited on Page 24)

[53] E. J. Candès, J. K. Romberg, and T. Tao, "Stable signal recovery from incomplete and inaccurate measurements," *Communications on Pure and Applied Mathematics*, vol. 59, no. 8, pp. 1207–1223, 2006. (cited on Page 25)

[54] D. Donoho, "Compressed sensing," *IEEE Transactions on Information Theory*, vol. 52, no. 4, pp. 1289–1306, 2006. (cited on Page 24)

[55] J. Morlet, G. Arens, E. Fourgeau, and D. Giard, "Wave propagation and sampling theory; Part I, Complex signal and scattering in multilayered media," *Geophysics*, vol. 47, pp. 203–221, 02 1982. (cited on Page 25)

[56] J. Morlet, G. Arens, E. Fourgeau, and D. Giard, "Wave propagation and sampling theory—part ii: Sampling theory and complex waves," *GEOPHYSICS*, vol. 47, no. 2, pp. 222–236, 1982. (cited on Page 25)

[57] M. Lustig, D. Donoho, and J. M. Pauly, "Sparse mri: The application of compressed sensing for rapid mr imaging," *Magnetic Resonance in Medicine*, vol. 58, no. 6, pp. 1182–1195, 2007. (cited on Page 25, 29, and 84)

[58] E. Ilicak, E. U. Saritas, and T. Çukur, "Automated parameter selection for accelerated mri reconstruction via low-rank modeling of local k-space neighborhoods," *Zeitschrift für Medizinische Physik*, 2022. (cited on Page 28, 75, and 78)

[59] T. Goldstein and S. Osher, "The split bregman method for l1-regularized problems," *SIAM Journal on Imaging Sciences*, vol. 2, no. 2, pp. 323–343, 2009. (cited on Page 29, 30, 32, 42, and 44)

[60] L. Bregman, "The relaxation method of finding the common point of convex sets and its application to the solution of problems in convex programming," *USSR Computational Mathematics and Mathematical Physics*, vol. 7, no. 3, pp. 200–217, 1967. (cited on Page 30)

[61] P. Montesinos, J. F. P. Abascal, L. Cussó, J. J. Vaquero, and M. Desco, "Application of the compressed sensing technique to self-gated cardiac cine sequences in small animals," *Magnetic Resonance in Medicine*, vol. 72, no. 2, pp. 369–380, 2014. (cited on Page 30, 31, 32, and 42)

[62] W. Yin, S. Osher, D. Goldfarb, and J. Darbon, "Bregman iterative algorithms for l(1)-minimization with applications to compressed sensing," *Siam Journal on Imaging Sciences - SIAM J IMAGING SCI*, vol. 1, 01 2008. (cited on Page 30)

[63] M. Bydder and J. Du, "Noise reduction in multiple-echo data sets using singular value decomposition," *Magnetic Resonance Imaging*, vol. 24, no. 7, pp. 849–856, 2006. (cited on Page 34)

[64] P. J. Shin, P. E. Z. Larson, M. A. Ohliger, M. Elad, J. M. Pauly, D. B. Vigneron, and M. Lustig, "Calibrationless parallel imaging reconstruction based on structured low-rank matrix completion," *Magn Reson Med*, vol. 72, pp. 959–970, Nov. 2013. (cited on Page 35, 36, and 52)

[65] M. Bydder, F. Ali, V. Ghodrati, P. Hu, J. Yao, and B. M. Ellingson, "Minimizing echo and repetition times in magnetic resonance imaging using a double half-echo k-space acquisition and low-rank reconstruction," *NMR in Biomedicine*, vol. 34, no. 4, p. e4458, 2021. e4458 NBM-20-0253. (cited on Page 36, 38, 49, 50, and 85)

[66] M. Bydder, F. Ali, A. Saucedo, V. Ghodrati, A. Samsonov, M. Akhtari, C. Wang, A. Hagiwara, J. Yao, and B. Ellingson, "Low rank off-resonance correction for double half-echo k-space acquisitions," *Magnetic Resonance Imaging*, vol. 94, pp. 43–47, 2022. (cited on Page 36 and 50)

[67] F. E. Boada, J. S. Gillen, G. X. Shen, S. Y. Chang, and K. R. Thulborn, "Fast three dimensional sodium imaging," *Magnetic Resonance in Medicine*, vol. 37, no. 5, pp. 706–715, 1997. (cited on Page 36 and 75)

[68] A. M. Nagel, F. B. Laun, M.-A. Weber, C. Matthies, W. Semmler, and L. R. Schad, "Sodium MRI using a density-adapted 3D radial acquisition technique,"

Magn Reson Med, vol. 62, pp. 1565–1573, Dec. 2009. (cited on Page 36 and 75)

[69] C. B. Ahn, J. H. Kim, and Z. H. Cho, "High-speed spiral-scan echo planar nmr imaging-i," *IEEE Transactions on Medical Imaging*, vol. 5, no. 1, pp. 2–7, 1986. (cited on Page 36)

[70] C. Licht, S. Reichert, M. Bydder, J. Zapp, S. Corella, F. G. Guye, Maxime Zöllner, L. R. Schad, and S. Rapacchi, "Low-rank reconstruction for simultaneous double-half-echo ^{23}na and undersampled ^{23}na multi-quantum coherences mri," *Magnetic Resonance in Medicine*, 2023. (cited on Page 41, 55, and 73)

[71] D. Collins, A. Zijdenbos, V. Kollokian, J. Sled, N. Kabani, C. Holmes, and A. Evans, "Design and construction of a realistic digital brain phantom," *IEEE Transactions on Medical Imaging*, vol. 17, no. 3, pp. 463–468, 1998. (cited on Page 41)

[72] Y. Blunck, S. Josan, S. W. Taqdees, B. A. Moffat, R. J. Ordidge, J. O. Cleary, and L. A. Johnston, "3d-multi-echo radial imaging of 23na (3d-merina) for time-efficient multi-parameter tissue compartment mapping," *Magnetic Resonance in Medicine*, vol. 79, no. 4, pp. 1950–1961, 2018. (cited on Page 41 and 49)

[73] I. Hancu, J. R. van der Maarel, and F. E. Boada, "A model for the dynamics of spins 3/2 in biological media: signal loss during radiofrequency excitation in triple-quantum-filtered sodium MRI," *J Magn Reson*, vol. 147, pp. 179–191, Dec. 2000. (cited on Page 41 and 49)

[74] M. A. Hoesl, L. R. Schad, and S. Rapacchi, "Volumetric 23na single and triple-quantum imaging at 7t: 3d-cristina," *Zeitschrift für Medizinische Physik*, 2021. (cited on Page 41 and 49)

[75] V. D. Schepkin, A. Neubauer, A. M. Nagel, and T. F. Budinger, "Comparison of potassium and sodium binding in vivo and in agarose samples using tqtppi pulse sequence," *Journal of Magnetic Resonance*, vol. 277, pp. 162–168, 2017. (cited on Page 41)

[76] J. P. Marques, T. Kober, G. Krueger, W. van der Zwaag, P.-F. Van de Moortele, and R. Gruetter, "Mp2rage, a self bias-field corrected sequence for improved segmentation and t1-mapping at high field," *NeuroImage*, vol. 49, no. 2, pp. 1271–1281, 2010. (cited on Page 42 and 50)

[77] T. Küstner, M. Schwartz, C. Würslin, P. Martirosian, N. F. Schwenzer, B. Yang, and H. Schmidt, "Compressed sensing lab: An mr acquisition and reconstruction system," in *Proceedings of the ISMRM Workshop on Data Sampling and Reconstruction*, (Sedona, AZ, USA), Jan. 2016. (cited on Page 42 and 49)

[78] Z. Wang, A. Bovik, H. Sheikh, and E. Simoncelli, "Image quality assessment: from error visibility to structural similarity," *IEEE Transactions on Image Processing*, vol. 13, no. 4, pp. 600–612, 2004. (cited on Page 46 and 53)

[79] M. Subbarao and J.-K. Tyan, "Selecting the optimal focus measure for autofocusing and depth-from-focus," *IEEE transactions on pattern analysis and machine intelligence*, vol. 20, no. 8, pp. 864–870, 1998. (cited on Page 48 and 53)

[80] E. Mussard, T. Hilbert, C. Forman, R. Meuli, J.-P. Thiran, and T. Kober, "Accelerated MP2RAGE imaging using cartesian phyllotaxis readout and compressed sensing reconstruction," *Magn Reson Med*, vol. 84, pp. 1881–1894, Mar. 2020. (cited on Page 50)

[81] H. C. M. Holme, S. Rosenzweig, F. Ong, R. N. Wilke, M. Lustig, and M. Uecker, "Enlive: An efficient nonlinear method for calibrationless and robust parallel imaging," *Scientific Reports*, vol. 9, p. 3034, Feb 2019. (cited on Page 52)

[82] C. Musco and C. Musco, "Stronger approximate singular value decomposition via the block lanczos and power methods," *CoRR*, vol. abs/1504.05477, 2015. (cited on Page 52)

[83] J. Ashburner, G. Barnes, C.-C. Chen, J. Daunizeau, G. Flandin, K. Friston, S. Kiebel, J. Kilner, V. Litvak, R. Moran, *et al.*, "Spm12 manual," *Wellcome Trust Centre for Neuroimaging, London, UK*, vol. 2464, no. 4, 2014. (cited on Page 53)

[84] A. Adlung, C. Licht, S. Reichert, S. Özdemir, S. A. Mohamed, M. Samartzi, M. Fatar, A. Gass, E. N. Prost, and L. R. Schad, "Quantification of tissue sodium concentration in the ischemic stroke: A comparison between external and internal references for 23na mri," *Journal of Neuroscience Methods*, vol. 382, p. 109721, 2022. (cited on Page 53 and 74)

[85] S. Lachner, M. Utzschneider, O. Zaric, L. Minarikova, L. Ruck, Štefan Zbýň, B. Hensel, S. Trattnig, M. Uder, and A. M. Nagel, "Compressed sensing and the use of phased array coils in 23na mri: a comparison of a sense-based and an individually combined multi-channel reconstruction," *Zeitschrift für Medizinische Physik*, vol. 31, no. 1, pp. 48–57, 2021. (cited on Page 74)

[86] Y. Yu, J. Jin, F. Liu, and S. Crozier, "Multidimensional compressed sensing mri using tensor decomposition-based sparsifying transform," *PLOS ONE*, vol. 9, pp. 1–13, 06 2014. (cited on Page 74)

[87] S. F. Roohi, D. Zonoobi, A. A. Kassim, and J. L. Jaremko, "Dynamic mri reconstruction using low rank plus sparse tensor decomposition," in *2016 IEEE International Conference on Image Processing (ICIP)*, pp. 1769–1773, 2016. (cited on Page 74)

[88] J. P. Haldar, "Low-rank modeling of local k-space neighborhoods (LORAKS) for constrained MRI," *IEEE Trans Med Imaging*, vol. 33, pp. 668–681, Mar. 2014. (cited on Page 74)

[89] P. J. Shin, P. E. Z. Larson, M. A. Ohliger, M. Elad, J. M. Pauly, D. B. Vigneron, and M. Lustig, "Calibrationless parallel imaging reconstruction based on structured low-rank matrix completion," *Magn Reson Med*, vol. 72, pp. 959–970, Nov. 2013. (cited on Page 74)

[90] C. Gnahm and A. M. Nagel, "Anatomically weighted second-order total variation reconstruction of 23na mri using prior information from 1h mri," *NeuroImage*, vol. 105, pp. 452–461, 2015. (cited on Page 74)

[91] S. Lachner, O. Zaric, M. Utzschneider, L. Minarikova, Štefan Zbýň, B. Hensel, S. Trattnig, M. Uder, and A. M. Nagel, "Compressed sensing reconstruction of 7 tesla 23na multi-channel breast data using 1h mri constraint," *Magnetic Resonance Imaging*, vol. 60, pp. 145–156, 2019. (cited on Page 74)

[92] Y. Zhao, R. Guo, Y. Li, K. R. Thulborn, and Z.-P. Liang, "High-resolution sodium imaging using anatomical and sparsity constraints for denoising and recovery of novel features," *Magnetic Resonance in Medicine*, vol. 86, no. 2, pp. 625–636, 2021. (cited on Page 74)

[93] A. Adlung, N. K. Paschke, A.-K. Golla, D. Bauer, S. A. Mohamed, M. Samartzi, M. Fatar, E. Neumaier-Probst, F. G. Zöllner, and L. R. Schad, "(23) na MRI in ischemic stroke: Acquisition time reduction using postprocessing with convolutional neural networks," *NMR Biomed*, vol. 34, p. e4474, Jan. 2021. (cited on Page 75, 79, and 83)

[94] K. Gregor and Y. LeCun, "Learning fast approximations of sparse coding," in *Proceedings of the 27th International Conference on International Conference on Machine Learning*, ICML'10, (Madison, WI, USA), p. 399–406, Omnipress, 2010. (cited on Page 75)

[95] K. Kulkarni, S. Lohit, P. Turaga, R. Kerviche, and A. Ashok, "Reconnet: Non-iterative reconstruction of images from compressively sensed measurements," in *Proceedings of the IEEE conference on computer vision and pattern recognition*, pp. 449–458, 2016. (cited on Page 75)

[96] A. L. Machidon and V. Pejović, "Deep learning for compressive sensing: a ubiquitous systems perspective," *Artificial Intelligence Review*, vol. 56, pp. 3619–3658, Apr. 2023. (cited on Page 75)

[97] J. A. Fessler, "MODEL-BASED IMAGE RECONSTRUCTION FOR MRI," *IEEE Signal Process Mag*, vol. 27, pp. 81–89, July 2010. (cited on Page 75 and 83)

[98] Y. Liu, Z. Yi, Y. Zhao, F. Chen, Y. Feng, H. Guo, A. T. L. Leong, and E. X. Wu, "Calibrationless parallel imaging reconstruction for multislice mr data using low-rank tensor completion," *Magnetic Resonance in Medicine*, vol. 85, no. 2, pp. 897–911, 2021. (cited on Page 79)

[99] B. Bilgic, T. H. Kim, C. Liao, M. K. Manhard, L. L. Wald, J. P. Haldar, and K. Setsompop, "Improving parallel imaging by jointly reconstructing multi-contrast data," *Magnetic Resonance in Medicine*, vol. 80, no. 2, pp. 619–632, 2018. (cited on Page 79)

[100] P. Linz, D. Santoro, W. Renz, J. Rieger, A. Ruehle, J. Ruff, M. Deimling, N. Rakova, D. N. Muller, F. C. Luft, J. Titze, and T. Niendorf, "Skin sodium measured with 23na mri at 7.0 t," *NMR in Biomedicine*, vol. 28, no. 1, pp. 54–62, 2015. (cited on Page 79 and 84)

[101] X. Wang, Z. Tan, N. Scholand, V. Roeloffs, and M. Uecker, "Physics-based reconstruction methods for magnetic resonance imaging," *Philosophical Transactions of the Royal Society A: Mathematical, Physical and Engineering Sciences*, vol. 379, no. 2200, p. 20200196, 2021. (cited on Page 83)

[102] S. Mandava, M. B. Keerthivasan, D. R. Martin, M. I. Altbach, and A. Bilgin, "Improving subspace constrained radial fast spin echo MRI using block matching driven non-local low rank regularization," *Phys Med Biol*, vol. 66, p. 04NT03, Feb. 2021. (cited on Page 83)

[103] E. Ilicak, S. Ozdemir, L. R. Schad, M. Weis, S. O. Schoenberg, F. G. Zöllner, and J. Zapp, "Phase-cycled balanced ssfp imaging for non-contrast-enhanced functional lung imaging," *Magnetic Resonance in Medicine*, vol. 88, no. 4, pp. 1764–1774, 2022. (cited on Page 83)

[104] Y. Shcherbakova, C. A. van den Berg, C. T. Moonen, and L. W. Bartels, "Planet: An ellipse fitting approach for simultaneous t1 and t2 mapping using phase-cycled balanced steady-state free precession," *Magnetic Resonance in Medicine*, vol. 79, no. 2, pp. 711–722, 2018. (cited on Page 83)

[105] C. Mirkes, G. Shajan, J. Bause, K. Buckenmaier, J. Hoffmann, and K. Scheffler, "Triple-quantum-filtered sodium imaging at 9.4 tesla," *Magnetic Resonance in Medicine*, vol. 75, no. 3, pp. 1278–1289, 2016. (cited on Page 83)

[106] L. Huang, J. Bai, R. Zong, J. Zhou, Z. Zuo, X. Chai, Z. Wang, J. An, Y. Zhuo, F. Boada, X. Yu, Z. Ling, B. Qu, L. Pan, and Z. Zhang, "Sodium MRI at 7T for early response evaluation of intracranial tumors following stereotactic radiotherapy using the CyberKnife," *AJNR Am J Neuroradiol*, vol. 43, pp. 181–187, Feb. 2022. (cited on Page 84)

[107] C. Ianniello, L. Moy, J. Fogarty, F. Schnabel, S. Adams, D. Axelrod, L. Axel, R. Brown, and G. Madelin, "Multinuclear MRI to disentangle intracellular sodium concentration and extracellular volume fraction in breast cancer," *Sci Rep*, vol. 11, p. 5156, Mar. 2021. (cited on Page 84)

[108] D. C. Noll, D. G. Nishimura, and A. Macovski, "Homodyne detection in magnetic resonance imaging," *IEEE Trans Med Imaging*, vol. 10, no. 2, pp. 154–163, 1991. (cited on Page 84)

[109] A. J. Madhuranthakam, H. H. Hu, A. V. Barger, C. R. Haider, D. G. Kruger, J. F. Glockner, J. Huston III, and S. J. Riederer, "Undersampled elliptical centric view-order for improved spatial resolution in contrast-enhanced mr angiography," *Magnetic Resonance in Medicine*, vol. 55, no. 1, pp. 50–58, 2006. (cited on Page 84)

[110] G. C. Wiggins, J. R. Polimeni, A. Potthast, M. Schmitt, V. Alagappan, and L. L. Wald, "96-channel receive-only head coil for 3 tesla: design optimization and evaluation," *Magn Reson Med*, vol. 62, pp. 754–762, Sept. 2009. (cited on Page 84)

[111] P. J. Schmid, "Dynamic mode decomposition of numerical and experimental data," *Journal of fluid mechanics*, vol. 656, pp. 5–28, 2010. (cited on Page 85)

9. Appendix

9.1 Multi-Dimensional Compressed Sensing reconstruction to advance ^{23}Na MQC MRI on clinical scanners

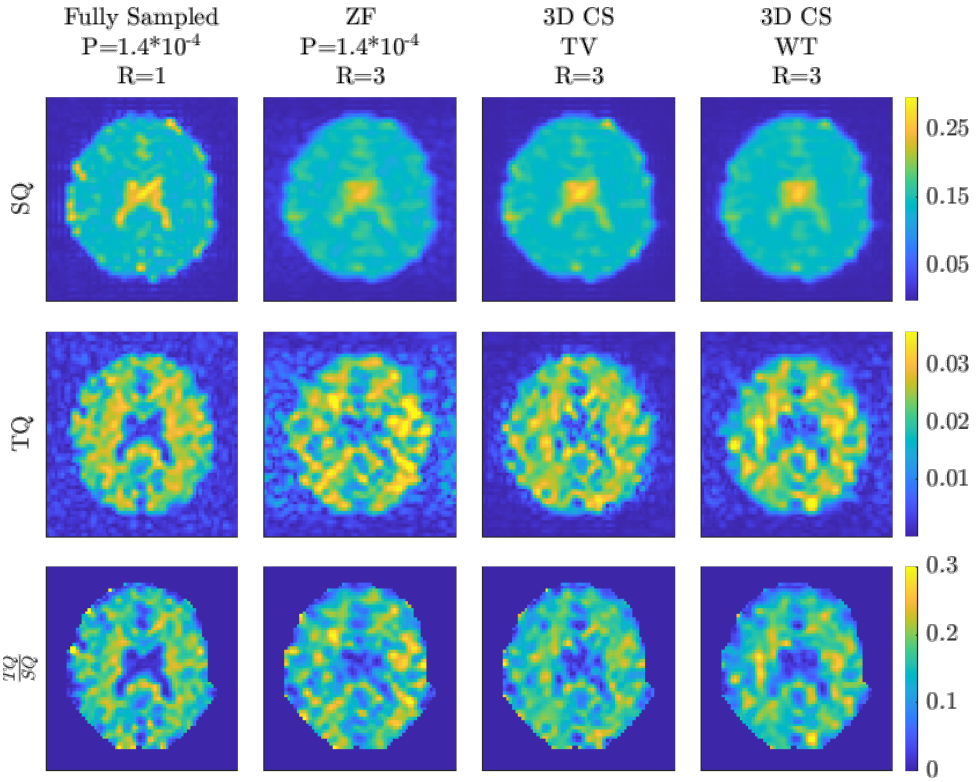

Figure 9.1: Reconstruction evaluation of Wavelet and TV sparsifying transform on numerical simulations. From left to right: fully sampled with additive noise, 3-fold retrospectively undersampled, and with either zero-filling[1], 3D CS leveraging total variation or 3D CS using Wavelet transform reconstructed. Wavelet transform allows multi-resolution decomposition for improved sparsity. However, this asset holds limited benefits in ^{23}Na MQC MRI with limited resolution. On the contrary, WT also exhibits the risk of border effects, especially in applications with noisy backgrounds, such as MQC sodium MRI. It was found that WT and TV performed similarly, so TV was preferred as the spatial sparsifying transform.

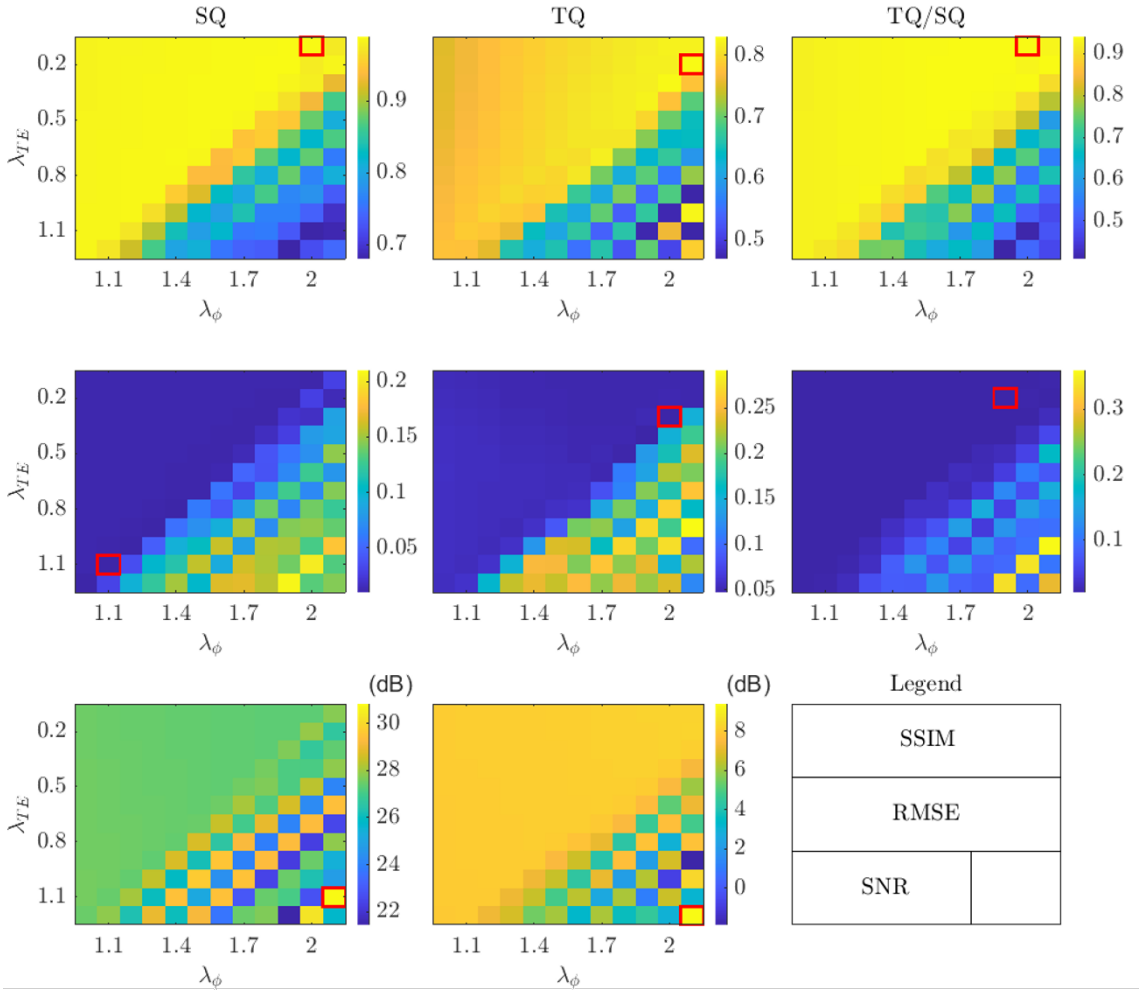

Figure 9.2: Color plots of all metrics for different regularization term weightings for the multi-echo dimension (λ_{TE}) and the phase-cycle dimension (λ_ϕ) evaluated on 3-fold undersampled numerical simulations. The square in red shows the regularization parameter combination that provided the best reconstruction result. The graphs revealed that various values lead to high reconstruction quality. It was also shown that decreasing the weight of the TE regularization led to decreased reconstruction performance, whereas smaller weights were beneficial for phase-cycle regularization. Interestingly, overweighting the regularization factors ($\lambda_{TE,\phi}>1$) results in decreased reconstruction performance. Conclusively, a trade-off between optimal SSIM, RMSE, and SNR was found using $\lambda_{TE} = 0.2$ and $\lambda_\phi = 1.9$.

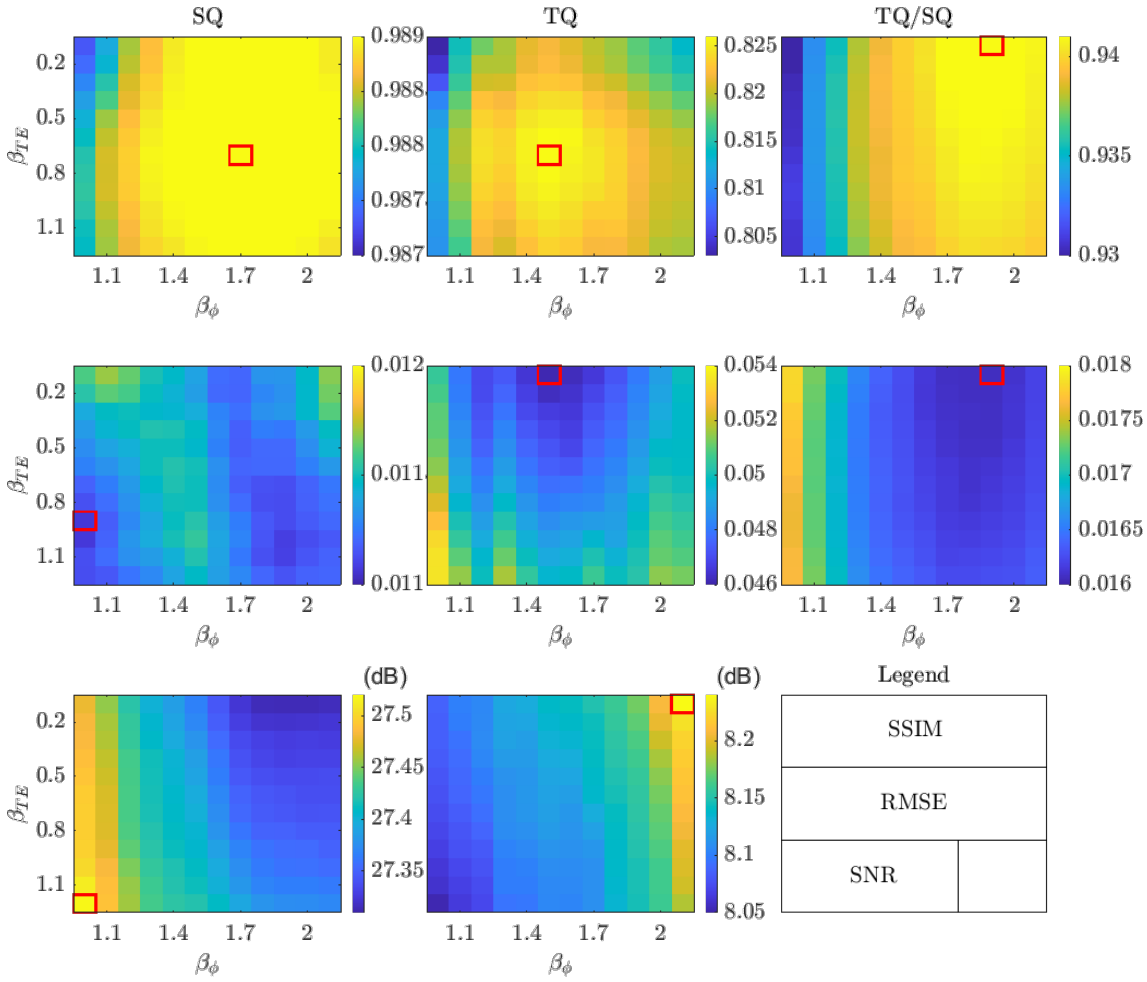

Figure 9.3: Color plots of all metrics for different sparsity thresholds for the multi-echo dimension (β_{TE}) and the phase-cycle dimension (β_ϕ) evaluated on 3-fold undersampled numerical simulations. The square in red shows the regularization parameter combination that provided the best reconstruction result. It is demonstrated that the phase-cycling dimension can be made sparser than the multi-echo dimension. Additionally, the graphs demonstrate that various values lead to high reconstruction quality. Not regularizing the phase-cycle dimension ($\beta_\phi = 0$) leads to decreased reconstruction performance, whereas small thresholds benefit TE regularization. Conclusively, a trade-off between optimal SSIM, RMSE, and SNR was found using $\beta_{TE} = 0.5$ and $\beta_\phi = 1.6$.

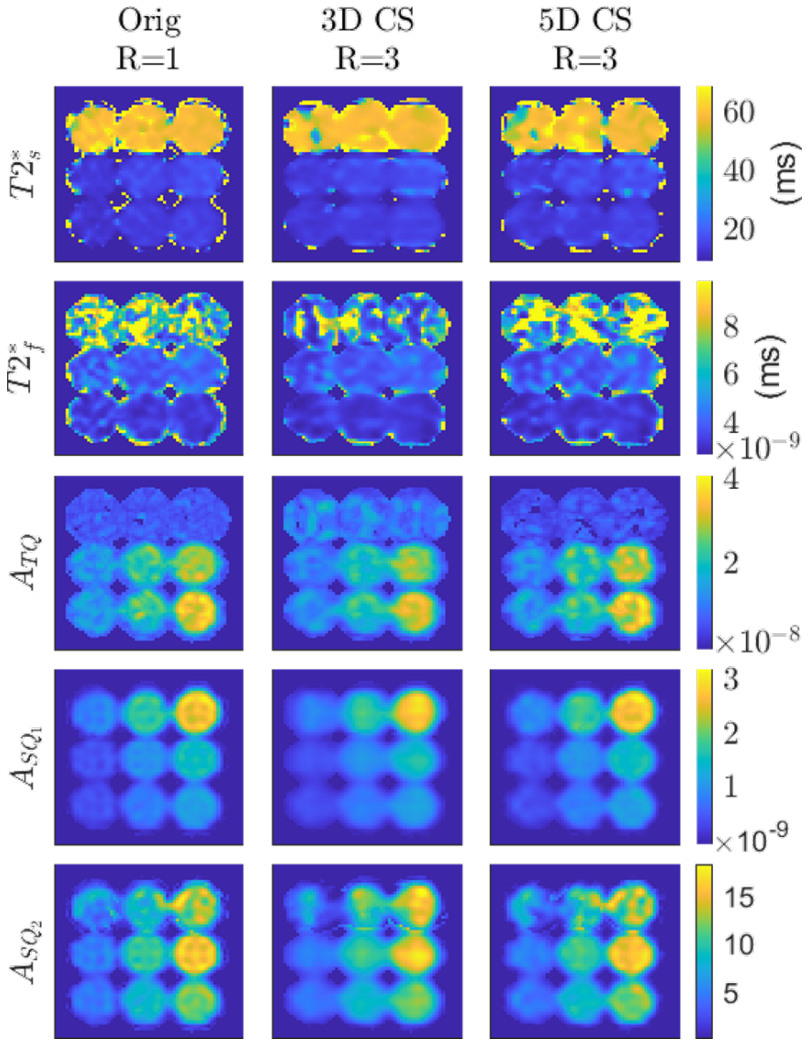

Figure 9.4: Resulting fit parameter maps for a center slice of fully sampled, 3D, and 5D CS reconstructions obtained with an undersampling factor of R=3 (Figure 4.3). Maps are shown with a body mask. It can be appreciated that vials containing 2 or 4% agar gel exhibit shorter T_2^* components as well as larger TQ signal amplitudes. A_{SQ_2} exhibited strong artifacts for the first row of vials, which do not contain agar. Hence, no $T_2 f$ component is expected to yield a noisy A_{SQ_2} parameter fit map. This artifact is even stronger for the 3D CS reconstruction due to the residual aliasing artifact. Additionally, the 3D CS parameters maps revealed extended blurring when compared to fully sampled and 5D CS.

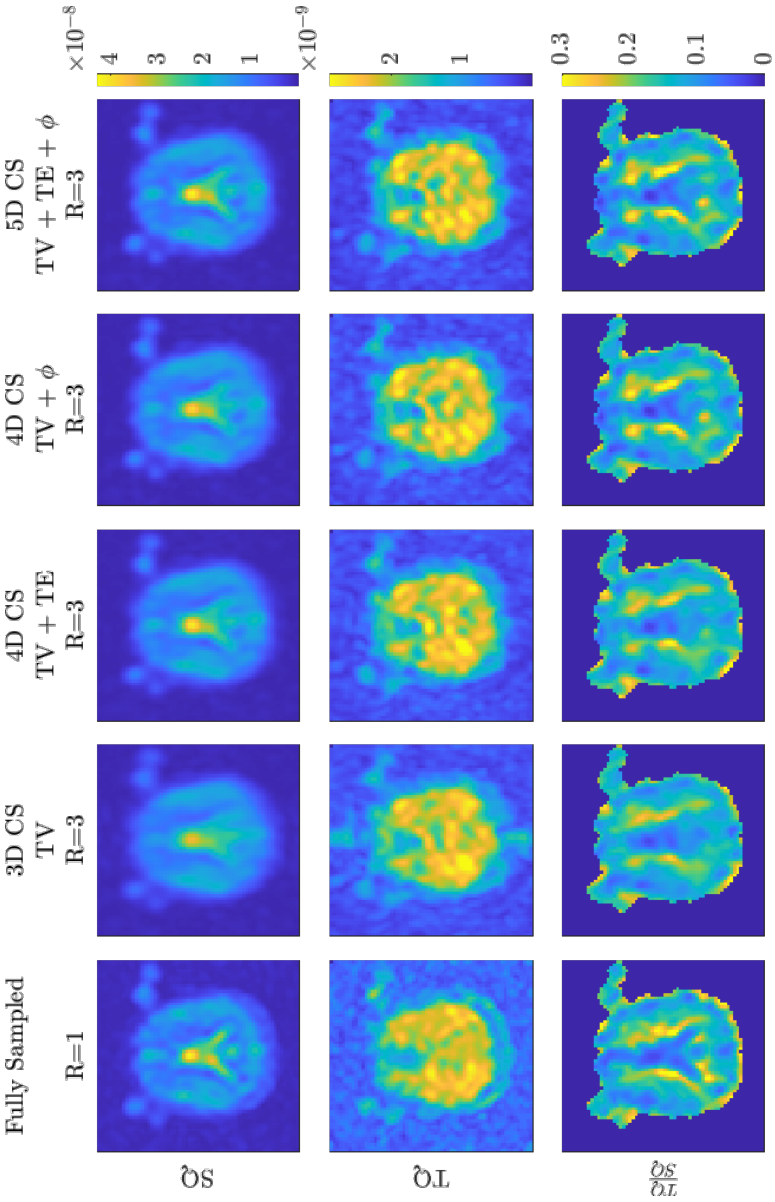

Figure 9.5: Reconstruction performance with different regularization terms added. Notably, improved reconstruction was observed by adding one of each regularization term (TE or ϕ). However, the best performance was obtained when both regularization terms, e.g., 5D CS, were utilized. Quantitative metrics are given in Table 9.3.

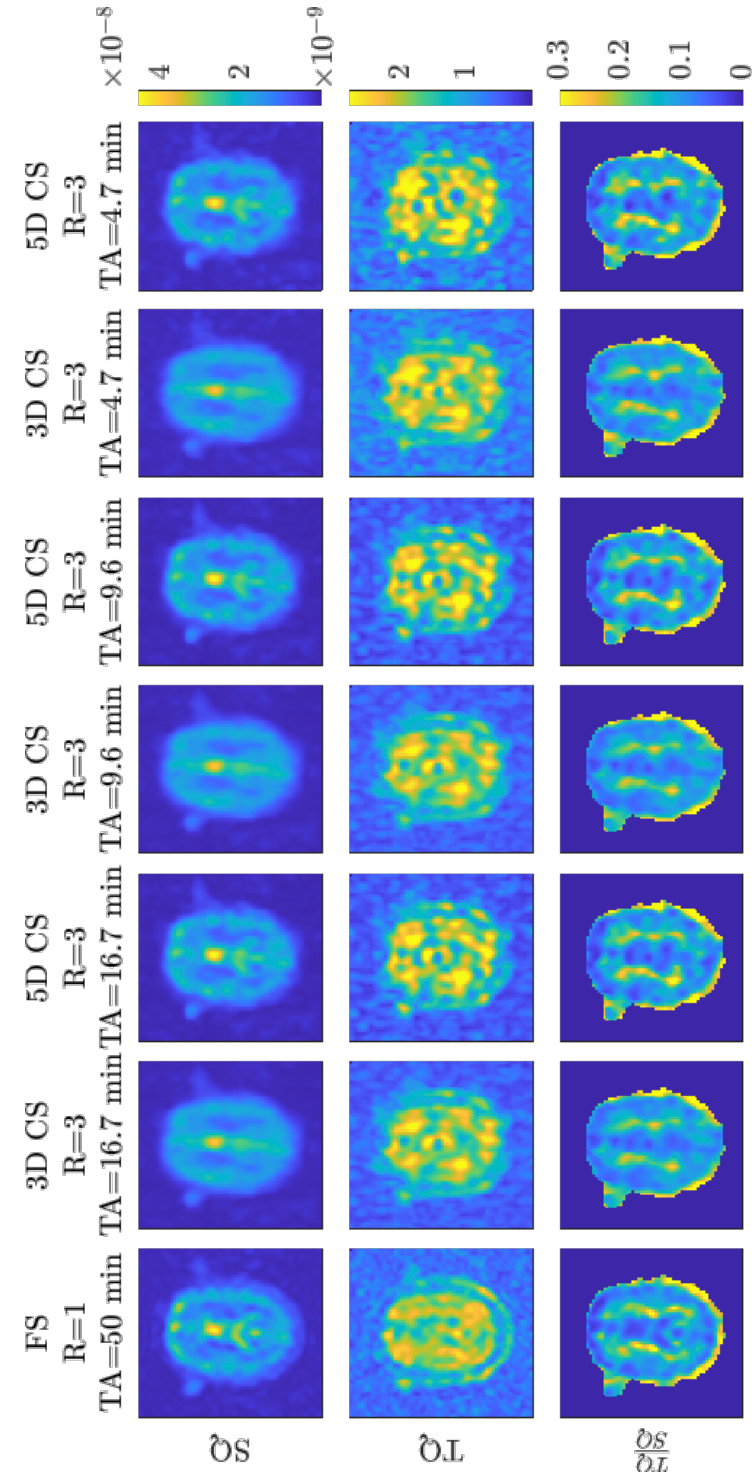

Figure 9.6: Reconstruction performance of 3D and 5D CS for R=3 and reduced averages. Reducing the number of averages enabled further acceleration but degraded image quality. However, 5D CS yielded reliable SQ and TQ/SQ ratio image reconstruction up to an acquisition time of less than 5 minutes.

Table 9.1: Mean and standard deviations for SSIM, RMSE, and SNR of simulated fully sampled and 3-fold undersampled SQ and TQ data for different noise levels. Metrics were evaluated against noise-free, fully sampled data.

Model	Signal	SSIM	RMSE	SNR (dB)
Fully Sampled	SQ	0.81±0.11	0.029±0.018	21.45±3.46
	TQ	0.43±0.20	0.150±0.075	4.99±2.58
	TQ/SQ	0.74±0.16	0.065±0.034	-
3D CS	SQ	0.83±0.05	0.042±0.033	27.23±2.63
	TQ	0.38±0.16	0.161±0.041	4.24±1.38
	TQ/SQ	0.66±0.08	0.072±0.025	-
5D CS	SQ	0.86±0.12	0.026±0.014	24.39±2.94
	TQ	0.52±0.26	0.132±0.072	5.90±2.12
	TQ/SQ	0.75±0.16	0.052±0.030	-

Table 9.2: Mean and standard deviations for T_2^* fast and slow components (ms) of the shown slice in Figure 9.4 reconstructed with 3D and 5D CS at an undersampling factor of R=3.

Vial	T_2^*	**Fully Sampled**	**3D CS**	**5D CS**
1	slow	61±4	57±7	56±9
	fast	7±2	7±3	7±3
2	slow	62±4	61±2	63±4
	fast	7±2	6±2	8±2
3	slow	60±1	60±2	60±2
	fast	7±2	5±2	8±2
4	slow	16±1	16±1	18±2
	fast	4±1	4±1	4±1
5	slow	19±1	19±1	20±<1
	fast	4±<1	4±<1	4±<1
6	slow	21±1	21±2	21±2
	fast	4±<1	4±<1	4±<1
7	slow	14±1	15±1	16±1
	fast	3±<1	3±<1	3±<1
8	slow	16±1	16±1	16±2
	fast	3±<1	3±<1	3±<1
9	slow	17±1	17±1	18±1
	fast	3±<1	3±<1	3±<1

Table 9.3: Quantitative reconstruction evaluation for 3D, 4D and 5D CS models that utilize different regularization terms. 5D CS demonstrated to provide superior reconstruction quality. Images are shown in Figure 9.5.

Model	Signal	SSIM	RMSE	SNR (dB)
3D CS TV	SQ	0.92	0.058	16.07
	TQ	0.82	0.095	8.07
	TQ/SQ	0.82	0.036	-
4D CS TV + TE	SQ	0.96	0.027	17.61
	TQ	0.83	0.083	10.26
	TQ/SQ	0.84	0.032	-
4D CS TV + ϕ	SQ	0.96	0.030	17.76
	TQ	0.86	0.063	9.76
	TQ/SQ	0.85	0.032	-
5D CS TV + TE + ϕ	SQ	0.97	0.020	18.08
	TQ	0.86	0.064	10.83
	TQ/SQ	0.86	0.030	-

9.2 Low-Rank reconstruction to advance ^{23}Na MQC MRI on clinical scanners

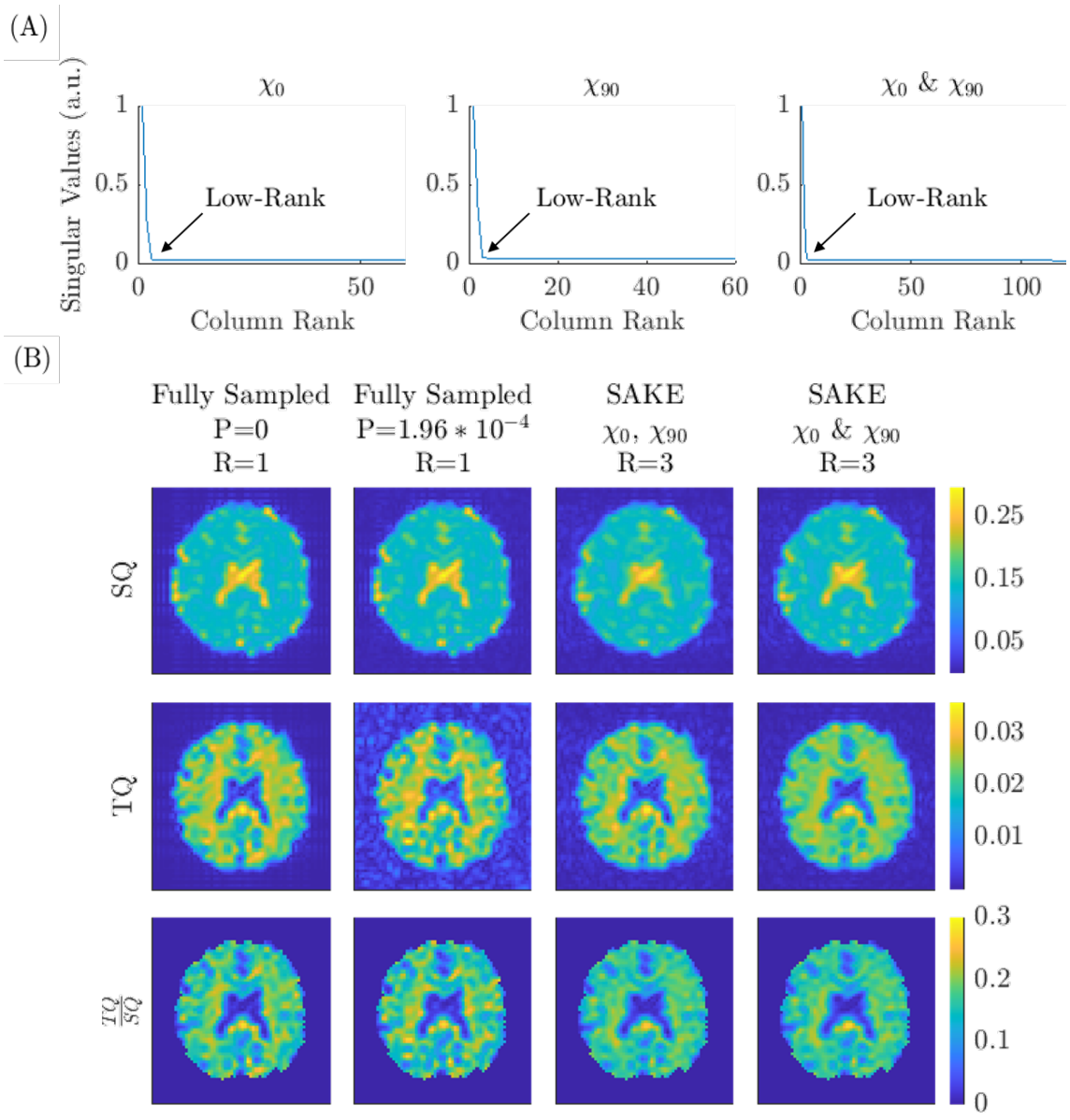

Figure 9.7: (A) ^{23}Na MQC MRI is intrinsically highly redundant due to its multi-dimensional space. This redundancy is shown by plotting the normalized singular values of the singular values decomposition (SVD) of each data set, χ, that was reshaped into a 2D matrix with the first dimension being [x,y,z] and second dimension [TE,ϕ]. By computing the SVD along the multi-echo and phase cycle dimension, it can be appreciated that most variance in the data is expressed by only a few of the largest singular values. It is shown that concatenating χ_0 and χ_{90} further enhances low-rankness. (B) By reconstructing χ_0 and χ_{90}simultaneously, image reconstruction is improved (Table 9.4).

Table 9.4: Quantitative reconstruction performance evaluation with χ_0 and χ_{90} combined or separately reconstructed. The SSIM was improved when the data sets were reconstructed jointly.

Model	Signal	SSIM	RMSE	SNR (dB)
χ_0 & χ_{90} separately	SQ	0.76	0.040	18.44
	TQ	0.71	0.048	9.87
	TQ/SQ	0.92	0.021	-
χ_0 & χ_{90} combined	SQ	0.83	0.030	18.87
	TQ	0.80	0.042	9.82
	TQ/SQ	0.96	0.021	-

Table 9.5: Mean and standard deviations for SSIM, RMSE, and SNR of simulated fully sampled and 3-fold undersampled SQ and TQ data for different noise levels. Metrics were evaluated against noise-free fully sampled data and correspond to data shown in Figure 4.9, A. SSIM and RMSE of SQ and TQ signals were evaluated over the whole image, whereas TQ/SQ ratio was evaluated for the region of interest.

Model	Signal	SSIM	RMSE	SNR (dB)
Fully Sampled	SQ	0.81 ± 0.11	0.029 ± 0.018	19.62 ± 2.36
	TQ	0.43 ± 0.20	0.148 ± 0.0738	4.45 ± 2.24
	TQ/SQ	0.74 ± 0.16	0.053 ± 0.030	-
5D CS	SQ	0.86 ± 0.12	0.026 ± 0.013	21.48 ± 1.67
	TQ	0.52 ± 0.26	$0.127 \pm 0.0.069$	5.10 ± 1.90
	TQ/SQ	0.75 ± 0.16	0.048 ± 0.027	-
SAKE	SQ	0.76 ± 0.05	0.035 ± 0.005	20.19 ± 1.00
	TQ	0.66 ± 0.12	0.067 ± 0.020	6.83 ± 0.17
	TQ/SQ	0.90 ± 0.02	0.024 ± 0.003	-

10. Publications

Journal Papers

Related to this thesis

- Licht C, Reichert S, Guye M, Schad LR, Rapacchi S. Multidimensional compressed sensing to advance 23Na multi-quantum coherences MRI. Magn Reson Med. 2024; 91: 926-941. doi: 10.1002/mrm.29902
- Licht C, Reichert S, Bydder M, et al. Low-rank reconstruction for simultaneous double half-echo 23Na and undersampled 23Na multi-quantum coherences MRI. Magn Reson Med. 2024; 1-16. doi: 10.1002/mrm.30132

Unrelated to this thesis

- Tönnes, C., Licht, C., Schad, L. & Zöllner, F. VirtMRI: A Tool for Teaching MRI. J Med Syst 47, 110 (2023), https://doi.org/10.1007/s10916-023-02004-4
- Adlung, A., Licht, C., Reichert, S., Özdemir, S., Mohamed, S., Samartzi, M., Fatar, M., Gass, A., Prost, E. & Schad, L. Quantification of tissue sodium concentration in the ischemic stroke: A comparison between external and internal references for 23Na MRI. Journal Of Neuroscience Methods. pp. 109721 (2022), https://www.sciencedirect.com/science/article/pii/S0165027022002473
- Hédouin, R., Metere, R., Chan, K., Licht, C., Mollink, J., Walsum, A. Marques, J. Decoding the microstructural properties of white matter using realistic models. NeuroImage, Volume 237. (2021), 118138, ISSN 1053-8119, https://doi.org/10.1016/j.neuroimage.2021.118138

Conference Contributions

Oral presentations

- Licht, C., Reichert, S., Zapp, J., Bydder, M., Guye, M., Schad, L. & Rapacchi, S. Low-Rank Reconstruction for Double-Half-Echo ^{23}Na and undersampled ^{23}Na Multi-Quantum Coherences MRI. ESMRMB 2023 Annual Meeting, Oral Presentation. (2023)
- Licht, C., Zapp, J., Bydder, M., Guye, M., Schad, L. & Rapaachi, S. Improved ^{23}Na Multi-Quantum Coherences MRI with simultaneous Cartesian Double-Half-Echo Sodium Readouts. ISMRM 2023 Joint Annual Meeting, Oral Presentation. (2023)
- Licht, C., Reichert, S., M., Guye, M., Schad, L. & Rapacchi, S. Prospectively undersampled higher resolution ^{23}Na Multi-Quantum Coherences MRI. X-nuclei Workshop 2023, Oral Presentation. (2023)
- Licht, C., Rapacchi, S. & Schad, L. Accelerated in-vivo ^{23}Na Multi-Quantum Coherences MRI by utilizing Low-Rank Matrix Completion. ISMRM 2023 Joint Annual Meeting, X-nuclei Study Group Meeting, Pitch. (2023)
- Licht, C., Schad, L. & Rapacchi, S. An iterative algorithm for resolving high-resolution ^{23}Na Multi-Quantum Coherences MRI from prior ^{1}H constraints. ISMRM 2022 Joint Annual Meeting, X-nuclei Study Group Meeting, Pitch. (2022)

Poster presentations

- Licht, C., Rapacchi, S. & Schad, L. Accelerated in-vivo ^{23}Na Multi-Quantum Coherences MRI by utilizing Low-Rank Matrix Completion. ISMRM 2023 Joint Annual Meeting, Digital Poster. (2023)
- Tönnes, C., Licht, C., Schad, L. & Zöllner, F. SimMRI – A web-based MR Image Simulator for easy accessible MRI teaching. ISMRM 2023 Joint Annual Meeting, Digital Poster. (2023)
- Licht, C., Rapacchi, S. & Schad, L. Low-Rank Image Reconstruction Improves ^{23}Na Multi-Quantum Coherences MRI. X-nuclei workshop, Poster. (2023)
- Licht, C., Rapacchi, S. & Schad, L. Accelerated ^{23}na Multi-Quantum Coherences MRI using Low-Rank Matrix Completion. DS-ISMRM 2022 Joint Annual Meeting, Pitch & Digital Poster. (2022)
- Licht, C., Rapacchi, S. & Schad, L. Improving 3D Cartesian multi-echo readout for ^{23}Na Multi-Quantum Coherences MRI . DS-ISMRM 2022 Joint Annual Meeting, Pitch & Digital Poster. (2022)
- Licht, C., Schad, L. & Rapacchi, S. An iterative algorithm for resolving high-resolution ^{23}Na Multi-Quantum Coherences MRI from prior ^{1}H constraints. ISMRM 2022 Joint Annual Meeting, Digital Poster. (2022)
- Licht, C., Rapacchi, S. & Schad, L. A Multi-Dimensional Compressed Sensing Model to Accelerate ^{23}Na Multi-Quantum Coherences MRI. ISMRM, Benelux, Poster Presentation. (2022)

11. Acknowledgements

First, I would like to thank Prof. Dr. rer. nat. Lothar R. Schad, thank you for allowing me to perform my Dr. sc. hum. studies under your supervision. I could always follow my research interests, and you strongly encouraged the collaborations with Marseille. I am especially thankful for being allowed to attend all the conferences to enlarge my academic network.

Secondly, I would like to thank Stanislas Rapacchi for being a great mentor during my journey. I would have not made it without you. You paved the way into the challenging world of MRI and academic research for me. Thank you for all your input, fruitful discussions, showing me how to write scientific manuscripts and for hosting me in Marseille. Despite my poor french skills, I will still give it a shot. Merci pour ton supervision. J'espère que nous pourrons continuer à travailler sur des projets en MRI et j'espère également pouvoir continuer à poser beaucoup de questions. Veuillez continuer à enseigner aux jeunes scientifiques en MRI, c'était un beau voyage pour moi. Merci beaucoup!

And, of course, Julia. Thanks for all your support during my journey, especially during the writing process. It was great talking about my project with you, and you always listened to my struggles, no matter how repetitive the discussion was. Thanks for staying by my side during this journey - MANY OF THE THANKS.

I would also like to thank all my colleagues at CKM for providing a joyful working environment. I enjoyed the conference trips and had a great time. I am sorry for all the Tischfußball games during the lunch break with me.

Thanks to my family for always supporting me and enabling me to follow my academic path.

Finally, I would like to thank the grant committee of PROCOPE Mobility 2022 and ISMRM Research Exchange 2022 for putting their trust in our work to financially support the collaboration between the CRMBM in Marseille and the CKM in Mannheim. I hope this great collaboration will span well beyond this work.